AD-A279 160 PAGE

Public reporting bu
gathering and main
collection of inform
Davis Highway, Suit

per response, including the time for reviewing instructions, searching existing data sources,
of information. Send comments regarding this burden estimate or any other aspect of this
Headquarters Services, Directorate for Information Operations and Reports, 1215 Jefferson,
and Budget, Paperwork Reduction Project (0704-0188), Washington, DC 20503.

1. AGENCY U!	4. REPORT DATE	3. REPORT TYPE AND DATES COVERED
		Final Technical Report (N00014-90-J-1635)

4. TITLE AND SUBTITLE	5. FUNDING NUMBERS
TUNNELING ACOUSTIC MICROSCOPY	N00014-90-J-1635 N63375 4126952

6. AUTHOR(S)

C. F. Quate and B. T. Khuri-Yakub

7. PERFORMING ORGANIZATION NAME(S) AND ADDRESS(ES)	8. PERFORMING ORGANIZATION REPORT NUMBER
Edward L. Ginzton Laboratory Stanford University Stanford, CA 94305-4085	

9. SPONSORING/MONITORING AGENCY NAME(S) AND ADDRESS(ES)	10. SPONSORING/MONITORING AGENCY REPORT NUMBER
Office of Naval Research Physics Division, Code 1112 Arlington, VA 22217-5000 Attn: L. E. Hargrove	

DTIC
ELECTE
MAY 12 1994
S G D

11. SUPPLEMENTARY NOTES

12a. DISTRIBUTION/AVAILABILITY STATEMENT	12b. DISTRIBUTION CODE
Approved for public release: distribution unlimited	

13. ABSTRACT (Maximum 200 words)

We have demonstrated the use of a near-field scanning acoustic microscope in a noncontact mode using electrostriction to generate acoustic waves from a sub-wavelength dimension spot. Noncontact images have been obtained using the electro-strictive acoustic signal as the sole feedback signal. 5 micrometer lateral resolution in this mode has been demonstrated using 11 micrometer acoustic wavelength.

Due to the nonlinear force interaction between the tip and the sample, frequency doubling is observed in the electrostrictive mode. During imaging, the tip and sample are excited by an rf signal at 350 MHz and the image is composed of a signal at 700 MHz.

14. SUBJECT TERMS	15. NUMBER OF PAGES
scanning probe microscope, near-field acoustic microscope, silicon tips, microfabrication, electrostrictive imaging, frequency doubling	
	16. PRICE CODE

17. SECURITY CLASSIFICATION OF REPORT	18. SECURITY CLASSIFICATION OF THIS PAGE	19. SECURITY CLASSIFICATION OF ABSTRACT	20. LIMITATION OF ABSTRACT

DTIC QUALITY INSPECTED 1

NSN 7540-01-280-5500

Standard Form 298 (Rev. 2-89)

GENERAL INSTRUCTIONS FOR COMPLETING SF 298

The Report Documentation Page (RDP) is used in announcing and cataloging reports. It is important that this information be consistent with the rest of the report, particularly the cover and title page. Instructions for filling in each block of the form follow. It is important to *stay within the lines* to meet *optical scanning requirements*.

Block 1. Agency Use Only *(Leave blank)*.

Block 2. Report Date. Full publication date including day, month, and year, if available (e.g. 1 Jan 88). Must cite at least the year.

Block 3. Type of Report and Dates Covered. State whether report is interim, final, etc. If applicable, enter inclusive report dates (e.g. 10 Jun 87 - 30 Jun 88).

Block 4. Title and Subtitle. A title is taken from the part of the report that provides the most meaningful and complete information. When a report is prepared in more than one volume, repeat the primary title, add volume number, and include subtitle for the specific volume. On classified documents enter the title classification in parentheses.

Block 5. Funding Numbers. To include contract and grant numbers; may include program element number(s), project number(s), task number(s), and work unit number(s). Use the following labels:

C	-	Contract	PR	- Project
G	-	Grant	TA	- Task
PE	-	Program Element	WU	- Work Unit Accession No.

Block 6. Author(s). Name(s) of person(s) responsible for writing the report, performing the research, or credited with the content of the report. If editor or compiler, this should follow the name(s).

Block 7. Performing Organization Name(s) and Address(es). Self-explanatory.

Block 8. Performing Organization Report Number. Enter the unique alphanumeric report number(s) assigned by the organization performing the report.

Block 9. Sponsoring/Monitoring Agency Name(s) and Address(es). Self-explanatory.

Block 10. Sponsoring/Monitoring Agency Report Number. *(If known)*

Block 11. Supplementary Notes. Enter information not included elsewhere such as: Prepared in cooperation with...; Trans. of...; To be published in.... When a report is revised, include a statement whether the new report supersedes or supplements the older report.

Block 12a. Distribution/Availability Statement. Denotes public availability or limitations. Cite any availability to the public. Enter additional limitations or special markings in all capitals (e.g. NOFORN, REL, ITAR).

DOD	-	See DoDD 5230.24, "Distribution Statements on Technical Documents."
DOE	-	See authorities.
NASA	-	See Handbook NHB 2200.2.
NTIS	-	Leave blank.

Block 12b. Distribution Code.

DOD	-	Leave blank.
DOE	-	Enter DOE distribution categories from the Standard Distribution for Unclassified Scientific and Technical Reports.
NASA	-	Leave blank.
NTIS	-	Leave blank.

Block 13. Abstract. Include a brief *(Maximum 200 words)* factual summary of the most significant information contained in the report.

Block 14. Subject Terms. Keywords or phrases identifying major subjects in the report.

Block 15. Number of Pages. Enter the total number of pages.

Block 16. Price Code. Enter appropriate price code *(NTIS only)*.

Blocks 17. - 19. Security Classifications. Self-explanatory. Enter U.S. Security Classification in accordance with U.S. Security Regulations (i.e., UNCLASSIFIED). If form contains classified information, stamp classification on the top and bottom of the page.

Block 20. Limitation of Abstract. This block must be completed to assign a limitation to the abstract. Enter either UL (unlimited) or SAR (same as report). An entry in this block is necessary if the abstract is to be limited. If blank, the abstract is assumed to be unlimited.

Final Technical Report

to

Office of Naval Research

for a Program of Research Entitled:

TUNNELING ACOUSTIC MICROSCOPY

for the period:
April 1, 1990-December 31, 1993

Principal Investigators:
Calvin F. Quate
B. T. Khuri-Yakub

94-14264

Accesion For		
NTIS CRA&I		☒
DTIC TAB		☐
Unannounced		☐
Justification		
By		
Distribution /		
Availability Codes		
Dist	Avail and / or Special	
A-1		

G. L. Report No. 5084

Edward L. Ginzton Laboratory
Stanford University
Stanford, California 94305-4085

94 5 11 012

ABSTRACT

Near-field scanning acoustic microscopy (NSAM) is a recent addition to the developing field of scanning probe microscopy. Its historical roots are scanning acoustic microscopy (SAM) first demonstrated in 1973 and scanning tunneling microscopy (STM), introduced in 1981. The NSAM uses acoustic waves to probe the sample but unlike the SAM that operates in the far-field regime, the resolution of the NSAM is not bound by the diffraction-limited spot created by an acoustic lens. Instead of an acoustic lens, the NSAM uses a sharp probe like those used in STM to contain the acoustic waves and deliver them to a spot of sub-wavelength dimension on the sample. While similarities in instrumentation exist between the NSAM and the STM, the contrast mechanism for the NSAM is based on variations in the acoustic properties of the sample in addition to surface topography.

The NSAM presented in this dissertation utilizes key components which are microfabricated using manufacturing processes similar to those used in integrated circuit fabrication. The microfabricated probes are comprised of silicon cones, with height on the order of 100 μm, integrated with ultrasonic transducers which operate in the GHz frequency range. Operation of the instrument has been demonstrated in contacting as well as non-contacting modes. The latter mode relies on electrostrictive forces to couple the sound from tip to sample. In the contacting mode, the vertical and lateral resolutions of the instrument are 30 Å and 1000 Å respectively.

In addition to the topic of NSAM, some microfabrication technologies for STM and atomic force microscopy (AFM) are also described in this dissertation.

TABLE OF CONTENTS

LIST OF TABLES

LIST OF ILLUSTRATIONS

Chapter 1: Introduction to Scanning Probe Microscopy and Microfabrication

1.1 Introduction to Near-Field Scanning Probe Microscopy

When one thinks of microscopes, one often thinks of the standard optical microscopes that are common in high school biology laboratories. Those instruments map the entire image simultaneously and use lenses to focus light down to a diffraction-limited spot. In the most common forms of optical microscopes, the lens also receives the light reflected from the spot and forms a magnified image of the sample. The resolution in this case is limited by the size of the spot that can be created (Figure 1.1 (a)).

The diffraction-limited spot size is the product of the f-number of the lens and the wavelength of the radiation used, where the f-number is ratio of the focal length of the lens to its diameter. f-numbers can only be reduced to approximately 0.5 so in order to make substantial gains in resolution, the wavelength of the radiation must be made as short as possible. The other characteristic of most optical microscopes is that every point in the focal plane is simultaneously mapped to a point on the image plane of the microscope so that the entire image is produced at once.

Two types of optical microscopes that do not map the entire image simultaneously are the confocal scanning optical microscope (CSOM) [1] and the near-field scanning optical microscope (NSOM) [2, 3]. These instruments create images point by point by scanning a diffraction-limited spot over a sample surface.

1
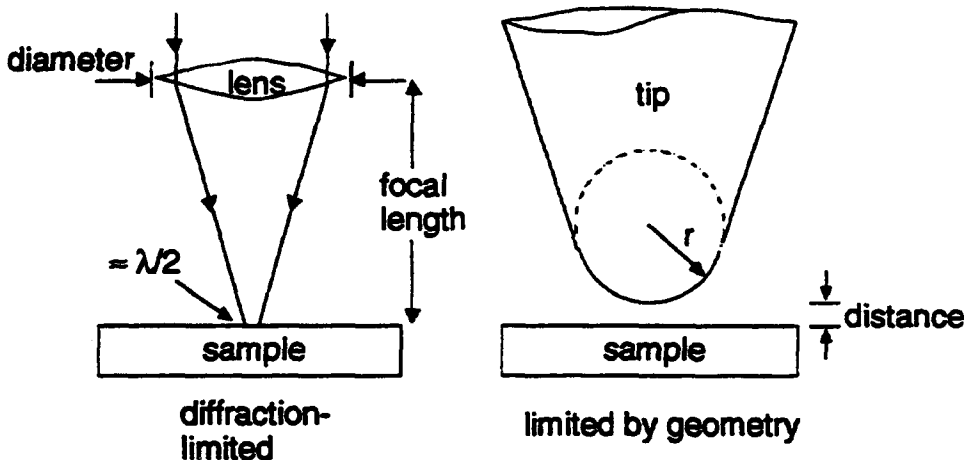
Figure 1.1 a) The resolution of far-field microscopes is determined by the size of a diffraction-limited spot produced by a lens. b) In near-field scanning probe microscopy a sharp probe confines the area of interaction between the tip and sample to a sub-wavelength sized spot. The resolution in this case is limited by the sharpness of the tip and the distance between the tip and sample.

In contrast to traditional far-field microscopes, the recently developed near-field scanning probe microscopes are not limited by diffraction and they compose the image point by point. In near-field scanning probe microscopes such as the scanning tunneling microscope (STM) [4], atomic force microscope (AFM) [5, 6], NSOM [2, 3] and near-field scanning acoustic microscope (NSAM) [7, 8, 9, 10, 11, 12] a sharp probe is used to confine the interaction between the probe and the sample. The lateral resolution of the microscopes is typically limited by the sharpness of the tip and the spacing between the tip and the sample (Figure 1.1 (b)) and since the probes can be made significantly sharper than the characteristic wavelength of the interaction mechanism being used, resolution significantly greater than $\lambda/2$ can be achieved.

The image is composed point by point by scanning the tip in a raster fashion over the sample while controlling the height of the tip by means of a feedback circuit that monitors the strength of the interaction between the tip and the sample. In principle, the resolution of these microscopes is constant at every point of the sample so the resulting image is a true 3-dimensional mapping of the sample surface.

The best known example of a near-field scanning microscope is the STM. The STM is an electron microscope like the more established scanning electron microscope (SEM) but whereas the SEM uses lenses to focus an electron beam to a small spot on the sample, the STM utilizes a sharp metal tip to conduct the electrons to a single atom at the apex of the tip. When the tip is brought within a few angstroms of a conducting sample, the electrons can quantum mechanically tunnel from the tip to the sample while never exceeding the energy of the barrier represented by the vacuum gap between the tip and sample [13]. When a small DC bias is placed across the tip and sample, the electron transition probability becomes exponentially higher in one direction than in the other and so a DC tunneling current flows. The tunneling current is also an exponential function of gap spacing. If an atom at the apex of the tip is even one atomic radius closer to the sample than its neighbors, the closest atom to the sample conducts almost all of the tunneling current. This confinement of the tunneling current to one atom is the source of the STM's exquisite lateral resolution.

Although the STM has many unique features, its basic components are shared by most scanning probe microscopes (Figure 1.2). In scanning probe microscopes, the sample is mounted on a mechanical scanner. The scanners are typically tripods made from segments of a piezoelectric ceramic such as lead zirconium titanate (PZT). PZT is chosen for its high sensitivity and relative stiffness. The tip is brought close to the

3

sample while the interaction signal is monitored. In the case of STM, the interaction signal is the tunneling current. A feedback circuit controls the spacing between the tip and sample by feeding an error signal to the z piezo of the scanner that controls the separation between the tip and sample. The display is created by recording the incoming interaction or feedback error signal at each x and y position and displaying the result on a video monitor as a 2-dimensional array of gray scales.

While tripod scanners are still used in certain ultra-high resolution microscopes such as UHV spectroscopy STMs, where the tripods' lower voltage sensitivity causes smaller scan ranges and lower scanner noise, in many applications they have been replaced by piezoelectric tube scanners [14]. Tube scanners are hollow PZT tubes with typical sidewall thickness on the order of 20 mils. The walls of the tube are metallized to form electrodes on both the interior and exterior. The interior metal film is continuous, while the outer metal film is segmented into four sections to create four independently addressable electrodes. To make the tube scan in x and y and maintain the spacing in z, the inner electrode is biased with a DC voltage and the outer electrodes are fed a combined voltage representing the scan and height information. The scan range for the tripods is a few thousand angstroms while some long tube scanners can scan as far as 200 µm.

1.2   Applications of Microfabrication in Scanning Probe Microscopy

The STM can be built completely using traditionally machined parts. Its close relative, the AFM however can not achieve its best resolution without the microfabrication of certain critical components.
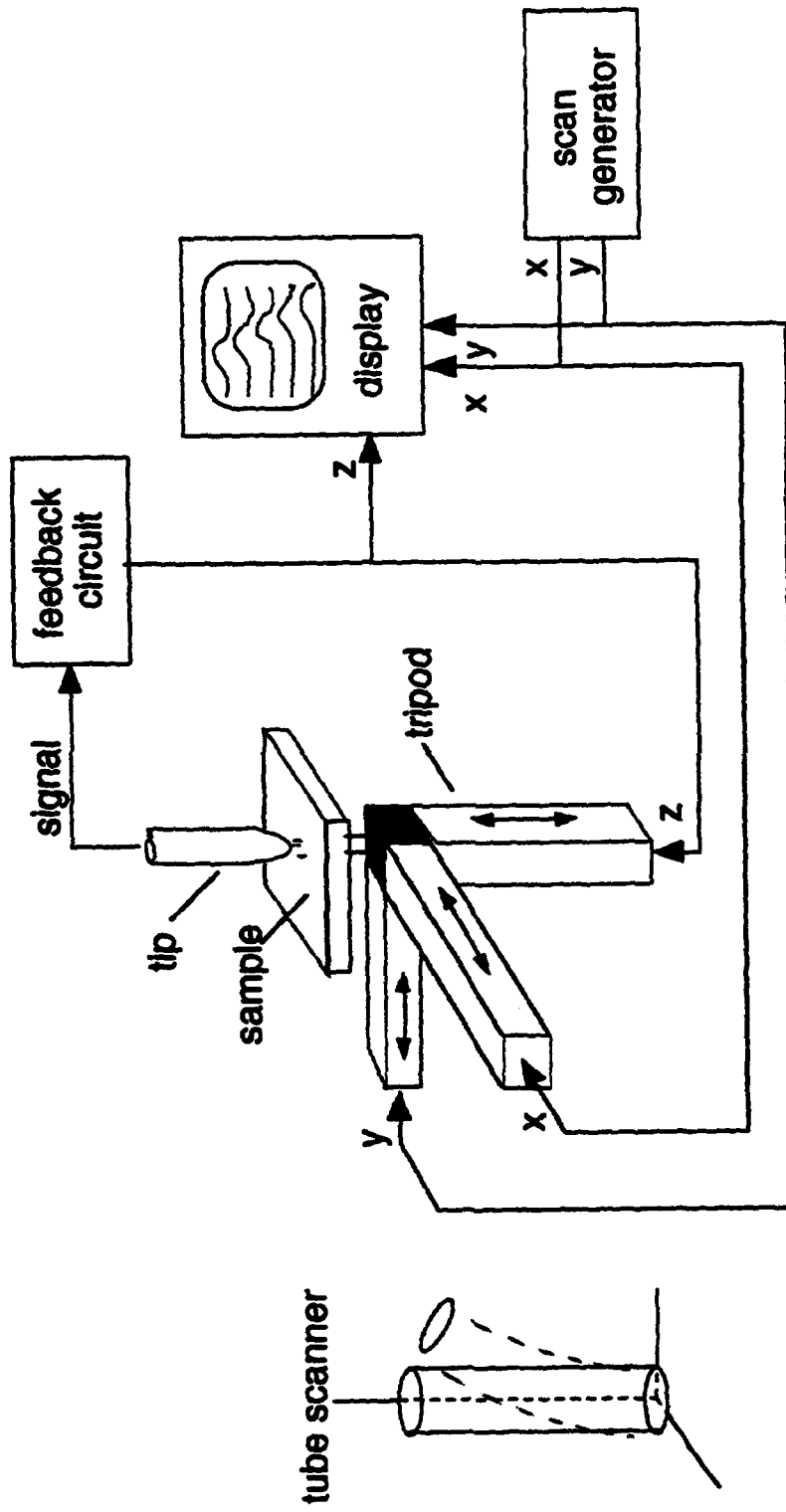
Figure 1.2 Most scanning probe microscopes share key elements. These include: the tip scanner, feedback circuit, scan generator and display. Piezoelectric scanner tubes have replaced tripod scanners due to their large range and ease of fabrication.

In AFM, the forces between the atoms on the tip and atoms on the sample are measured by monitoring the deflection of a force-sensing cantilever (Figure 1.3). The deflection sensor can take various forms including tunneling sensors [5], optical interferometers [15], optical beam deflection sensors [16] and integrated piezoresistive detectors [17]. The forces used during imaging are typically on the order of 10^{-9} N [15]. The AFM can be operated in both the contact mode, in which repulsive forces deflect the cantilever, and non-contact mode, in which the cantilever is vibrated near the sample surface where forces between the cantilever and the sample affect the amplitude or frequency of the moving cantilever [15, 18].
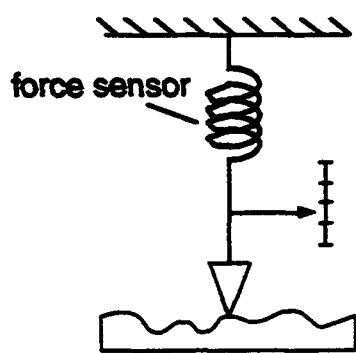
The concept   ## The instrument
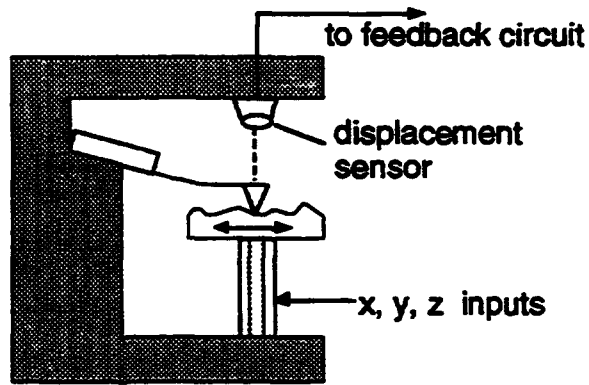
Figure 1.3 An AFM maps the topography of conducting or insulating samples by measuring the interatomic forces between a tip and a sample through the use of a force-sensing element shown schematically as a spring but actually embodied as a cantilever.

The first AFM [4] was equipped with a cantilever fabricated by cutting a thin gold foil. While this AFM obtained some images and was able to resolve atomic steps, the cantilever proved to be too crude to resolve the atomic corrugations of the sample. In

order to improve the performance of the AFM, the cantilever needed to be constructed in such a way as to have both a low spring constant and a high resonance frequency. Since the resonance frequency of the cantilever, ω_0, is given by

$$\omega_0 = \sqrt{\frac{k}{m}} \tag{1.1}$$

the mass, m, must be kept small if the resonance frequency, ω_0, is to be made high while the force constant, k, is minimized. Even in 1986, the inventors of the first AFM understood that these requirements suggest the use of microfabrication.

Microfabricated cantilevers for AFM were first introduced by Albrecht and Quate in 1987 [6]. These cantilevers were made from silicon wafers and thin films using microfabrication techniques usually found in the manufacture of integrated circuits. Albrecht fabricated cantilevers with dimensions on the order of 100 x 20 x 1 μm, force constants on the order of 1 N/m and resonance frequencies in the tens to hundreds of kHz range. These cantilevers were used to obtain the first images of atomic corrugations with the AFM. These early cantilevers were made from silicon dioxide and were very fragile. They also did not have integral tips so naturally occurring asperities had to be relied upon to act as tips when imaging. In the succeeding years, many improvements have been made in the design and manufacture of AFM cantilevers including the use of silicon nitride instead of silicon dioxide for increased cantilever robustness and the addition of integral, sharp tips to aid in the imaging of rough samples. Some of these improvements are presented in this dissertation. Many other improvements have been presented by other researchers in what has become a fertile common ground between microfabrication and microscope research.

1.3 Near-Field Scanning Acoustic Microscopy

The AFM creates images using DC force as the contrast mechanism. It is not a large conceptual leap from the use of DC or low frequency forces in AFM to the use of ultra-high frequency force modulations used in NSAM. An acoustic wave is simply a time varying force wave which propagates in a medium. The first NSAMs were demonstrated by Takata and coworkers at Hitachi Central Research Laboratory [7] and Uozumi and coworkers at Aoyama Gakuin University [8] both in Japan. In NSAM, an acoustic wave is launched down a tip where it is subsequently coupled into a sample. The interaction between the tip and sample can be measured either by monitoring the transmitted acoustic power using a receiving ultrasonic transducer mounted beneath the sample, or by monitoring the changes in acoustic resonance caused by loading of the tip.

The NSAM differs from the STM in that the NSAM can image insulators as well as conductors. Unlike the AFM however, the NSAM may yield information about a sample's material properties such as elasticity and acoustic impedance. By obtaining 2-dimensional mappings of variations in these properties, the composition or mechanical structure of samples may be determined.

Since the NSAM's contrast mechanism is based on the relative efficiency of acoustic coupling between the tip and sample, any force interaction that can generate acoustic waves in the tip and sample can conceivably be exploited as an imaging mechanism. One such example is the use of electric fields between the tip and sample to generate acoustic waves. If an electric field is placed across a conductive tip and sample, an attractive force is created much as in the case of a parallel plate capacitor. If the electric field is varied at high frequencies, the attractive force also varies with time and an

acoustic wave is launched into the tip and sample. Some of the acoustic power can be collected by a transducer at the back of the tip and used for imaging.

The electrostrictive mode of acoustic wave generation allows the NSAM to be used in non-contacting mode and perhaps more importantly to estimate the force between the tip and sample for a given value of received acoustic power. Since the force caused by an electric field can be known, and the acoustic power for a given electric field is known, the force and acoustic power can be correlated to give the NSAM a meaningful force calibration.

The first NSAMs, operated in the frequency range of 80 kHz to 5 MHz, were very similar in instrumentation to STMs, often using metal tips with bonded ultrasonic transducers to create ultrasonically active probes. The NSAM described in this dissertation uses microfabricated probes comprised of silicon tips and zinc oxide piezoelectric transducers. By utilizing microfabrication, it is possible to make tips with radii of curvature of less than 1000 Å and transducers with operating frequencies up to several GHz. The NSAM with microfabricated NSAM has been demonstrated in both the transmission and electrostrictive modes of operation. While its current demonstrated resolution does not exceed that of the non-microfabricated instruments, there are several improvements possible which may yield increased resolution for the microfabricated instrument. In addition, since the key components of our NSAM are microfabricated, it may be possible to integrate the acoustically active probes onto standard AFM cantilevers to allow simultaneous operation in the AFM and NSAM modes.

1.4   Overview of Dissertation

The principal theme of this dissertation is the use of microfabrication in the field of scanning probe microscopy. Central to all scanning probe microscopes is the tip, therefore a discussion of various microfabrication processes for tips is presented in Chapter 2. The development of the AFM cantilevers with conical and pyramidal tips described in Chapter 2 was done in close collaboration with Tom Albrecht. Chapter 3 describes in detail the fabrication of the tetrahedral tip and its use in AFM. Images taken by Rob Barrett and me with various tips and flat cantilevers are shown side by side to demonstrate the positive effects of having sharp tips on AFM cantilevers.

The experience making microfabricated tips and cantilevers was heavily leveraged to design and demonstrate the NSAM with microfabricated probes in collaboration with Babur Hadimioglu and Prof. Pierre Khuri-Yakub. An overview of the NSAM's history and a description of the NSAM instrumentation are presented in Chapter 4. The transmission mode operation of the NSAM is described in Chapter 5. Images taken in the transmission mode are shown in Chapter 6. The electrostrictive mode of operation is described in Chapter 7 and some early images taken in this mode are shown.

Chapter 8 describes a microfabricated STM scanner made using a planar microfabrication process. The device was invented by Tom Albrecht and Mark Zdeblick and was developed in a team effort. An atomic resolution image of graphite taken using this microfabricated scanner is presented.

References

1)   J. Z. Young and F. Roberts, Nature **167**, 231 (1951).

2)   U. C. Fischer, U. T. Durig and D. W. Pohl, App. Phys. Lett. **52**, 249 (1988).

3)   E. Betzig, J. K. Trautman, T. D. Harris, J. S. Weiner, and R. L. Kostelak, Science **252**, 1468 (1991).

4)   G. Binnig, H. Rohrer, C. Gerber and E. Weibel, Phys. Rev. Lett. **50**, 120 (1983).

5)   G. Binning, C. F. Quate and Ch. Gerber, *Phys. Rev. Lett.* **56**, 1164 (1986).

6)   T. R. Albrecht and C. F. Quate, J. Vac. Sci. Technol. A **6**, 271 (1987).

7)   K. Takata, T. Hasegawa, S. Hosaka, S. Hosoki, and T. Kumoda, Appl. Phys. Lett. **55**, 1718 (1989).

8)   K. Uozumi and K. Yamamuro, Jpn. J. Appl. Phys. **28**, 1297 (1989).

9)   P. Güthner, U. Ch. Fischer and K. Dransfeld, Appl. Phys. **B48**, 89 (1989).

10)   J. K. Zieniuk and A. Latuszek, 1986 IEEE Ultrasonics Symposium Proceedings, 1037 (1986).

11)   B. T. Khuri-Yakub, C. Cinbis, C. H. Chou and P. A. Reinholdtsen, 1989 IEEE Ultrasonics Symposium Proceedings, 805 (1989).

12)   S. Akamine, B. Hadimioglu, B. T. Khuri-Yakub, H. Yamada and C. F. Quate, TRANSDUCERS '91 International Conference on Solid-StateSensors and Actuators Proceedings, San Fracisco, 857 (1991).

13)   J. G. Simmons, J. Appl. Phys. **34**, 1793 (1963).

14)   G. Binnig and D. P. E. Smith, Rev. Sci. Instrum. **57**, 1688 (1986).

15)   Y. Martin, C. C. Williams, and H. K. Wickramasinghe, J. Appl. Phys. **61**, 4723 (1987).

16)   G. Meyer and N. M. Amer, Appl. Phyus. Lett. **53**, 1045 (1988).

17)   M. Tortonese, R. C. Barrett and C. F. Quate, Appl. Phys. Lett. **62**, 834 (1993).

18)   T. R. Albrecht, P. Grütter, D. Horne and D. Rugar, J. Appl. Phys. **69**, 668 (1991).

Chapter 2:   Microfabricated Tips

2.1   The Importance of Tip Sharpness in Scanning Probe Microscopy

It is commonly understood that a sharp tip is necessary to do scanning probe microscopy effectively. What constitutes a "sharp" tip however is open to debate. The tip sharpness necessary is a function of both the exact type of microscope being used and the nature of the sample under study. Generally speaking, the more sensitive the interaction signal is to changes in spacing between the tip and sample, the less sharp the tip needs to be achieve high resolution. In addition, a flatter sample requires a less sharp tip for high quality imaging.

The STM is a good example of a type of microscope that does not necessarily need a sharp tip in order to obtain optimal resolution. The tunneling current, which is the STM's interaction signal, decreases exponentially with increasing spacing between the tip and sample; therefore, even if the tip is relatively blunt, high resolution images of atomically flat samples can still be obtained since some atom on the tip usually extends an atomic radius below its neighbors and conducts most of the tunneling current (Figure 2.1 (a)) [1].

When imaging a sample with surface roughness greater than the roughness of the tip, the tunneling current is no longer strictly confined to a single atom (Figure 2.1(b)). In this case, the image contains artifacts associated with the switching of the tunneling signal from one atom to another or from one atom to multiple atoms. Hence, when

imaging rough samples, even a microscope that relies on a highly distance dependent interaction signal suffers if the tip does not have a radius of curvature less than the relevant features of the sample.

(a)   (b)
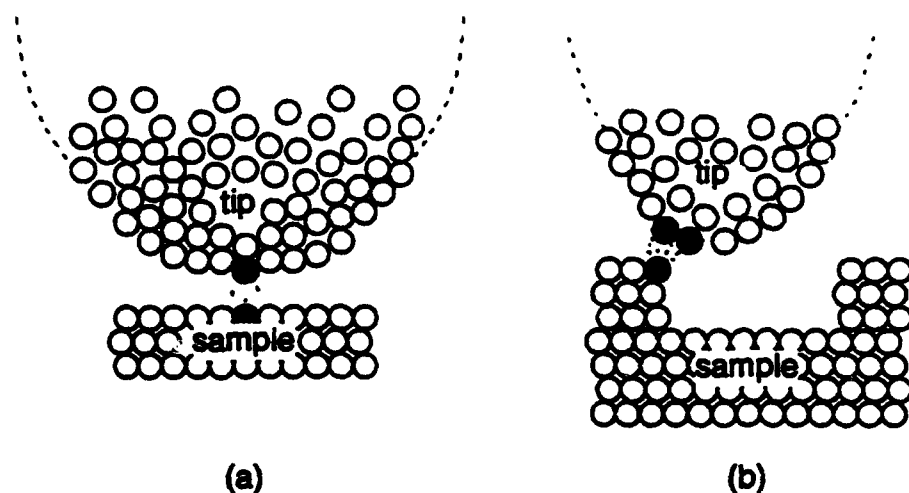
Figure 2.1 a) For imaging flat samples using a microscope like the STM whose interaction signal depends strongly on distance, even a relatively blunt tip is typically capable of achieving optimal resolution. b) When the sample has roughness comparable or in excess of the tip, multiple sources can contribute to the image.

Just as in the case of the STM, a blunt AFM tip can also be used to image the atomic corrugations of flat samples simply by relying on the presence of local asperities. The first AFM to obtain images of atomic corrugations used a flat cantilever lacking any extra tip (Figure 2.2) [2]. In AFM, the problem of tip sharpness is greater than in the case of the STM. Since interatomic forces such as van der Waals and magnetic forces have relatively long decay lengths, from tens to hundreds of angstroms, the interaction between the tip and sample is rarely confined to a pair of atoms. Often the sample has

14
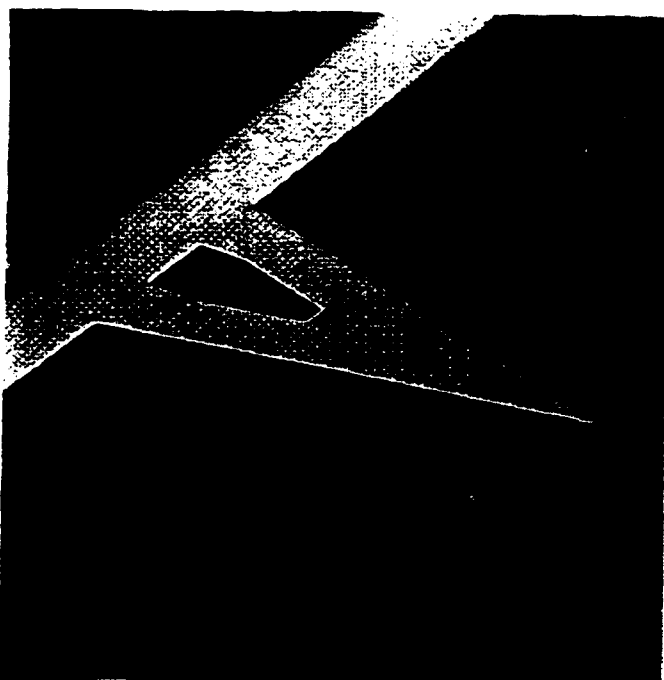
Figure 2.2 This silicon nitride AFM cantilever has no tip other than its
sharply tapered end. When used to image atomically flat samples
however, local asperities on the cantilever act as tips and allow the
imaging of atomic corrugations. The cantilever is 100 μm long and 0.7
μm thick.

features whose sharpness rivals that of the AFM tip and the resulting image can deviate

substantially from the actual surface topography. In Figure 2.3 a tip with finite radius, r,

is shown tracing a trench of width, w, with perfectly sharp corners. The observed

topography (dashed line), shows that the apparent width of the trench is the actual width

minus twice the tip radius. Since the edges of the trench are sharper than the tip itself, the

edge in effect begins to image the tip and the result is an apparent edge radius that is

actually the radius of the tip itself. In the case where w is less than $2r$ the tip does not

even reach the bottom of the trench.

15
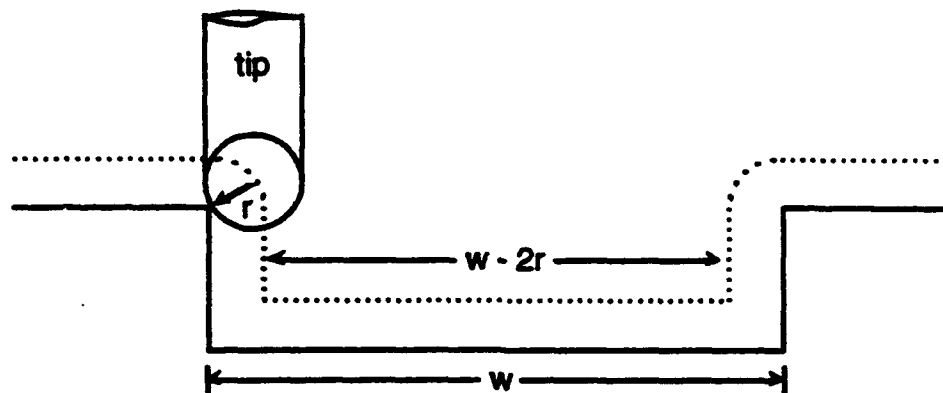
Figure 2.3 When a tip with finite radius is used to image a rough sample, the apparent topography is a convolution of the sample topography and the tip shape.

It is important to understand that the original topography of the surface cannot be retrieved by characterizing the tip shape or by deconvolving it with the image. In the process of tracing the sample surface with a blunt tip, information is actually lost. Figure 2.4 demonstrates graphically that the same tip imaging different samples can produce identical images. It would be impossible to distinguish between these three samples even if the tip shape were known exactly.

The first tips to be used on AFM cantilevers were not integrally formed with the cantilever but instead were attached to the cantilever after fabrication [3]. Attaching tips individually is a painstaking and irregular process which can be eliminated through the use of microfabrication to create tips which are integral to the cantilever. Since 1987, numerous processes for microfabricating tips have been demonstrated [4, 5, 6, 7]. In the following sections several of these tip fabrication techniques are discussed. They include demonstrated processes for conical, pyramidal, tetrahedral and truncated blade tips.
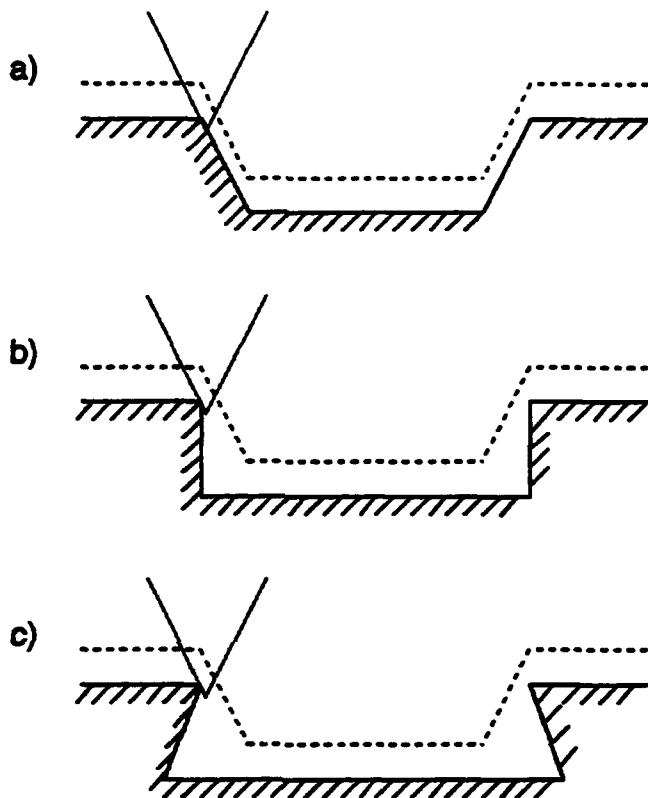
Figure 2.4 The true topography of a sample can not be calculated by deconvolving the measured imaged with the known tip shape. The measured image is not unique to one sample topography as demonstrated here.

In addition to sharpness, there are several other desired characteristics for AFM tips. Tips should have high aspect ratios in order to probe into deep trenches but they should not be so thin and whip-like that they are easily damaged or bent by lateral forces. Radial symmetry is desirable in order to obtain good images regardless of the cantilever's orientation with respect to the sample. If possible, the tips should point away from the

bulk of the substrate so that when they are fabricated on cantilevers, the substrate does not come into contact with the sample before the tip does. Tips which are self-aligned to the cantilever are advantageous since the location of the tip is not determined by the registration error in photolithography. Finally, if at all possible, tip fabrication processes should include or be compatible with sharpening processes not only to increase the sharpness of the tips but also to improve uniformity. The factors such as high aspect ratios, radial symmetry and orientation of the tip affect the image quality. The factors of self-alignment and compatibility with sharpening processes affect the manufacturability of the devices. Improving image quality and manufacturability are both goals of this research.

2.2   Conical Tips

A type of tip that has the shape of a right cone, like an inverted ice cream cone, and extends perpendicularly from the surface of a cantilever a few microns has come to be known as "conical tips". Conical tips are currently gaining popularity because they can be made from silicon and can therefore be sharpened using an oxidation sharpening technique to tip radii of less than 100 Å [8]. Their aspect ratio can be varied over a large range by modifying a few fabrication parameters. Conical tips are radially symmetric and point away from the surface of the wafer. They have two principal drawbacks, they are hard to make with high uniformity and they are not self-aligned to the cantilever. These minor shortcomings notwithstanding, conical tips seem destined to become the tip of choice for many AFM users.

2.2.1 Conical tip fabrication process

The fabrication process for conical tips is shown in Figure 2.5. The fabrication begins with the patterning of small circles of masking material (Figure 2.5 (a)). The masking material can be oxide, nitride, refractory metal or any other material that is not etched in the silicon etch. The thickness of the masking material depends on the desired height of the tip and the etch selectivity between the masking material and the silicon substrate. 2000 Å of oxide is sufficient to make 10 μm tall silicon tips and 100 μm tall tips can be made using 1000 Å of evaporated aluminum. Next, the wafer is etched in either a plasma or wet etchant. Although most of the etching occurs in the vertical direction, there is some finite undercutting of the mask. By carefully monitoring the etching process through periodic optical inspections, the etching can be stopped just prior to or just after the masking material caps have fallen off (Figure 2.5 (b)). If the etching time is too short, the tips are not fully tapered to a point at the apex but if the etching time is too long, the caps fall off and cease to protect the tip. If the tip is left in the etching environment without its protective cap, the tip is immediately attacked at its apex and rapidly loses its sharpness. In practice, when using plasma to etch the silicon, the caps usually fall off and come to rest against the tip as shown in Figure 2.5 (b) and thereby afford a few extra minutes of protection. In the final step of the fabrication process, the caps are selectively removed and the tips are exposed (Figure 2.5 (c)).
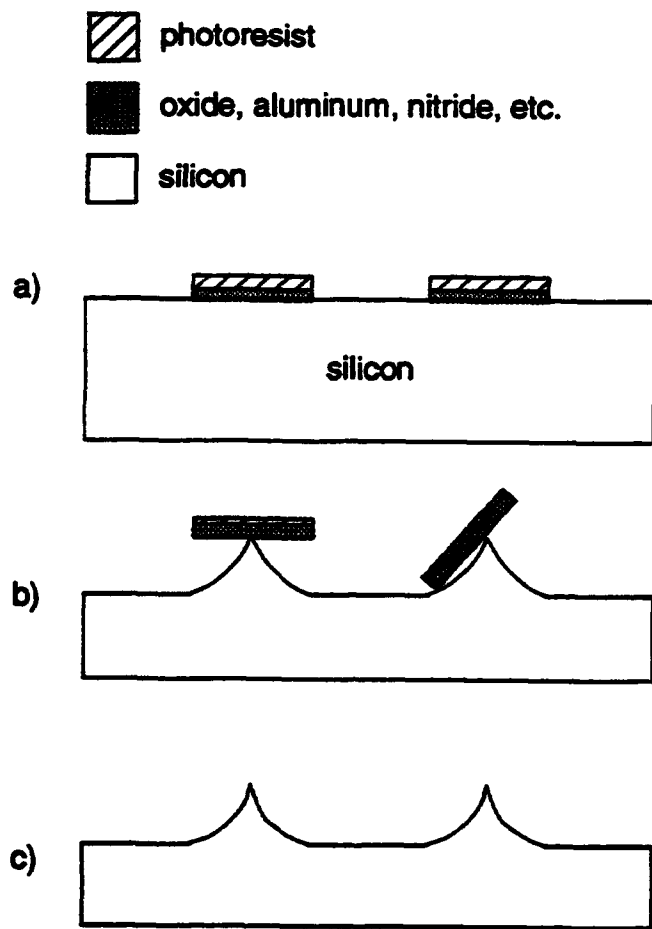
Figure 2.5 To fabricated conical tips a) a masking material such as oxide is patterned into circles. b) Dry or wet etching of the silicon undercuts the masking material and yields conical tips. c) To fully expose the tips, the masking material is selectively removed.

2.2.2 Oxidation sharpening of silicon tips

The most serious disadvantage of the conical tip process is that the etching conditions and durations are critical for the proper formation of tips. Since etching rates and durations are the two least controllable fabrication parameters, a fabrication process

that relies heavily on them is usually very difficult to reporduce from wafer to wafer or even across a single wafer. Plasma etching is very non-uniform so that the tips in the center may take longer to form than the tips at the perimeter of the wafer. If wet etching is used, the etch time becomes more critical since the caps are washed away in the etchant and the tips are quickly attacked.

In order to make the tips sharper and at the same time increase their uniformity, silicon conical tips can be sharpened using a low temperature thermal oxidation process [8]. This sharpening process is quite simple and elegant. By using this technique, it is possible to make many tips with radii less than 100 Å with good uniformity. After the tips are formed, they are thermally oxidized at 950 °C to form an oxide layer 2000 Å to 1 μm in thickness. When the oxide is selectively removed in a HF acid solution, the resulting silicon tips are sharper and have higher aspect ratio than they had prior to oxidation. The mechanism of oxidation sharpening process is described in detail elsewhere [9, 10], but it can be understood from a brief explanation.

When silicon is thermally oxidized, it expands. Due to geometric factors, the oxide in highly convex regions can not expand as fully as the oxide grown in flat regions. When the oxide can not fully expand, stress builds up in the film and reduces the diffusivity of incoming oxidizing species. Since thick oxide formation is a diffusion limited process, the reduction in diffusivity results in a slower oxidation rate in convex as compared to flat regions. The net effect of these factors is that the silicon on the sidewalls of the tip tends to oxidize more rapidly than silicon at the apex of the tip. The consumption of silicon preferentially from the sidewalls has the effect of increasing the tips' aspect ratios and reducing their tip radii. Although the conditions exist to produce this phenomenon using other substrate materials such as iron, the only oxidation

21

sharpened AFM tips demonstrated to date have been made from silicon. A slightly different oxidation sharpening process discussed in Section 2.3.2 has been used to make sharp tips of silicon nitride.

2.3 Pyramidal Tips

Pyramidal tipped cantilevers are the most widely used AFM cantilevers in the world. They were initially favored for two reasons, their uniformity and their radial quasi-symmetry. Their numerous disadvantages include the fact that without sharpening, they are can rarely be made much sharper than 500 Å radius of curvature, they are not self-aligned, their aspect ratio is approximately 0.5 and when first fabricated, they point into the bulk of the substrate. All of these disadvantages however are counterbalanced by three factors: the relative ease of fabricating the pyramidal tips, the development of a method for flipping the tips upside-down onto a second substrate [4] and the demonstration of a technique to sharpen the tips to 100 Å radius [11].

2.3.1 Pyramidal tip fabrication process

The fabrication of the pyramidal tip begins with the patterning of small square windows into a masking material on a (100) silicon wafer (Figure 2.7 (a)). The windows are oriented so that their sides are parallel to (110) planes in the silicon wafer. The masking material can be oxide, nitride, heavily doped silicon or various metals. The exposed silicon is then etched in an anisotropic etchant such as a potassium hydroxide (KOH)/water or an ethylenediamine/pyrocatechol (EDP)/water solution [12].
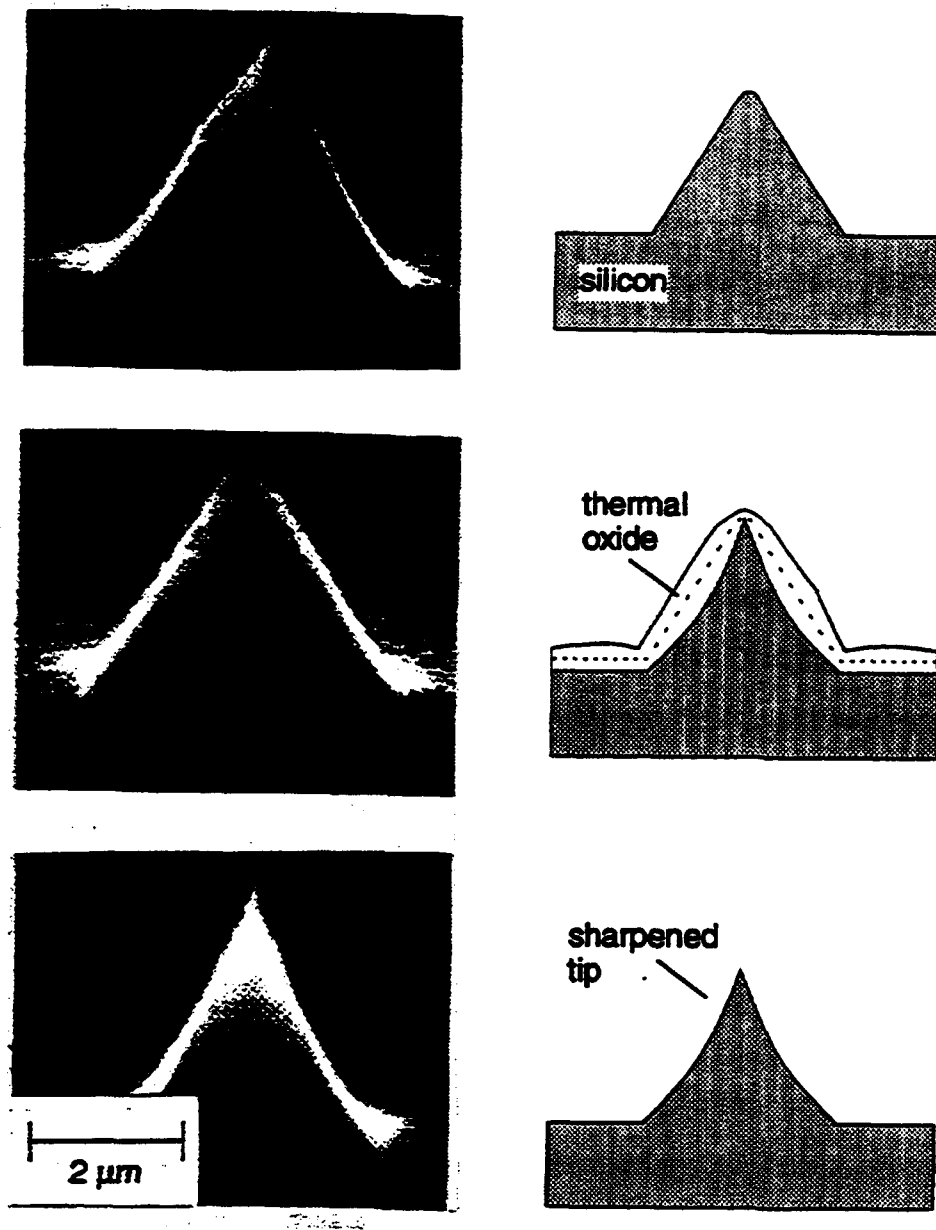
Figure 2.6 a) Conical tips after initial fabrication vary in sharpness across
the wafer and have typical radii of curvature of approximately 500 Å. b)
When the tip are oxidized at 950 °C to yield several thousands of
angstroms of oxide, the oxide growth is non-uniform. c) When the non-
uniform oxide is selectively removed, the resulting silicon tips can have
radii of curvature less than 100 Å.

These etchants etch silicon in the [100] direction up to 400 times faster than the [111] directions [12] therefore when the silicon in these windows is etched the etching is very rapid in the vertical direction but slows down almost to a stop when a (111) plane is encountered. Since silicon has a diamond-like crystal structure, after a certain amount of etching in the [100] direction, the pit terminates with the meeting of four (111) planes. The resulting pit has the shape of a pyramid with its apex pointing downward into the bulk of the substrate (Figure 2.7 (b)). The tip is formed by casting the desired tip material into the pyramidal pit and therefore this fabrication technique is sometimes referred to as a microcasting technique (Figure 2.7 (c)). The tip material can be oxide, nitride, polysilicon, metal or heavily boron doped single crystal silicon. Once the tip material has been deposited the tip can be transferred to a Pyrex glass substrate by anodic bonding if it is desired, as in AFM, that the tip point away from the bulk of the substrate (Figure 2.7 (d)) [4]. The original silicon substrate is selectively removed by etching again in KOH or EDP and the tip is fully exposed (Figure 2.7 (e)).

2.3.2 Sharpening of microcast tips by low temperature oxidation

Sharper tips with slightly higher aspect ratios are obtainable using the microcasting technique in which the interior contour of the pyramidal pit is first modified by a low temperature silicon oxidation (Fig. 2.9). Like the oxidation sharpening process described in Section 2.2.2, the microcast sharpening process also relies on the non-uniform growth rate of low temperature thermal oxide. In this case however, the process utilizes thin oxides at concave regions not the convex regions of the previous process.

a)

silicon (100)

oxide or
nitride

b)

[111]

oxide or
nitride

c)

d)

e)
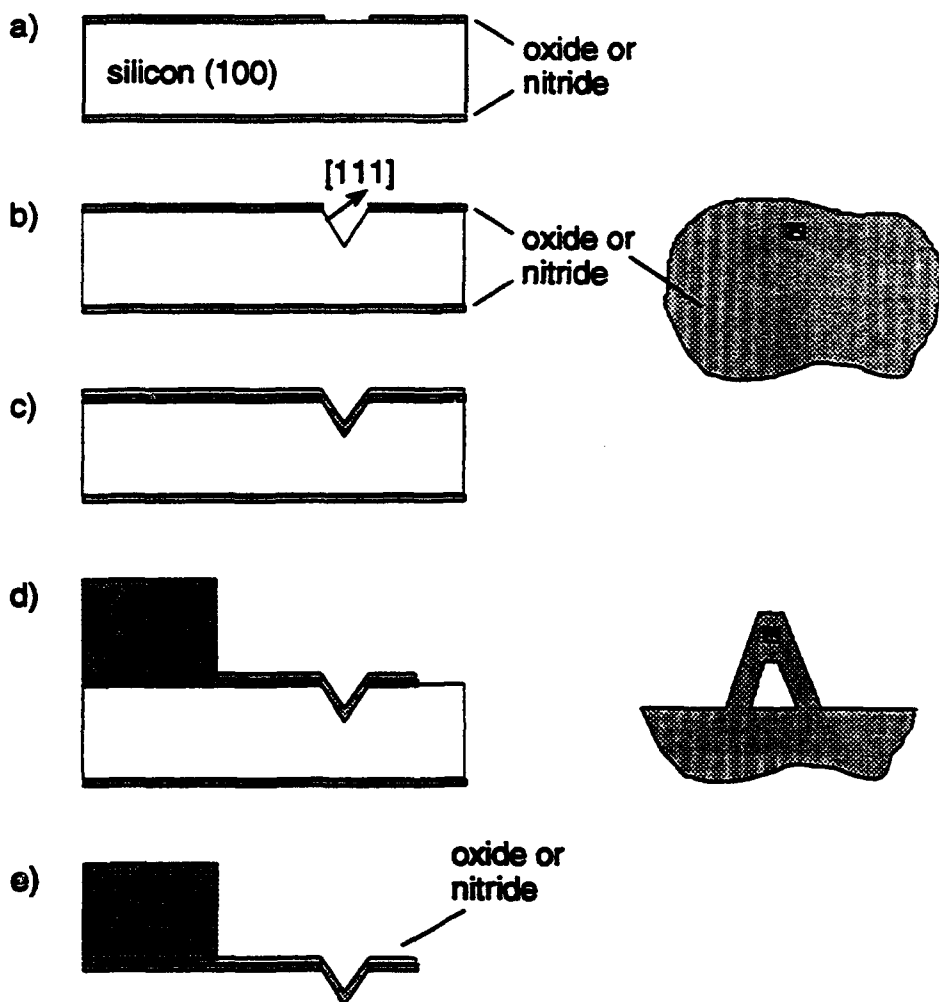
oxide or
nitride

Figure 2.7 a) The pyramidal tip fabrication process begins with the patterning of a small square aperture in an oxide or nitride masking material on a (100) silicon wafer. b) Anisotropic wet etching creates a pyramid shaped pit whose sidewalls are (111) planes. c) The desired cantilever and tip material are cast into the mold. d) A cantilever is patterned and bonded to a second substrate such as Pyrex 7740. e) The silicon substrate is selectively removed to leave a free-standing cantilever with integral pyramidal tip.

Figure 2.8 Unsharpened pyramidal tips can be formed integrally on
AFM cantilevers. Their unsharpened radii of curvature is approximately
500 Å.

By patterning the tip material it is possible to form cantilevers with integral
pyramidal tips such as the one shown in Figure 2.8 [4].

The mechanism for the depressed oxidation rate in concave regions is slightly
different from the mechanism in the convex regions. In the concave regions, the oxide
growth rate is depressed by geometrical factors. Due to the concavity, the surface area
available for accepting incoming oxidizing species is smaller than the surface area of the
silicon available for reaction at the silicon/oxide interface. The density of oxidizing

species is smaller therefore in concave areas than flat areas and the oxidation rate is correspondingly depressed. This effect is responsible for observations of thinner oxide films at edges of ridges and in the corners at the bases of vertical walls. At high oxidation temperatures, above 1050 °C typically, this effect is not as pronounced since the oxide undergoes viscous flow and smoothes out areas of high concavity [9, 10].
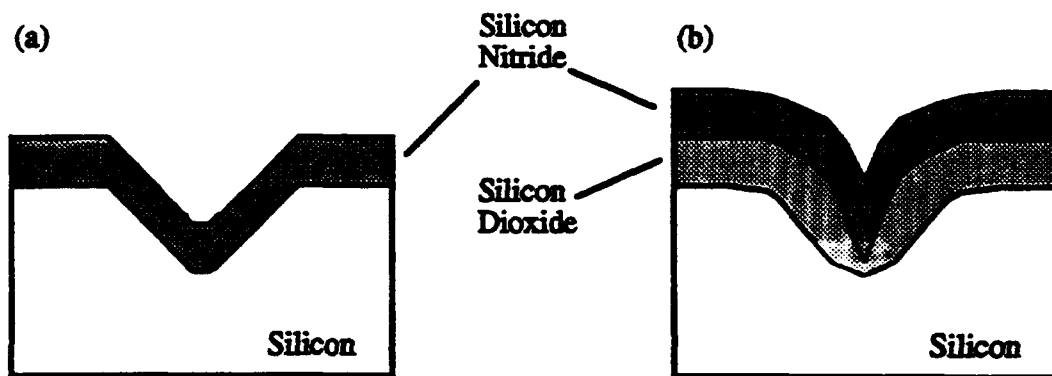
Figure 2.9 a) In the standard pyramidal tip fabrication process, a pyramidal pit is etched into a (100) silicon wafer and the tip material is cast directly into the cavity. b) In the microcast sharpening process, the interior contour of the pyramidal pit is first modified by a non-uniform thermal oxide before the tip material is cast. The resulting tips are sharper and have higher aspect ratios.

To determine the sharpening characteristics of the microcast sharpening technique, an experiment was conducted making pyramidal tips using various thicknesses of oxide all grown at 950 °C [11]. Other than the inclusion of the oxide layer, the process used is identical to that of conventional pyramidal tips. Several nitride coated (100) silicon wafers were photolithographically patterned with squares varying in size from 2 to

25 microns. An SF_6 and C_2ClF_5 plasma was used to transfer the pattern to the nitride film. The silicon in the exposed squares was etched in a KOH and water solution (30% by weight) at 60 °C for 2 hours using the nitride film as a masking material. The etch rate of silicon dioxide and silicon nitride in the KOH solution is less much than 50Å/minute. At this temperature, the etch rate of silicon in the [100] direction is approximately 0.4 microns/minute [13]. In order to ensure that the pyramidal pits would all be terminated as much as possible by intersecting (111) planes the etch time used was 100% greater than would be necessary for the formation of 25 micron deep pyramidal pits. The etch was done at 60 °C to enhance the anisotropy ratio between the etch rates in the two directions even further in hopes of obtaining a sharper pyramid than would have resulted by etching at 80 °C. At 80 °C, KOH etches silicon in the [100] direction approximately 400 times faster than in the [111] direction and the anisotropy of the etch increases exponentially with decreasing temperature.

After the pyramidal pits were formed, the wafers were separated and silicon dioxide films of varying thicknesses were grown on each wafer in steam at 950 °C. Target oxide thicknesses ranged from 0 Å to 10,000 Å in increments of 2000 Å. The actual thicknesses obtained are as follows: 0 Å, 1830 Å, 3890 Å, 5240 Å, 7820 Å and 9500 Å. The oxide thicknesses were measured on the (100) wafer surface in a region far from a pit using a Nanospec optical interferometer system. The wafers were then all cleaned simultaneously in a modified RCA cleaning process including a 30 second etch in 50:1 buffered oxide etch (BOE). The exposure to the BOE was brief but may have resulted in a slight modification of the oxide surface contour of each sample. Next, 2000 Å of silicon nitride were deposited on all the wafers by low pressure chemical deposition (LPCVD) at a deposition temperature of 775 °C. Large rectangular openings were

patterned on the back sides of the wafers and the exposed silicon was etched in KOH solution completely through the wafers leaving only membranes composed of silicon nitride and silicon dioxide at the front surface of the wafers. After the silicon etch was completed, the inverted nitride and silicon dioxide pyramids could be seen directly with an optical microscope. The oxide was then selectively removed from each wafer by etching in 6:1 BOE for a period appropriate for completely etching the oxide on each wafer plus an additional, fixed time of 3 minutes for each sample including the sample which had no thermal oxide. After the oxide was removed, 100 Å of gold were sputtered on both sides of the silicon nitride membranes to reduce charging in the scanning electron microscope (SEM).

A SEM equipped with a sample stage which held all samples at the same, fixed angle was used to examine the samples. Carbon contamination can build up on the sample quickly during high magnification imaging in the SEM; therefore, it is important to obtain photos of the samples quickly before the contamination can significantly alter the shape of the tip under study. Before making detailed examinations of a sample, the tip uniformity over the sample was confirmed by imaging approximately 20 tips. Focusing closely on a single tip, the beam astigmation was corrected and the photo exposure time was determined. The definitive photograph was taken of an adjacent tip so as to minimize the tip's exposure to the electron beam. The radii of curvature and the aspect ratios of the tips were measured from the photographs. We define the aspect ratio as the ratio of the last 1000 Å in height of the tip to the full width of the tip at a point 1000 Å down from its apex. The 1000 Å value was chosen because it is relevant to the mesoscopic structures which lie between the angstrom scale of atomic features and the micron scale of macroscopic structures.
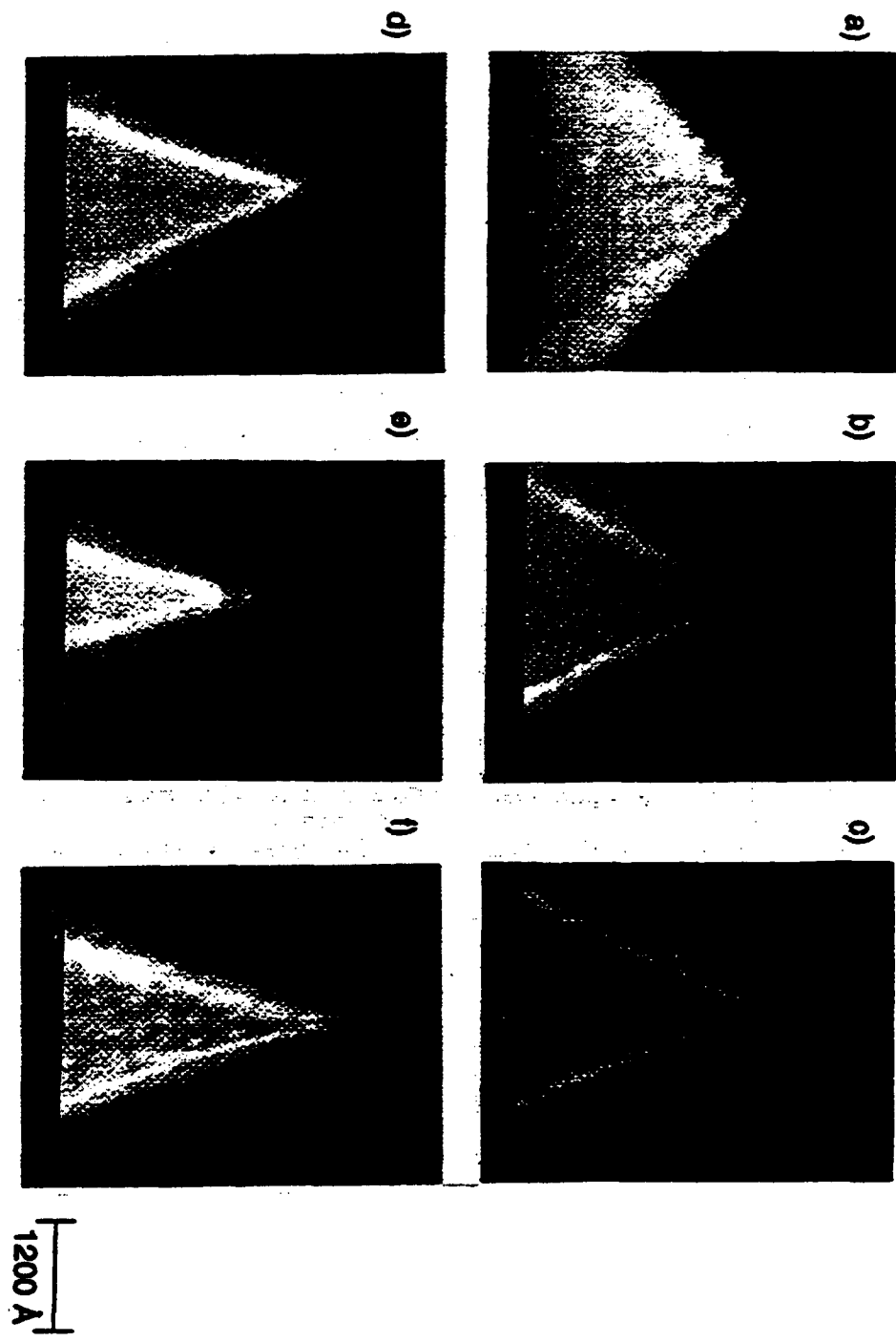
Figure 2.10 a) Tip A had no oxide and a 450 Å radius tip. b) Tip B had 1830 Å of oxide and a 250 Å radius tip. c) Tip C had 3890Å of oxide and was the sharpest tip. Its radius is 110 Å. d) Tip D had 5240 Å of oxide and a 130 Å radius tip. e) Tip E had 7820 Å of oxide and a 180 Å radius tip. f) Tip F had 9500 Å of oxide and a 240 Å radius tip.

Tip	Oxide Thickness	Tip Radius	Aspect Ratio
A	0 Å	450 Å	0.36
B	1830 Å	250 Å	0.64
C	3890 Å	110 Å	0.95
D	5240 Å	130 Å	1.0
E	7820 Å	180 Å	1.0
F	9500 Å	240 Å	1.0

Table 2.1 The oxide thicknesses used to fabricate microcast sharpened tips are shown in this table. The tip radii and aspect ratios were measured from SEM photos.

SEM photographs of the resulting tips are shown in Figure 2.10 (a - f) and measured parameters are listed in Table 2.1. Tip A has an aspect ratio which is 51% lower than the value of 0.7 calculated from a simple geometric consideration of a pyramidal pit bounded by four (111) planes. On the sample containing Tip B, two distinct types of tip shapes were observed. Approximately 30% of the tips terminated in a single point as does the tip in Figure 2.10 (b) but the remainder of the tips, even those directly neighboring this one, terminated in a cleft shape with two points separated by a slight indentation. This may have been due to the oxide faces from the sidewalls barely meeting in some of the pits while not quite meeting in others. Another cause of these cleft tips may have been that the pyramidal pits terminated not at a point but rather in a knife blade structure causing a cleft shaped tip with sharp horns corresponding to each

31

end of the original knife blade. This appears unlikely however since knife blade tips were not observed on any of the other samples.

The sharpest tips were fabricated in molds that had 3890 Å of oxide. Tip C in Figure 2.10 (c) is representative of these tips, having a radius of curvature of 110 Å and an aspect ratio of 0.95. Over 95% of the tips examined on this sample had similar radii of curvature. All the tips in this study were covered with 100 Å of sputtered gold before imaging in the SEM, so the actual radii of curvature of these tips may be lower than those measured from these SEM photos.

The graph in Figure 2.11 shows the trends for the radius of curvature and aspect ratio as a function of the oxide thickness. The radius of curvature drops significantly from a radius of 450 Å for no oxide to 110 Å for oxide thickness of up to 3890 Å. Beyond that oxide thickness, the radius actually begins to rise slightly. The aspect ratio follows a similar trend, improving rapidly for oxide thicknesses of 0 Å to 3890 Å and flattening out thereafter. The fact that both curves turn over at an oxide thickness around 3890 Å may be indicative of the meeting of the oxide faces from the sides of the pyramidal pit. The optimal oxide thickness is probably determined by the geometry of the original pit.

A composite tip of oxide and nitride can be fabricated if the oxide is only partially removed from the nitride tip (Figure 2.12). If a conductive material such as polysilicon or metal were used in place of the nitride, an insulated tip with a conductive center would result. Such a tip could be useful in applications such as scanning electrochemical microscopy [14] or scanning ion conductance microscopy [15].
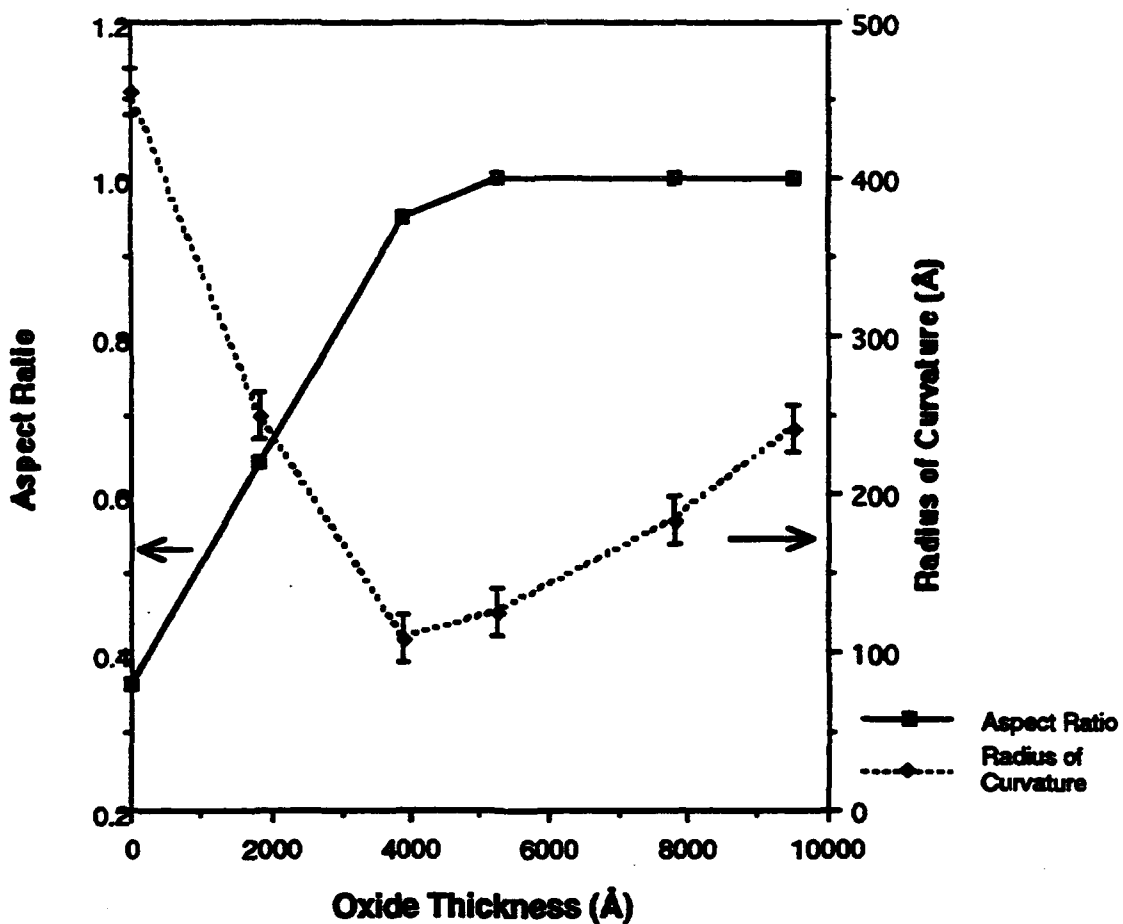
Figure 2.11 The tips' radii of curvature drops suddenly with increasing oxide thickness before reaching a minimum at an oxide thickness of approximately 3890 Å. The aspect ratios rise to a value of 1 which is higher than the geometrically predicted value of 0.7.

If the silicon nitride were selectively removed from the center while leaving the oxide covering, a hollow tip could be fabricated for use in applications such as near-field optical microscopy [16, 17] and biological microscopy where micro pipettes are presently being used.
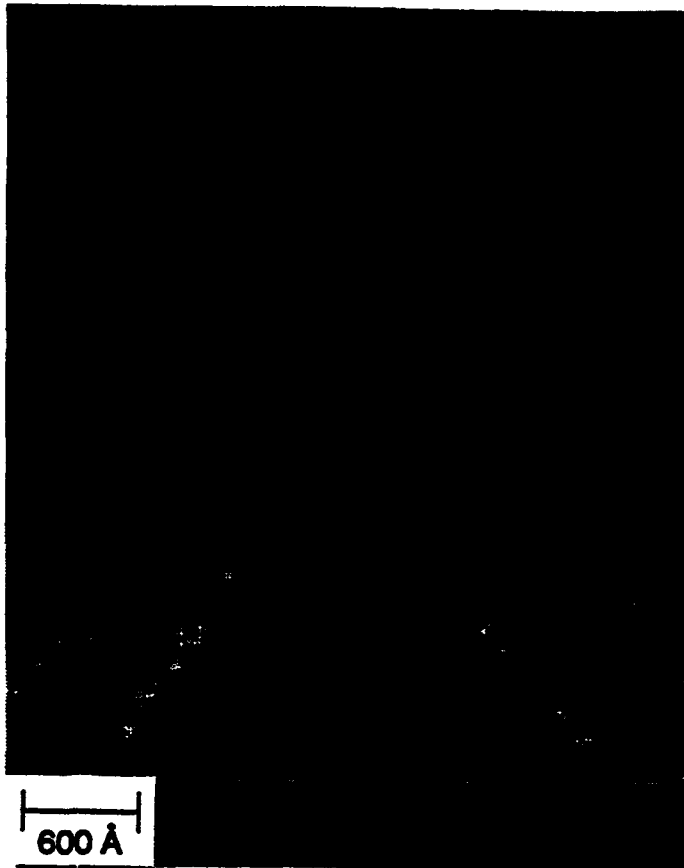
Figure 2.12 By selectively removing only part of the oxide film, it is
possible to fabricate a composite tip that may be useful in other types of
microscopy such as scanning electrochemical or near-field scanning
optical microscopy.

The microcast sharpening technique allows tips to be fabricated with a very
simple process without unduly sacrificing sharpness or uniformity. While pyramidal pits
were used as molds in this work, Akitoshi Toda and coworkers at Olympus Optical
Company have demonstrated that the cylindrical pits can be used to form conical tips
with radii of curvature of 100 Å or less [18]. This technique of sharpening tips cast from

various materials may find applications in other research areas such as microvacuum electronics.

2.4   Tetrahedral Tips

Tetrahedral tips are single crystal silicon tips which are made using a combination of anisotropic dry and wet etches. The principal advantages of the tetrahedral tips are that tetrahedral tips have higher aspect ratios than pyramidal tips, point away from the bulk of the substrate as fabricated, are self-aligned and are self-sharpened to as low as 100 Å radii of curvature. This section describes the fabrication of the tips alone while Chapter 3 describes the fabrication of tetrahedral tips on nitride cantilevers and their use in AFM.

The fabrication process begins with the deposition of nitride on a silicon (100) wafer. A post with sharp corners pointing in the <100> directions is plasma etched into the silicon using the nitride and photoresist as masking materials. The wafer is then thermally oxidized at 950 °C such that the exposed silicon everywhere is covered with oxide but the nitride cap is unaffected (Figure 2.13 (a)). The nitride cap is selectively removed in hot phosphoric acid or in a SF_6/CF_3Br plasma. After the etch, the silicon interior of the post is exposed from the top only (Figure 2.13 (b)). The interior of the post is etched using a wet anisotropic etchant such as KOH or EDP. These etchants can not effectively attack the tetrahedral volumes in the corners of the posts since these volumes are bounded on their sides by oxide and on their face by silicon (111) planes (Figure 2.13 (c)). The tips are finally exposed by the selective removal of the oxide sidewalls in an HF solution.

It is sometimes assumed that the tetrahedral tips' sharpness is limited by the resolution of the lithography process used to pattern the initial post. This is not the case

however since the posts' sidewalls are thermally oxidized at a low temperature to induce the non-uniform oxide growth discussed in Section 2.2.2. As in the case of the conical silicon tips, the non-uniform oxide growth sharpens the corners of the post to a sharp blade since the corner represents highly convex regions. The apex of a tip is therefore defined by a (111) plane intersecting a very sharp vertical edge at the corner of a post (Figure 2.13 (b)). When fully formed, if further sharpening is desired, the tips can be oxidized again to undergo further oxidation sharpening.

2.5 Truncated Blade Tips

Truncated blade tips are similar in shape to tetrahedral tips but they extend from the edge of the wafer rather than extending perpendicularly from its face. Although sharp, with tip radii as low as 200 Å, because of their geometry truncated blade tips have yet to be used in any microscope.

They are fabricated by forming a blade structure on one side of the wafer and then truncating the blade with an intersecting (111) plane, exposed by wet anisotropic etching. The resulting tip juts out from the edge of the wafer and has a shape roughly defined by the intersection of three (111) planes.

To fabricate a truncated blade tip it is first necessary to create a sharp blade structure. Although a blade can be made by using undercutting as done in the conical tip fabrication process, this method as previously described is not highly desirable since the masking material can fall off and overetching of the blade can result.

Instead, blade structures can be made by patterning a large straight-edged feature into a nitride film. When etched in a wet anisotropic etchant, the side profile looks as shown in Figure 2.15 (a).

36
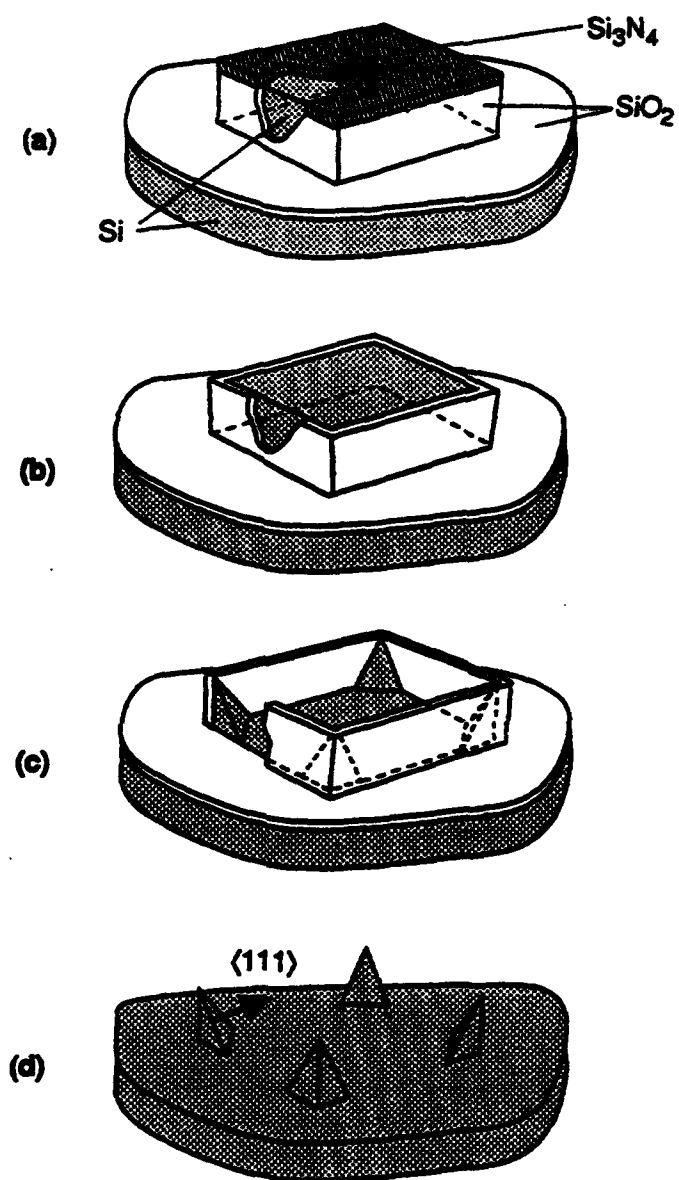
Figure 2.13 a) A vertical-walled post with nitride top and oxide sidewall is fabricated by plasma etching and thermal oxidation. b) The nitride cap is selectively removed to expose the silicon interior. c) The silicon is anisotropically etched in a wet etchant such as KOH or EDP. d) The oxide sidewalls are selectively removed to expose the tip.

37

Fully formed tetrahedral tips are shown in Figure 2.14. By varying the size and shape of the original post, differing configurations of tips can be made. The tips are self-aligned to the corners of the posts and they point away from the bulk of the substrate. A further advantage of the tetrahedral tip fabrication process is that it does not rely on any critical etching steps. If the wet etch is done for too long, the height of the tip increases but its shape does not change. This makes the tetrahedral tip fabrication very robust and reproducible.

10 μm

Figure 2.14 Tetrahedral tips can be formed from posts of varying sizes.

The wafer is then thermally oxidized, at 950 °C if sharpening is desired (Figure 2.15 (b)). The nitride is selectively removed and the exposed silicon is etched in an

a)

[111]

silicon (100)   nitride

b)

thermal oxide

c)

[111]

d)
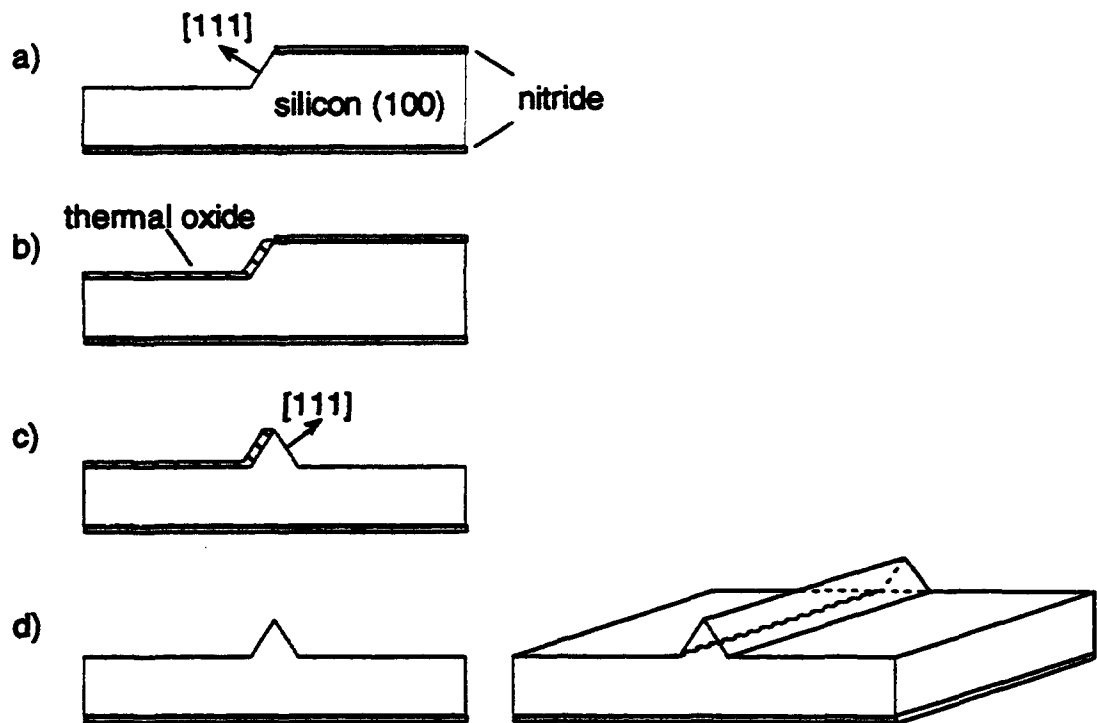
Figure 2.15 a) A nitride mask is patterned to have a long straight edge
parallel to the {110} planes. The exposed silicon is then wet
anisotropically etched. b) The exposed silicon is thermally oxidized. c)
The nitride is selectively removed and the newly exposed silicon is
anisotropically etched. d) The fully formed blade structure is revealed
when the oxide is removed.

anisotropic etchant (Figure 2.15 (c)). When the oxide is selectively removed, a blade-like
structure is left (Figure 2.15 (d)).

This method of making blades is more reproducible than the undercutting
technique since overetching only changes the relative heights of the flat areas adjacent to

the blade structure but does not result in additional etching at the apex of the blade. In addition, the low temperature oxidation step can sharpen the blade.

Once the blades have been formed, they are protected by either a thermal oxide or LPCVD nitride layer. Then large windows are patterned from the backside of the wafer and etched in an anisotropic etchant. The anisotropic etchant forms a pit whose sides are bound by (111) planes and when these planes intersect the blade at the front surface of the wafer, a tip is formed at the intersection of the three (111) planes (Figure 2.16). These tips are highly reproducible and can be quite sharp as shown in Figure 2.17 (a, b).
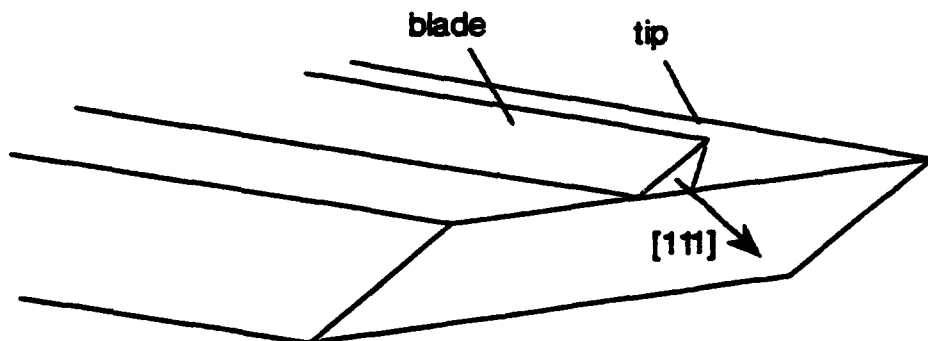
Figure 2.16 Truncated blade tips are formed at the intersection of three (111) planes.

a)

b)
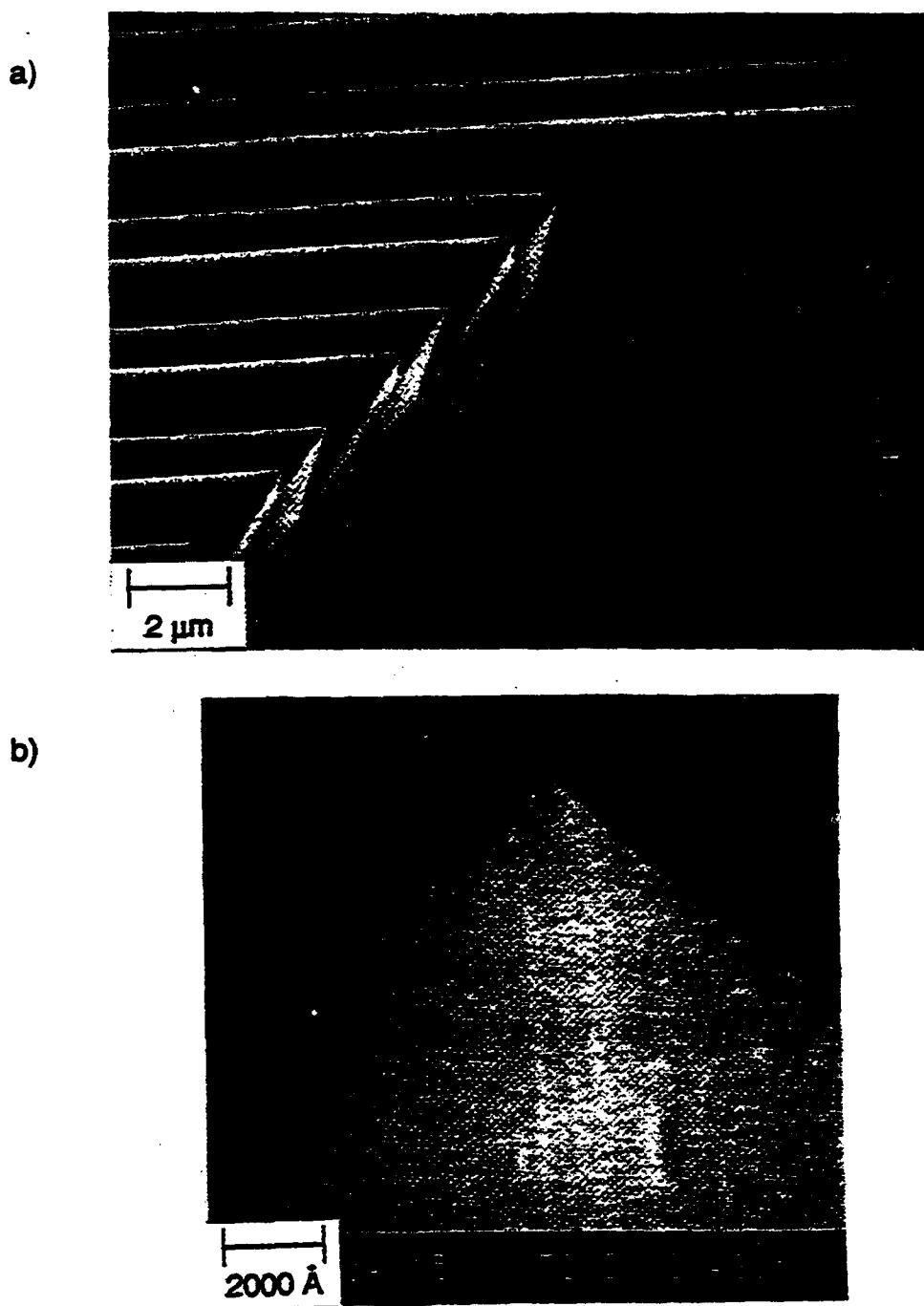
Figure 2.17 a) The truncated blade tips are highly reproducible. b) The radius of curvature of this tip is 170 Å even after being covered with 100 Å of sputtered gold for SEM imaging.

41

References

1)   G. Binnig, H. Rohrer, C. Gerber and E. Weibel, Phys. Rev. Lett. **50**, 120 (1983).

2)   T. R. Albrecht and C. F. Quate, J. Vac. Sci. Technol. A **6**, 271 (1988).

3)   T. R. Albrecht, Ph. D. dissertation, Stanford University (1989).

4)   T. R. Albrecht, S. Akamine, T. E. Carver, and C. F. Quate, J. Vac. Sci. Technol. A **8**, 3386 (1990).

5)   S. Akamine, R. C. Barrett, and C. F. Quate, Appl. Phys. Lett. **57**, 316 (1990).

6)   R. A. Buser, J. Brugger, and N. F. de Rooij, Microelectr. Engrg. **15**, 407 (1991).

7)   O. Wolter, T. Bayer, and J. Greschner, J. Vac. Sci. Technol. **39**, 1353 (1991).

8)   R. B. Marcus, T. S. Ravi, T. Gmitter, K. Chin, D. Liu, W. J. Orvis, and D. R. Ciarlo, C. E. Hunt and J. Trujillo, Appl. Phys. Lett. **56**, 236 (1990).

9)   R. B. Marcus and T. T. Sheng, J. Electrochem. Soc. **129**, 1278 (1982).

10)   D. Kao, Ph. D. dissertation, Stanford University (1986).

11)   S. Akamine and C. F. Quate, J. Vac. Sci. Technol. B **10**, 2307 (1992).

12)   K. E. Peterson, Proc. IEEE **70**, 420 (1982).

13)   B. E. Burns, Ph. D. dissertation, Stanford University, 1987.

14)   M. V. Mirkin, F. R. F. Fan, and A. J. Bard, Science **257**, 364 (1992).

15)   C. B. Prater, P. K. Hansma, M. Tortonese, and C. F. Quate, Rev. Sci. Instrum. **62**, 2634 (1991).

16)   U. C. Fischer, U. T. Durig and D. W. Pohl, App. Phys. Lett. **52**, 249 (1988).

17)   E. Betzig, J. K. Trautman, T. D. Harris, J. S. Weiner, and R. L. Kostelak, Science **252**, 1468 (1991).

18)   A. Toda, private communication.

Chapter 3   Atomic Force Microscopy Using Cantilevers With Tetrahedral Tips

3.1   Atomic Force Microscopy Using Cantilevers With Tetrahedral Tips

In AFM a force-sensing cantilever is brought into close proximity of a sample so that very small forces between the cantilever and the sample can be detected. The force is measured by monitoring the displacement of the cantilever that has a known force constant. A two-dimensional mapping of surface forces can be obtained if the sample is scanned under the tip in a raster fashion. While its lateral resolution is not as high as that of the STM, the AFM has at least one advantage over STM which is its ability to image insulators as well as conductors. This makes AFM ideal for investigation of atomically flat samples [1], integrated circuit devices [2], polymers [3], biological specimens [4] and other samples which have relatively poor conductivity.

The force-sensing cantilever is a crucial component in all AFMs. Microfabricated cantilevers are ideal for use in AFM since they have both low force constants and high mechanical resonance frequencies. [1,5] Microfabricated cantilevers without tips can be used to image atomically flat samples since there exits some asperities which serve as local tips even on flat cantilevers. The need for a sharp tip with a high aspect ratio arises when samples with rough surfaces are imaged. When imaging rough samples with a flat cantilever, multiple asperities can interact with the sample in different locations and create a

image comprised of multiple signal sources. These artifacts are most pronounced in areas of the sample that have vertical walls and deep trenches.

In the past, researchers have used sharpened wire cantilevers [6], flat microcantilevers without tips, or cantilevers with tips attached by hand [4]. More recently, methods for microfabricating cantilevers with sharp, integral tips have been presented [7, 8, 9, 10]. The cantilever with tetrahedral tip presented in this chapter has numerous advantages over most of the previous designs. The tetrahedral tip can have radius of curvature less than 100 Å due to the sharpening effect of a low temperature thermal oxidation process that is an inherent part of the device fabrication process. The tetrahedral tip is very regular and reproducible since its shape is determined by well-controlled dry etching processes and silicon crystallographic geometry. The tetrahedral tips are made using a self-aligned process that ensures that each tip is formed only at the very end of each cantilever. Finally, the tetrahedral tip can be integrally fabricated on a silicon nitride cantilever. Silicon nitride is an ideal cantilever material since its yield strength of 14×10^{10} dynes/cm^2 is roughly twice that of silicon dioxide or single crystal silicon [11].

3.2   Tetrahedral Tipped Cantilever Fabrication Process

The process for fabricating a self-aligned, tetrahedral, single crystal silicon tip on a dielectric cantilever is shown in detail in Figure 3.1.
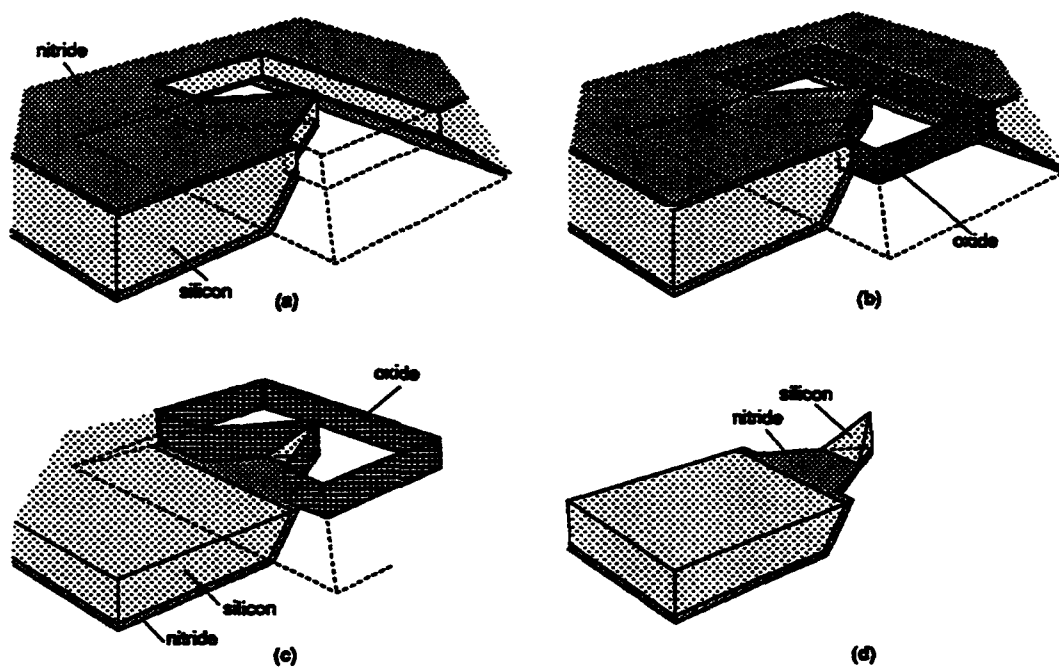
Figure 3.1 a) The process for creating cantilevers with integral tips begins
with the fabrication of a free-standing silicon and silicon nitride cantilever.
b) Exposed silicon surfaces are selectively oxidized. c) The nitride is
removed from the front of the wafer and the exposed silicon is
anisotropically etched leaving a tetrahedral volume at the end of the
cantilever. d) Selective removal of the silicon dioxide exposes the finished
cantilever with integral, self-aligned tip.

A thin silicon membrane is created by wet, anisotropic etching of a lightly doped (100) orientation silicon wafer. The etching is done using a solution of KOH and water. The wafer is then coated with a low stress silicon nitride film deposited using a low pressure chemical vapor deposition (LPCVD) process. Next, a cantilever is effectively carved out of the silicon and nitride membrane by masking with a photoresist layer and etching vertically in a dry etcher. At this point, the freestanding cantilever is comprised of a sandwich of the nitride films surrounding a silicon center. Thermally oxidizing the cantilever at 950 °C long enough to grow approximately 4000 Å of oxide causes the exposed silicon at the sides of the cantilever to be oxidized but does not modify either nitride surface. Next, the nitride layer on the top of the wafer is removed using an anisotropic plasma etch consisting of SF_6 and CF_3Br. Selectively removing the top nitride layer exposes the silicon interior of the cantilever from the top surface only. The bottom surface is still protected by the lower nitride layer and the sidewalls are protected by the thermal silicon dioxide. When the cantilever is etched again in the anisotropic KOH etchant, the silicon portion of the cantilever etches but only from the exposed top surface of the cantilever and neither from the sides nor the underside. At a rate of approximately 1 μm/minute, the wet etchant completely etches the silicon portion of the cantilever leaving a tetrahedral volume of silicon at the end of the cantilever that is bounded by the silicon nitride on the bottom, oxide on the sidewalls, and a (111) silicon crystal plane. The tip is completely exposed by selectively etching the oxide sidewalls with buffered HF acid that etches the oxide without attacking the nitride or the silicon. For use in an optical or tunneling detection AFM, 40 Å of chrome and 400 Å of gold are evaporated on the backs of the cantilevers to increase their reflectivity and conductivity.
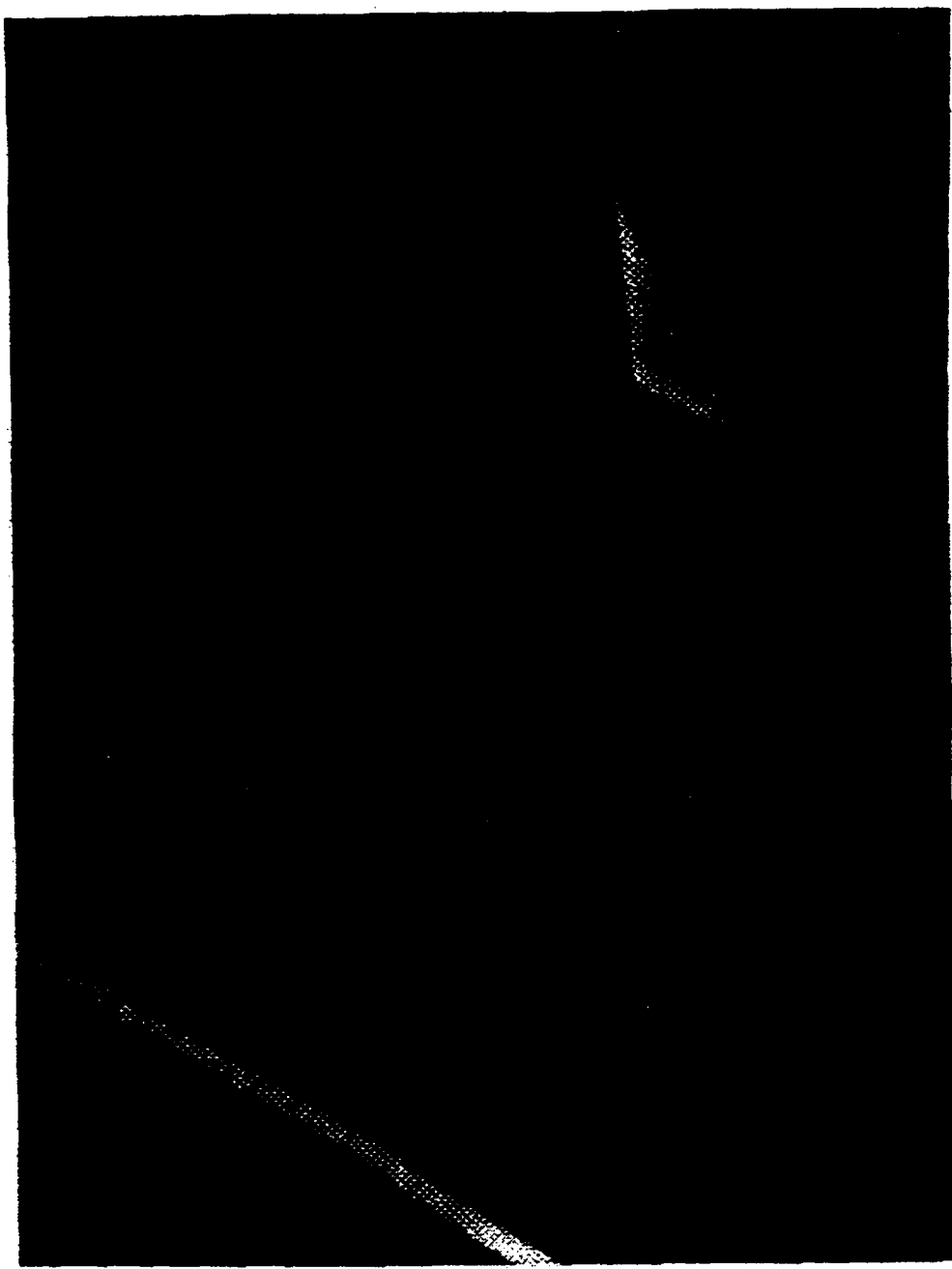
Figure 3.2 The single crystal silicon, tetrahedral tip can be microfabricated on an amorphous silicon nitride cantilever in a self-aligned, self-sharpening process. The cantilever is 100 μm in length and 0.7 μm in thickness.

a)

b)
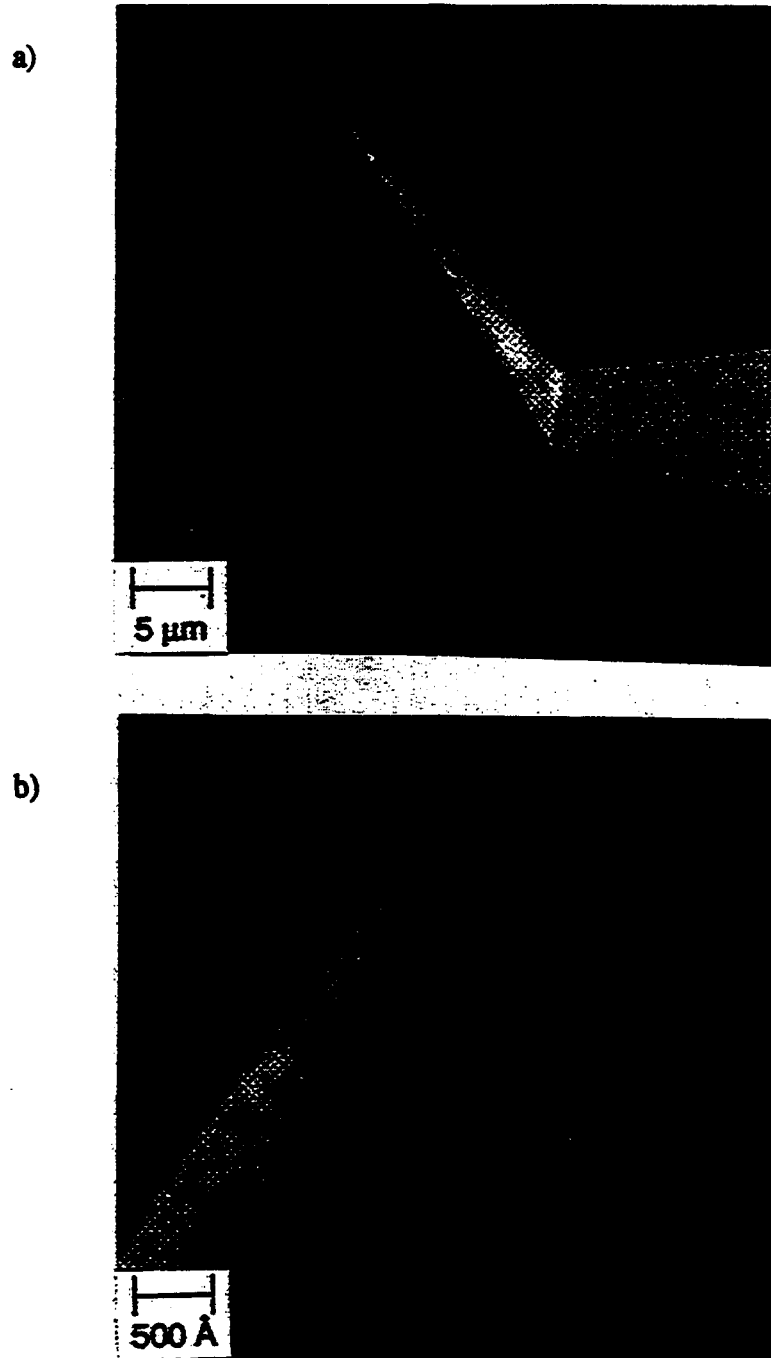
Figure 3.3 a) Since the tetrahedral tip is made of single crystal silicon it can also be oxidation sharpened. b) This photo shows a sharpened tip with less than 100 Å radius of curvature.

The chrome adhesion promotion layer must be kept as thin as possible to minimize the stress on the cantilever that can cause bending. A finished cantilever and tip are shown in Figure 3.2. If further sharpening is desired, tetrahedral tips on nitride cantilevers can be sharpened using the oxidation sharpening technique described in Section 2.2.2 (Figure 3.3).

3.3 Imaging with Tetrahedral Tips

The AFM results presented here were obtained using V-shaped cantilevers with dimensions of 100 x 22 x 0.7 μm. The calculated force constant for these cantilevers is 0.59 N/m and the measured resonant frequency is 78.7 kHz. The tip height is 5.6 μm. Most of the images were taken by Rob Barrett using an optical beam deflection AFM of his own design described elsewhere [12].

Cantilevers were evaluated by imaging samples of two distinct classes: atomically flat samples (highly-oriented pyrolitic graphite (HOPG) and Au(111) on mica [12]) as well as samples with rougher topographies (a 2.6 μm pitch diffraction grating etched in glass, a compact disk (CD) stamper and a vertical walled silicon grating of 6.25 μm period). The results of the atomic scale imaging experiments are presented in detail elsewhere [8] but one interesting effect bears noting here. It is known [6] that lateral forces are exerted on the cantilever during AFM imaging. When using cantilevers with relatively tall tips such as the tetrahedral tips, the lateral forces are magnified by the height of the tip. This can be understood by thinking of the tip as a lever arm. The taller the tip, the larger is the effective lever arm. Pronounced lateral bowing of the cantilever caused by lateral forces was observed by Rob Barrett even on atomically flat samples at forces of 10^{-7} N which are quite common in AFM.

To evaluate the performance of these tips on imaging large-scale structures, a 2.6 μm pitch, 750 Å deep diffraction grating was imaged with both the tipped cantilevers and identical cantilevers without tips. The images were taken in constant-force mode with an applied force of 10^{-8} N and a horizontal scan rate of 2 Hz. Figure 3.4 shows the improvement in imaging quality when tipped cantilevers are used. Images taken with the untipped cantilever lose lateral resolution near tall structures as the face or edge of the cantilever comes into contact with the sample. The addition of the tip on the cantilever provides enough clearance to allow faithful imaging of structures up to several microns in height.

The finite apex angle of tetrahedral tips limits the angular resolution of the imaging, that is vertical walls will always appear to have a finite slope. Since the tetrahedral tip has one vertical edge, it may be possible to position the cantilever in such a way as to image at least one wall of a trench with high fidelity. In order to evaluate the sidewall imaging ability of these tips a vertical-walled grating was imaged. This 6.25 μm period grating was fabricated by anisotropically etching a silicon (110) wafer. The grating's vertical sidewalls are defined by {111} crystal planes. From images of the vertical-walled grating, the smallest full angle of these tips we have inferred is 46° for both the front-to-back and side-to-side angles of the tip. In contrast, the full angle of the tip itself when viewed from the side is 34.8° and the full angle is 38.4° when viewed from directly in front of the tip, looking down the length of the cantilever. The difference between the angles inferred from imaging the silicon grating and the measured angles may be attributed to experimental error and large scale roughness of the tip's surfaces.
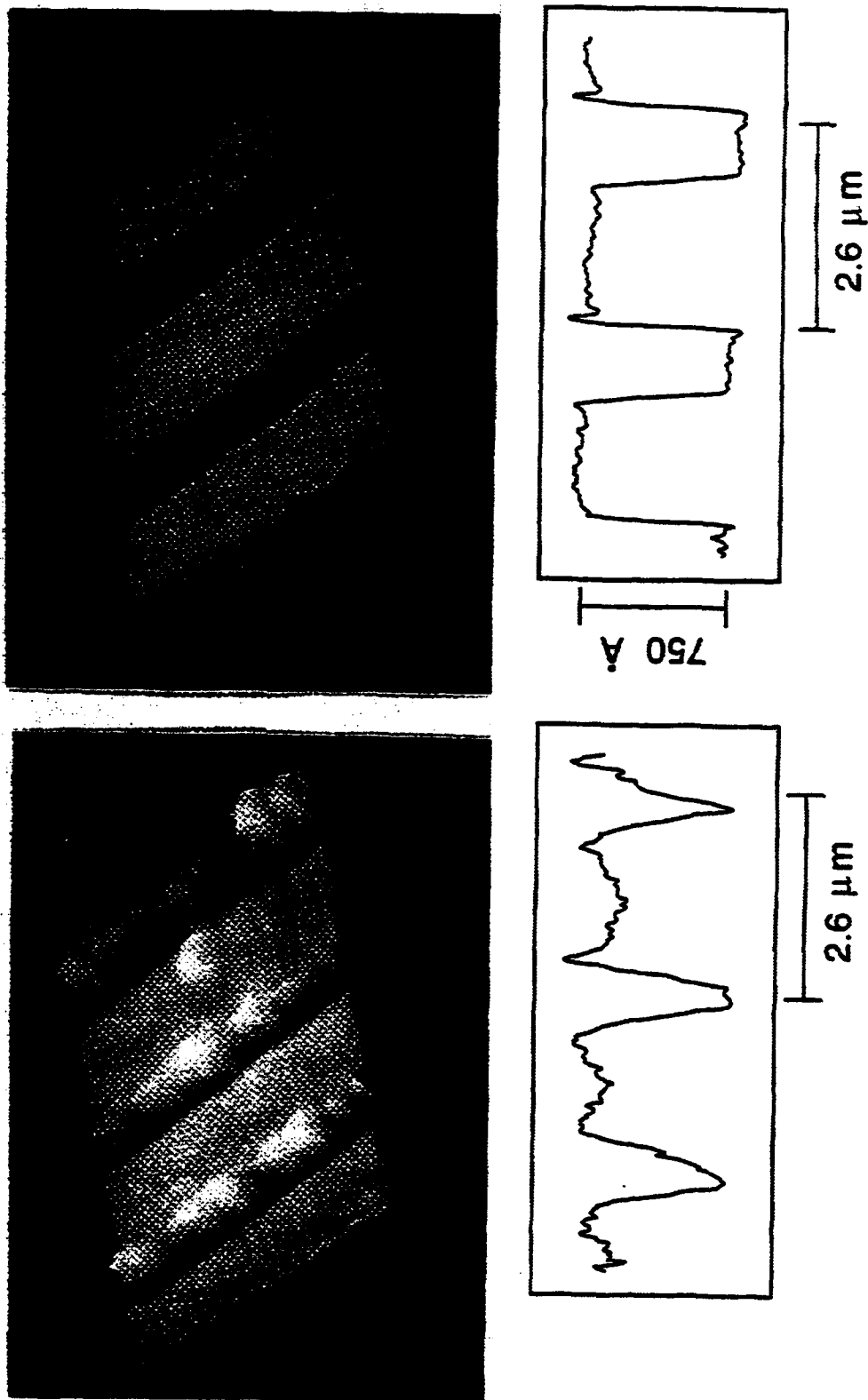
Figure 3.4 Using a cantilever with a fabricated tip improves the image quality of large structures as evidenced by the images and traces of a diffraction grating imaged with a flat cantilever (left) and a cantilever with a tetrahedral tip (right). These images were taken by Rob Barrett [8].

SEM micrographs of several tips before and after imaging clean graphite in air were compared to determine possible changes to the tip caused by imaging. SEM micrographs of the tips taken before use showed them to be sharp to the resolution limit of the SEM (approximately 200 Å). After using the cantilevers to image graphite for 30 minutes, the tips were examined again in the SEM and there was no perceivable change in the tip shape, even for those tips that had been accidentally crashed into the surface. On one occasion, while imaging the diffraction grating with a tipped cantilever, the image quality suddenly deteriorated. Examination of the tip in the SEM revealed that a contaminant particle approximately half the size of the tip had become attached to the tip. Cleaning the tip for 20 minutes in a 4:1 H_2SO_4/H_2O_2 solution removed the particle. The cantilever was rendered useless for optical detection AFM however, since the acid solution removed the reflective gold coating from the cantilever.

A CD stamper was imaged using a tetrahedral tip, a pyramidal tip and a flat cantilever with no fabricated tip (Figure 3.5). The spacing between tracks is 1.6 microns and the height of each bump is approximately 800 Å tall. The flat cantilever is clearly unable to follow the steep sidewalls of the CD bumps. Notice that each bump has a similar notch in the upper left. This feature is not on the sample but is rather a feature on the cantilever that is being "imaged" by the bump as the cantilever tracks over them. While the presence of either the tetrahedral or the pyramidal tip greatly enhances the image quality, there is a discernible difference between the images that these two tips produce. The edge transitions in the pyramidal tip image are less sharp than the those in the tetrahedral tip image. This effect is expected since the apex angle of the tetrahedral tip is roughly half that of the pyramidal tip.

Figure 3.5 A compact disk stamper was imaged using a tetrahedral tip, a pyramidal tip and a flat cantilever with no fabricated tip. The performance of the flat cantilever is the worst but there is a discernible difference even between the tetrahedral and pyramidal tip performances.

The difference between imaging with a pyramidal tip and a tetrahedral tip is further evidenced by the images of a gallium arsenide (GaAs) metal semiconductor field effect transistor (MESFET). The gate region of the MESFET is shown in Figure 3.6. The actual gate line which is 500 Å wide and approximately 200 Å tall is located at the bottom of a 5000 Å wide, 1800 Å deep trench. The tetrahedral tip is able to track the trench and detect the presence of the gate line whereas the pyramidal tip does not have an aspect ratio high enough to enter the trench completely and therefore does not sense the gate wire.

3.4   Summary

The silicon nitride cantilevers with tetrahedral silicon tips have several advantages over other types of cantilevers and tips. Tetrahedral tips are sharp, self-aligned and reproducible. In use, they are capable of faithfully following the contour of rough samples faithfully. The silicon tips are robust and show little or no wear from normal imaging of graphite.

Conical silicon tips, when oxidation sharpened, can have radii of curvature in the nanometer range, moreover they are radially symmetric. Process uniformity is still a problem for these ultra-sharp conical tips however. The tetrahedral tip may find an application with users who want sharper tips than pyramidal tips but do not want to pay the higher price of ultra-sharp, conical silicon tips.

Pyramidal Tip

Tetrahedral Tip

0.6 μm

Figure 3.6 These images of the gate region of a GaAs MESFET demonstrates the fact that image quality can differ even when using two cantilevers which both have tips. The tetrahedral tip (left) can reach into the bottom of the trench (5000 Å wide and 1800 Å deep) to image the gate line (500 Å wide and 200 Å tall) whereas the pyramidal tip (right) can not. These images were taken by Rob Barrett [8].
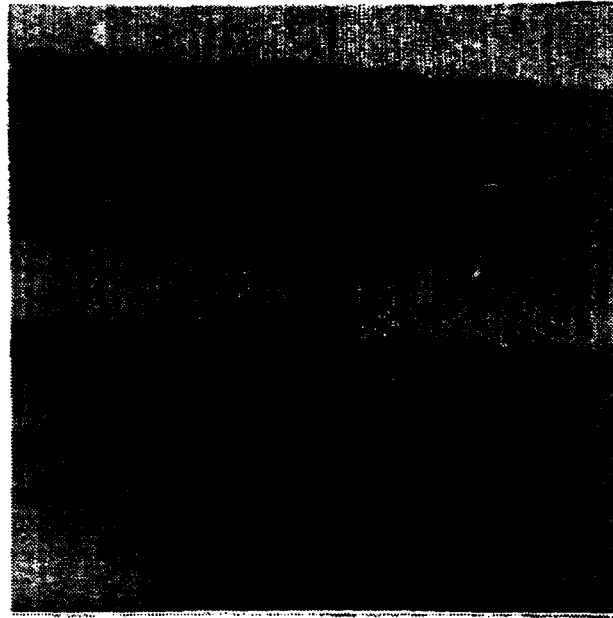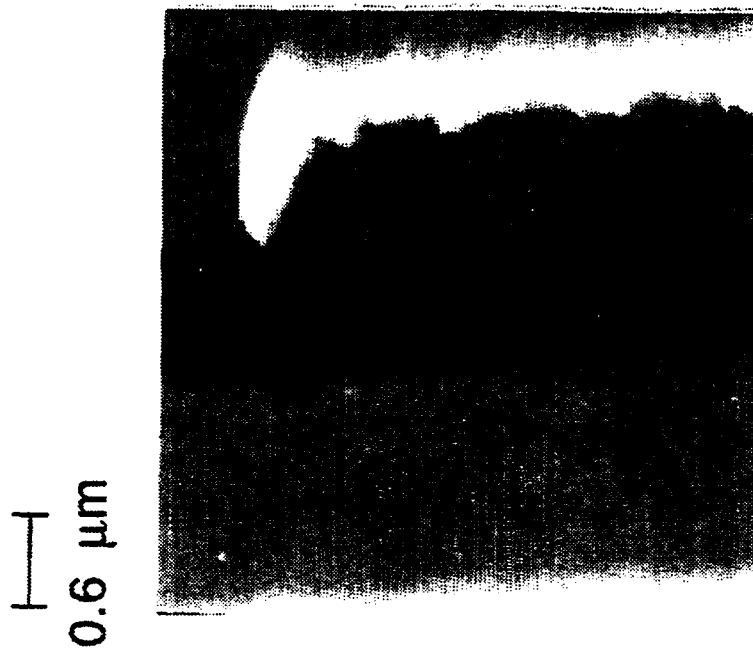
References

1)   T. R. Albrecht and C. F. Quate, J. Appl. Phys. **62**, 2599 (1987).

.2)   S. A. C. Gould, B. Drake, C. B. Prater, A. L. Weisenhorn, S. Manne, H. G. Hansma, P. K. Hansma, J. Massie, M. Longmire, V. Elings, B. Dixon Northern, B. Mukergee, C. M. Peterson, T. R. Albrecht and C. F. Quate, J. Vac. Sci. Technol. A 8, 369 (1990).

3)   M. M. Dovek, T. R. Albrecht, S. W. J. Kuan, C. A. Lang, R. Emch, P. Grütter, C. W. Frank, R. F. W. Pease, and C. F. Quate, J. Appl. Phys. **64**, 1178 (1988).

4)   B. Drake, C. B. Prater, A. L. Weisenhorn, S. A. C. Gould, T. R. Albrecht, C. F. Quate, D. S. Cannell, H. G. Hansma, and P. K. Hansma, Science **243**, 1586 (1989).

5)   G. Binning, C. F. Quate and Ch. Gerber, Phys. Rev. Lett. **56**, 1164 (1986).

6)   C. M. Mate, G. M. McClelland, R. Erlandsson, and S. Chiang, Phys. Rev. Lett. **59**, 1942 (1987).

7)   T. R. Albrecht, S. Akamine, T. E. Carver, and C. F. Quate, J. Vac. Sci. Technol. A 8, 3386 (1990).

8)   S. Akamine, R. C. Barrett, and C. F. Quate, Appl. Phys. Lett. **57**, 316 (1990).

9)   R. A. Buser, J. Brugger, and N. F. de Rooij, Microelectr. Engrg. 15, 407 (1991).

10)   O. Wolter, T. Bayer, and J. Greschner, J. Vac. Sci. Technol. 39, 1353 (1991).

11)   K. E. Peterson, Proc. IEEE **70**, 420 (1982).

12)   R. C. Barrett, Ph. D. dissertation, Stanford University (1991).

Chapter 4: Near-Field Scanning Acoustic Microscopy and Instrumentation

4.1 Introduction to Scanning Acoustic Microscopy

The scanning acoustic microscope was demonstrated by Lemons and Quate in 1973 [1]. The type of scanning acoustic microscope they invented uses an acoustic lens to focus sound waves in a fluid medium to a diffraction-limited spot. A sample is mechanically scanned through the focal spot. Variations in the acoustic properties of the sample alter the amplitude and phase of the reflected signal and these changes are the source of contrast. Lemons and Quate's instrument and its descendants [2, 3, 4] utilize piezoelectric elements to launch acoustic plane waves down a sapphire buffer rod to a hemispherical acoustic lens located at its end (Figure 4.1). The lens and sample are immersed in a liquid that acts as the transmission medium for the acoustic waves between the lens and the sample. Since the acoustic velocity in the buffer rod is significantly higher than in the liquid, it is possible to focus the acoustic waves to a diffraction limited spot of size given by [2]

$$S = (F\#)\lambda$$

$$\tag{4.1}$$

$$F\# = \frac{z_0}{D}$$

$$\tag{4.2}$$

where F# is the f-number of the lens, typically 0.75. z_0 is the focal length of the lens which can vary from 0.2 mm [1] to 12 μm [5]. D is the diameter of the lens aperture.
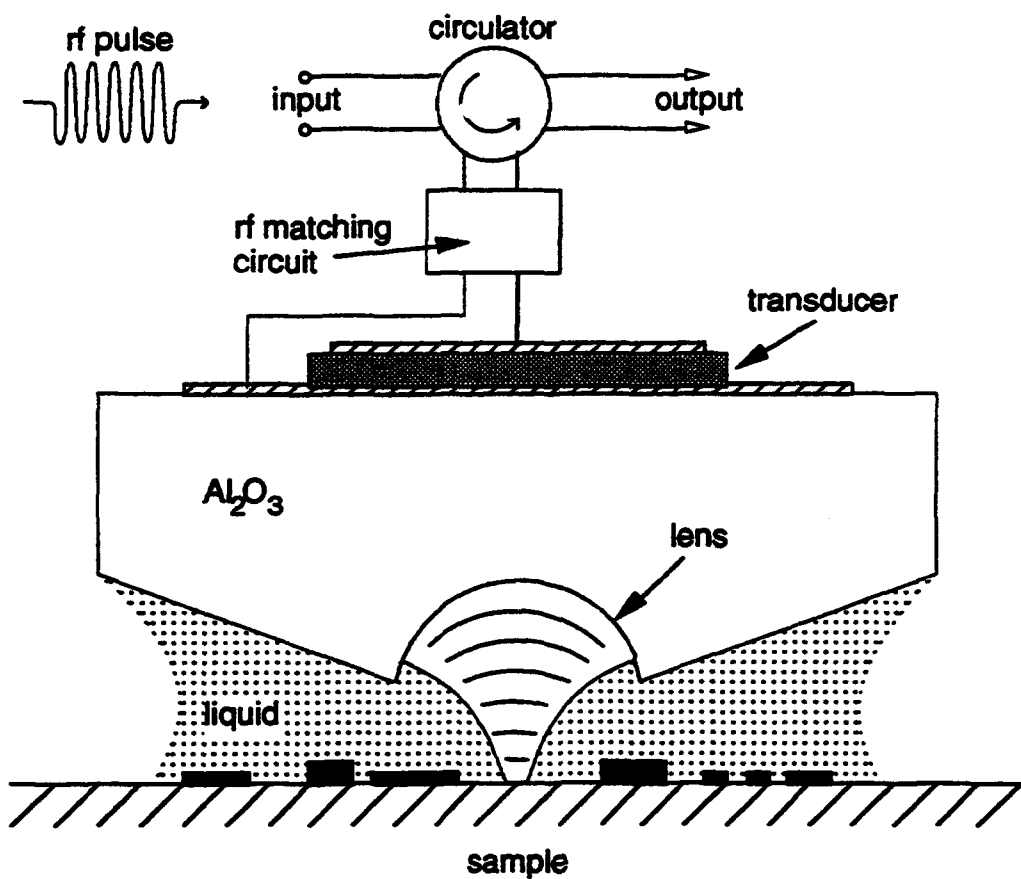
Figure 4.1 The far-field scanning acoustic microscope utilizes a hemispherical acoustic lens to focus acoustic waves in a liquid to a diffraction limited spot. (After Quate et al. [2].)

Since it is a far-field instrument, the resolution of the scanning acoustic microscope is limited by the spot size. In order to reduce the spot size the instrument can be operated at higher frequencies to reduce the acoustic wavelength; however, the frequency can not be increased without bound since the attenuation of sound in most liquids is proportional to the square of the frequency. Hence, if the frequency is increased, the acoustic path length must be reduced by a corresponding factor in order to maintain acoustic signal power

constant. Reducing the acoustic path length becomes a practical problem since it can be difficult to fabricate lenses with focal lengths on the order of a few microns. The far-field scanning acoustic microscope can have resolution as high as 2000 Å when operated in water at an acoustic frequency of 5 GHz. In liquid helium at a temperature of 0.2 K, the resolution can be as high as 200 Å [3].

The advantages of the scanning acoustic microscope is not limited to its high resolution however. It is an important analytical tool because it provides images based on a different contrast mechanism than other forms of microscopy. The contrast mechanism in acoustic microscopy relies on variations in the acoustic properties at various locations of a sample. It is therefore possible to see details in acoustic images which are not detectable in the optical microscope [6] A further distinction between the scanning acoustic microscope and the scanning electron microscope (SEM) is that the scanning acoustic microscope images samples under liquid which can be an advantage when imaging certain samples such as living cells which can not be imaged in vacuum.

Imaging samples under liquid, although advantageous in some instances, can also be disadvantageous in others since some samples are not compatible with liquids, this represents a limitation on the use of the acoustic microscope. Although some low resolution images have been obtained using air as the acoustic medium [7], in general it is necessary to immerse the sample in a liquid. Another drawback to scanning acoustic microscopy is that in order to resolve features of less than a micron, it is often necessary to immerse the sample in either hot water or in cryogenic gases. These operating conditions are problematic not only because they are incompatible with some samples, but also because they make it more difficult to inspect samples quickly.

4.2   Near-field Scanning Acoustic Microscopy (NSAM)

The first microscope utilizing the near-field effect was demonstrated by Ash Nichols in 1972 [8]. Their instrument passed 10 GHz rf waves through a 1.5 mm aperture and achieved a lateral resolution of 0.5 mm, or $\lambda/60$. The growth in importance of the STM, AFM and other scanning probe instruments in the 1980's kindled a renewed interest in the near-field acoustic microscopy [9, 10, 11, 12, 13, 14].

In near-field scanning acoustic microscopy (NSAM), much as in the STM and AFM, a sharp probe is brought into close proximity to a sample such that acoustic energy can be coupled between the two. In contrast to previous scanning acoustic microscopes in which the acoustic spot is created by focusing sound waves with lenses or by passing acoustic waves through a small aperture, in the near-field scanning acoustic microscopes the acoustic spot is made small by using a solid tip with a very sharp apex. The extremity of the tip is typically 10 to 10,000 times smaller than the wavelength of the acoustic waves that it transmits. Hence, the resolution of the microscope is limited not by the diameter of a diffraction-limited spot but rather by the radius of curvature of the tip and the acoustic power that can be delivered to the apex of the tip.

A second limitation on the resolution of scanning acoustic microscopes is the working distance between the tip and the sample. In order to obtain the optimum resolution, the tip must not only be sharp, but its position must also be maintained within a fraction of a wavelength from the sample surface. The resolution is therefore determined by the larger of the spacing between the tip and sample or the radius of curvature of the tip.

4.2.1 Resonance NSAM

There are two major types of NSAM instruments. The first type, exemplified by acoustic microscope of Güthner and coworkers, utilizes some form of an acoustic resonator (Figure 4.2) [11]. In this case, one arm of a quartz tuning fork acts as a probe. The tuning fork is driven at its resonance frequency of 32.7 KHz and the interaction of the tuning fork with the sample is monitored by measuring changes in the resonance frequency or vibration amplitude of the tuning fork. This configuration has yielded images of insulators with lateral resolution on the order of 1 μm.
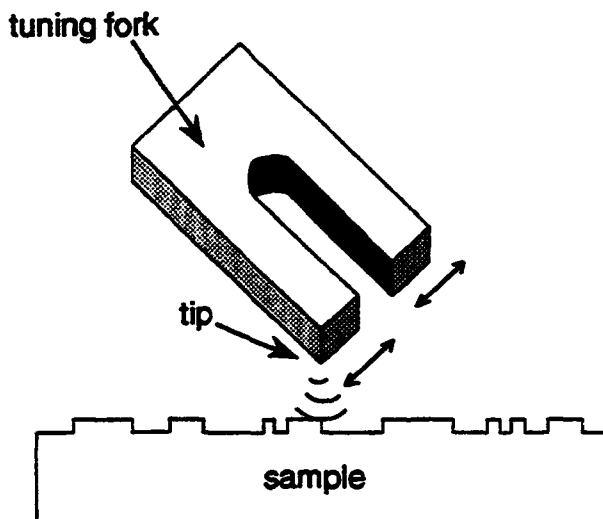
Figure 4.2 Güthner and coworkers use one leg of a quartz oscillator as a tip to probe a sample acoustically. The image is obtained by monitoring the amplitude of the oscillator's vibration.

Among several benefits of the resonator-type instrument is that when forces between the sample and the tip are sufficiently large, the vibration of the resonator stops.

This effect provides a convenient measure of the point where the separation between tip and sample is zero.

A further advantage of the resonator-type acoustic microscope is that it is a single port device that operates without a receiving transducer on the back of the sample. Such instruments are easier to use since they require no alignment of transmitting and receiving transducers and they are also capable of imaging samples of any reasonable thickness.

In order for the resonator-type instrument to function properly however, either the resonator must have very high Q so that small changes in the applied force create significant variations in the resonance frequency or the microscope must be able to determine the vibration amplitude very accurately.

4.2.2 Transmission NSAM

Other versions of NSAMs do not use acoustic resonators, but instead operate in transmission mode in which sound waves are excited in the tip by one ultrasonic transducer and transmitted into the sample where they are received by a second transducer. Takata and coworkers [9] demonstrated such a transmission instrument that vibrates a tip approximately 10 $Å_{p-p}$ by applying a continuous wave 70 KHz sinusoidal voltage to the z electrode of a piezoelectric scanner tube (Figure 4.3). The received acoustic signal is rectified and can be used to control the spacing between the tip and the sample through the use of a feed back circuit.

While imaging in the transmission acoustic mode, Takata's instrument can also monitor tunneling currents between the tip and the sample so that for conductive samples, two different contrast mechanisms can be monitored and the separation between the tip and the sample can, in principle, be controlled by either signal.
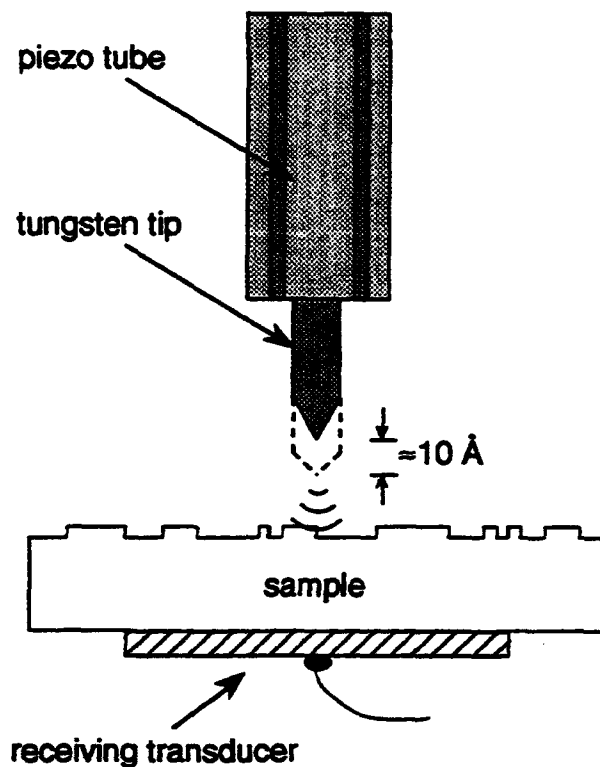
Figure 4.3 Transmission mode NSAM has been demonstrated by several
researchers using modified STMs. Takata and coworkers modulate the z
piezo of a standard STM scanner to excite acoustic waves into the sample.

Advantages of two-port NSAM instruments include the fact that since the tip need

not be an integral part of an acoustically resonator, common tungsten or platinum/iridium

tips similar to those used in STMs can be used. If the tip is damaged during use, it can be

replaced easily and quickly. Damage to the tip is of particular concern for non-resonator-

type instruments since there is no inherent sign, in the absence of a tunneling current

signal, when the tip and sample come into contact.

In the resonator-type instruments, when the tip and sample come into contact, the

resonator stops resonating. In transmission instruments however, if the tip were to make

contact with the sample, the transmitted acoustic signal could still show a distance dependence since raising or lowering the tip could change the cross-sectional area of contact between the tip and the sample and thereby modulate the transmitted signal.

The frequency range of operation for a NSAM using a piezoelectric tube scanner as its ultrasonic source is determined by the resonance frequency of the piezoelectric tube. Typical PZT piezoelectric tube scanners have resonances on the order of tens to hundreds of kHz. In lieu of the tube scanner, piezoelectric plates can be bonded on the end of metal tips [10] but at frequencies in the range of several MHz and above, poor bond quality between the piezoelectric transducer and the base of the tip causes coupling inefficiencies which limit the transmission of acoustic power from the transducer to the tip.

4.3 NSAM With Microfabricated Probe Assembly

Unlike other NSAMs the instrument presented in this dissertation uses integrated, microfabricated tips and transducers instead of sharpened wires, piezoelectric ceramics and crystal resonators. Microfabrication techniques allow the fabrication of hundreds of tips and transducers on each silicon wafer. In addition, as described in Chapter 2, the technology for microfabricating sharp tips has improved to a level such that it is possible to microfabricate silicon tips that are sharper than sharpened metal tips. Utilizing ZnO thin films for transducers instead of bulk piezoelectric ceramics such as PZT, it is possible to obtain efficient, high frequency transducers with excellent acoustic coupling between the transducer and the tip even at frequencies in the GHz regime. The following sections describe the fabrication of the tip and ultrasonic transducer assembly as well as the mechanical design of the instrument.

4.4   Tip Fabrication Process

The NSAM tips are fabricated using either the conical or the tetrahedral tip fabrication processes described in Chapter 2. Since the tips for use in NSAM are not mounted on the ends of cantilevers but are instead located in the center of a square silicon die, the tips must be quite tall to allow some tilt of the sample with respect to the tip substrate without causing the edge of the die to touch the sample (Figure 4.4). Tips of 60 to 100 μm height were fabricated allowing a 2 degree tilt.
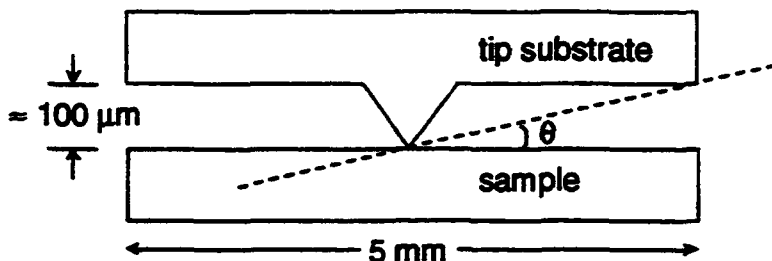
Figure 4.4 The NSAM tips must be tall so that the allowable tilt angle of the tip substrate with respect to the sample is as large as possible.

Making such tall tips necessitates some modifications to the tip fabrication processes previously described. In both the conical and the tetrahedral tip fabrication processes the height of the tips is determined by a SF_6/C_2ClF_5 plasma etch. To fabricate tips of height up to 10 μm, silicon dioxide, silicon nitride or even photoresist can be used as a masking material. When the tips exceed this height however, the etch selectivity between the silicon and the masking materials in the plasma is insufficient to allow extended etching. For tall tips therefore, aluminum, chrome, tungsten or some other refractory metal must be used as the masking material since the etch rate of these materials in the silicon plasma etch is insignificant.

To fabricate tall NSAM tips, 1000 Å of evaporated aluminum was chosen for a masking layer due to aluminum's ease of deposition, relatively low stress and compatibility with other standard integrated circuit fabrication processes.
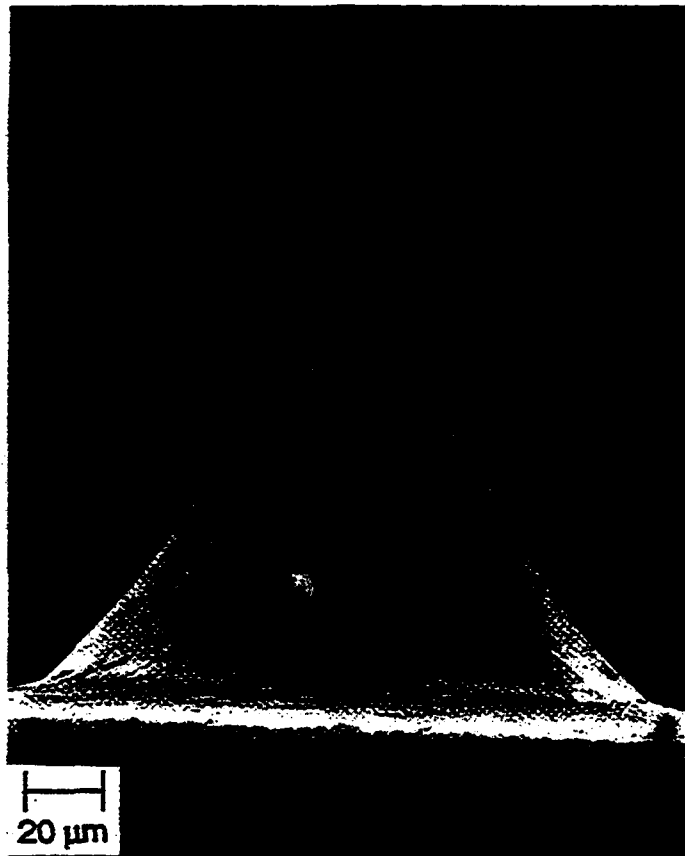
Figure 4.5 The completed conical tip shown here is approximately 100 μm tall.

The inclusion of a metal masking layer creates a process compatibility problem since metal contaminants can diffuse out of a wafer during subsequent high temperature thermal cycles. For both the conical and the tetrahedral tip processes, the only high temperature process step necessary after the long dry etch is a thermal oxidation at 950 °C. These oxidations are carried out in a metal contaminated oxidation furnace typically used

for tungsten annealing so contamination from the metal masking materials used during the long dry etch process does not adversely affect clean furnaces reserved for electronic device fabrication.

Although both conical and tetrahedral tip processes yield sharp tips, it is more difficult to make a tall tetrahedral tip than it is to make a conical tip of similar height. In order to fabricate a tetrahedral tip, a vertical-walled post must first be formed. When the desired tip height is on the order of 100 μm, it is difficult to make a sufficiently tall vertical-walled post. For this reason, conical tips are preferred for use in NSAM.

One modification included in the next generation of tips being fabricated by Andreas Judas is the creation of relatively short conical tips of 1 to 10 μm height on silicon mesas which are approximately 100 μm tall (Figure 4.6). The fabrication process for such tips begins with the oxidation of a double side polished, silicon (100) wafer. Small oxide circles approximately 10 μm in diameter are patterned and etched. Silicon nitride is then deposited over the entire wafer and large nitride squares on the order of 100 μm on a side are patterned and etched. The mesas are formed by using the silicon nitride as a mask while wet etching the silicon in EDP or KOH. After mesas of a desired height have been obtained, the nitride is stripped to expose the silicon dioxide circles. The circles are used as masks during either a plasma or wet etch in EDP during which the silicon is etched until the circles are almost completely undercut. The circles are then removed by etching in a buffered HF solution.

☐ silicon
■ oxide
☑ nitride

a)

b)

c)

d) ≈ 10 μm
   ≈ 100 μm
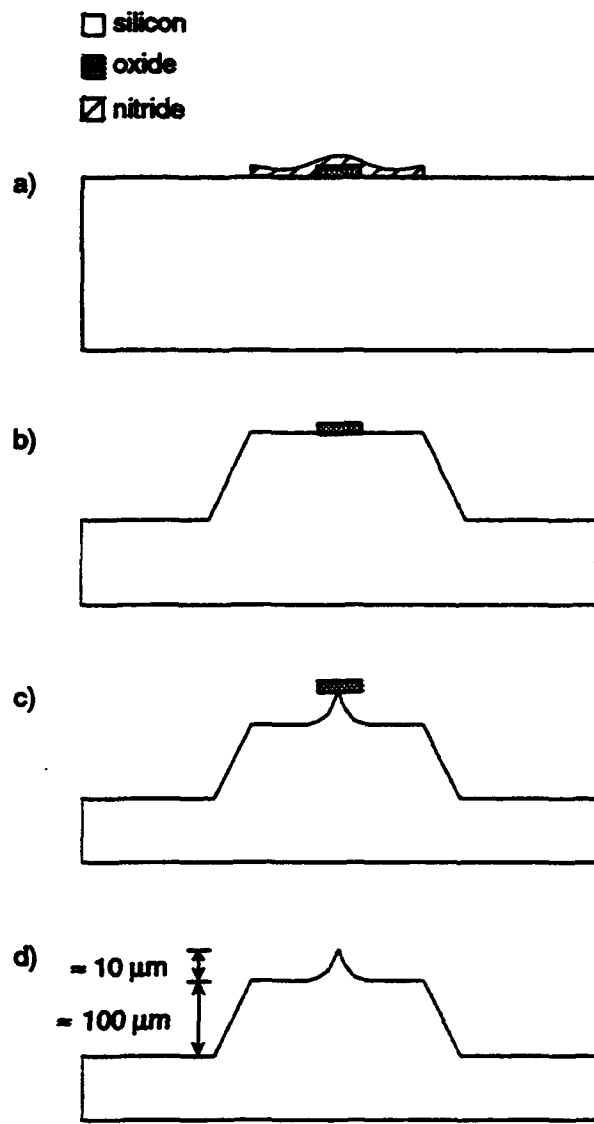
Figure 4.6 To make a tip on a mesa structure, a) a double layer mask of nitride over oxide is patterned. b) An anisotropic wet etch is first used to form a mesa c) and a short plasma etch is then used to form the small conical tip. d) The final tip is exposed when the oxide mask is selectively removed.

If further sharpening is desired, the tips are thermally oxidized in steam at 950 °C. Due to the differential oxide growth rate on tips previously described in Chapter 2, the silicon tip is sharpened by the oxidation and subsequent removal of the oxide.

The mesa tip process has two principal advantages over the previous conical tip process. First, since the mesas are wet etched using nitride as the mask, no metal masking layer is necessary and process compatibility problems are alleviated. An additional benefit of the process is that since most if not all of the silicon etching is done with wet etchants, uniformity from tip to tip is increased and the use of environmentally harmful chloroflourocarbons for plasma etching can be reduced.

4.5 Ultrasonic Transducer Fabrication Process

Other than the fabrication of the tips the other major fabrication process necessary is for creation of the ultrasonic transducers. The ultrasonic transducers are simple, capacitor-like structures consisting of a ZnO island sandwiched between a gold ground plane electrode and a small gold top electrode (Figure 4.7).

Before the fabrication of the ultrasonic transducers can begin, if the devices are to be made on a silicon substrate, the silicon wafer must first be oxidized or covered with silicon nitride in order to allow the subsequent deposition of well-oriented ZnO. In these cases, a 1000 Å thick film of silicon nitride is used. When the substrate has been properly prepared, 1000 Å of gold are evaporated on the wafer using a 40 to 100 Å thick titanium adhesion promotion layer. When the wafer is unloaded from the gold evaporation station it is immediately placed in the ZnO sputtering station [15] where a $\lambda/2$ thick film of ZnO is deposited. A 1000 Å thick, gold top electrode is then evaporated and patterned using a

69

lift-off process. Finally, the ZnO is patterned and etched from all areas except in islands under and around the top electrodes.
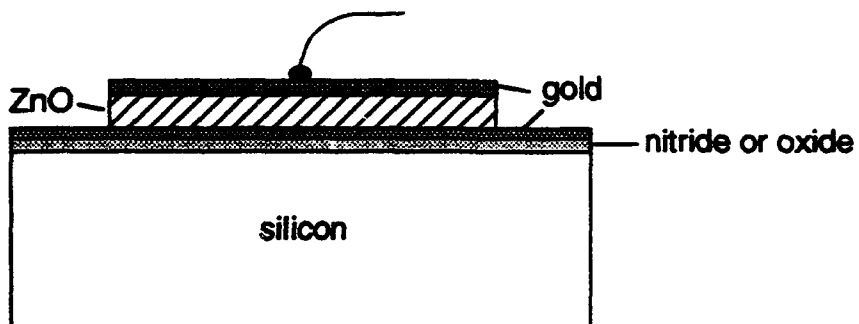
Figure 4.7 The ultrasonic transducers are similar in structure to capacitors. They are comprised of 2 gold electrodes each 1000 Å thick on either side of a ZnO layer. A 1000 Å film of oxide or nitride on the silicon facilitates the growth of c-axis oriented ZnO. The thickness of the ZnO is chosen to be equal to half the desired acoustic wavelength. Diameter of the transducers is 100 to 200 μm.

Patterning the ZnO serves two purposes, first it exposes the ground plane for making electrical contact and secondly, it removes most of the highly stressed ZnO film which is prone to peeling after long exposures to humidity.

4.5.2 Ultrasonic Transducer Design

When designing the transducers, there are two principal variables that can be altered, the thickness of the piezoelectric material and the area, or size, of the transducer. The thickness of the piezoelectric material is determined by the desired operating frequency. Once chosen, the operating frequency in conjunction with the acoustic velocity in the piezoelectric material determines the wavelength of the acoustic wave. For a first order design, if the transducer is considered to be air-backed, the thickness mode resonance of

70

the device can be excited if the thickness of the piezoelectric film is equal 1/2 the acoustic wavelength in the piezoelectric material. The longitudinal acoustic velocity in ZnO is 6.33 km/s [16] and the corresponding wavelength at 1 GHz is 6.33 μm. Therefore, for 1 GHz operation approximately 3.16 μm of ZnO are deposited.

The assumption that the transducer is air-backed is a good one in reality since the 1000 Å gold top electrode and the gold bonding ball represent only a small amount of mass loading. For the purposes of the NSAM, the small deviation between the theoretical and actual operating frequencies is negligible since the transducers' operation is sufficiently broad band to allow a matching network to tune the transducers within in an acceptable frequency range.

The size of the transducer is primarily influenced by the need to generate plane waves with uniform acoustic intensity. The acoustic field intensity generated by an ultrasonic transducer varies widely depending on the distance from the transducer along the axis and the distance from the axis. It is convenient to consider two distinct regions defined by the Fresnel limit, S = 1, where S, for an isotropic substrate, is the Fresnel parameter given by [16]

$$S = \frac{z\lambda}{a^2}$$

(4.1)

z is the distance from the transducer measured along the axis, λ is the wavelength of the acoustic wave, and a is the transducer radius.

The region where S < 1 is known as the Fresnel region. In the Fresnel region, the acoustic intensity varies rapidly with z but is uniform and well-confined within an area roughly corresponding to the transducer cross-section. The Fraunhofer region where S > 1, is the region in which diffraction becomes significant and the acoustic intensity falls

monotonically as $1/z^2$ along the axis. Due to diffraction the intensity also falls off in directions orthogonal to the axis such that at the plane $S = 1$, the main lobe has its -3 dB points at a radius of 0.35 a.

Given that acoustic intensity is such a strong function of radius and distance, the transducer was designed to operate in the regime between $S = 1$ and $S = 2$ to deliver the highest and most uniform field intensity possible to the base of the silicon tip. If the tip were too far in the Fresnel zone of the transducer, the field intensities across is base would not be uniform. If in contrast, the tip was too far in the Fraunhofer region, the field intensity would be less than the maximum value possible. For these probes, transducers of various sizes were fabricated. For 1 GHz operation on 1 mm thick silicon wafers these transducer sizes correspond to $0.025 < S < 47.8$. Since the last minimum of the field intensity occurs at $S = 1$, transducers were designed to operate between $S = 1$ and $S = 2$ in order to maximize efficiency. It was determined empirically that transducers ranging in radius from 28.79 to 57.57 μm, or S parameter from 7.6 to 1.9 work best in the NSAM.

Transducer Area (μm^2)	Equivalent Radius (μm^2)	S parameter
416	11.5	47.8
2603	28.79	7.6
10,411	57.57	1.9
41,642	115.13	0.48
125,434	199.82	0.16
260,265	287.83	0.076
384,141	349.68	0.052
783,961	499.54	0.025

Table 4.1 Transducer areas and calculated S parameters are shown in this table. Equivalent radii are indicated since transducers were not circular in all cases.

4.5.2 Ultrasonic Transducer Performance

The transducers are designed to have a thickness resonance mode at a given operating frequency. In order to operate efficiently the impedance of the transducer must be well-matched to the impedance of the driving electronics which is commonly 50 Ω. Figure 4.8 (a) and (b) show the reflection coefficient, or $|S_{11}|$, of a 50 μm transducer with and without a matching network.
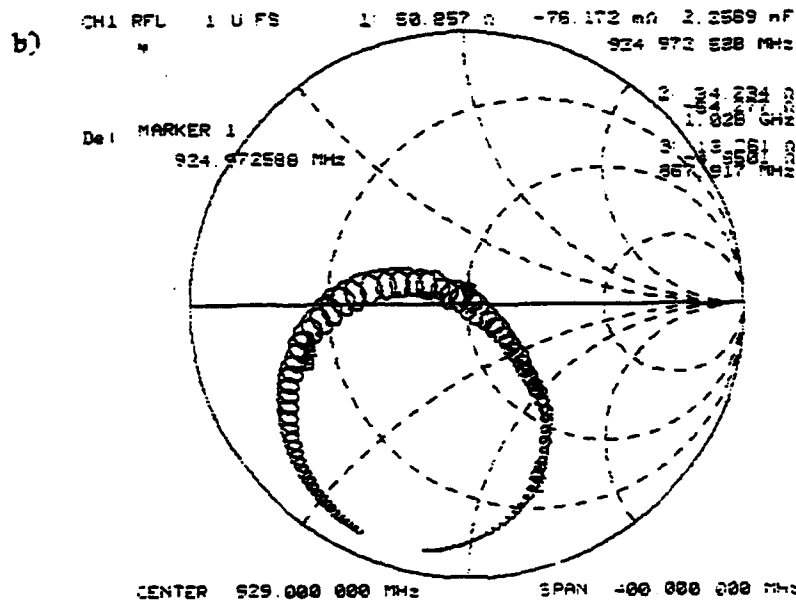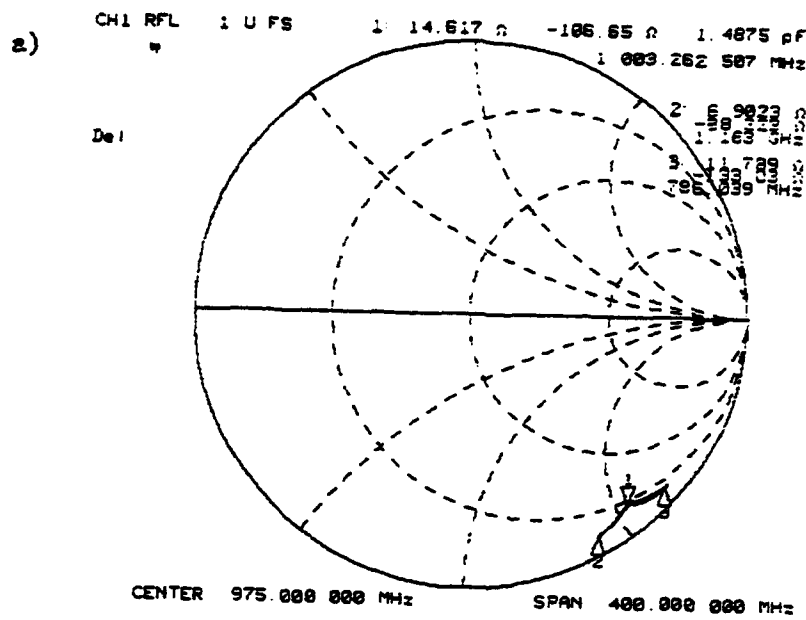
Figure 4.8 a) The plot of $|S_{11}|$ for an untuned transducer shows a very
poor match to the 50 Ω. b) When the transducer is tuned with using a
matching network, the $|S_{11}|$ curve passes directly through the 50 Ω point
at the center of the Smith chart.
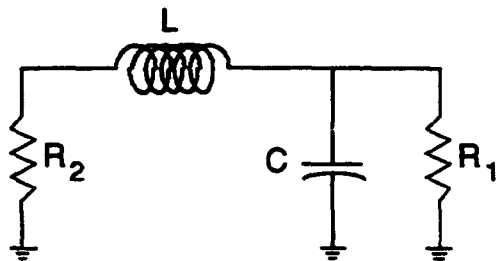
$$R_2 > R_1$$

$$X_L = Q R_1$$

$$X_C = \frac{R_2}{Q}$$

$$Q = \sqrt{\frac{R_2}{R_1} - 1}$$

Figure 4.9 The matching networks used to tune the transducers were made using these circuits and design rules after Hardy [17].

The rules used to design the matching network are shown in Figure 4.9 [17]. The Smith chart in Figure 4.8 (a) shows only a small resonance peak that is poorly matched to the 50 Ω impedance at the center of the chart while the reflection coefficient of the same transducer with the matching network passes directly through the 50 Ω point.

Matching networks are used in this manner to match impedances and tune the operating frequencies of the transducers used in most of the experiments described in this dissertation. The one-way insertion loss versus frequency of a tuned transducer on a silicon wafer is shown in Figure 4.10.
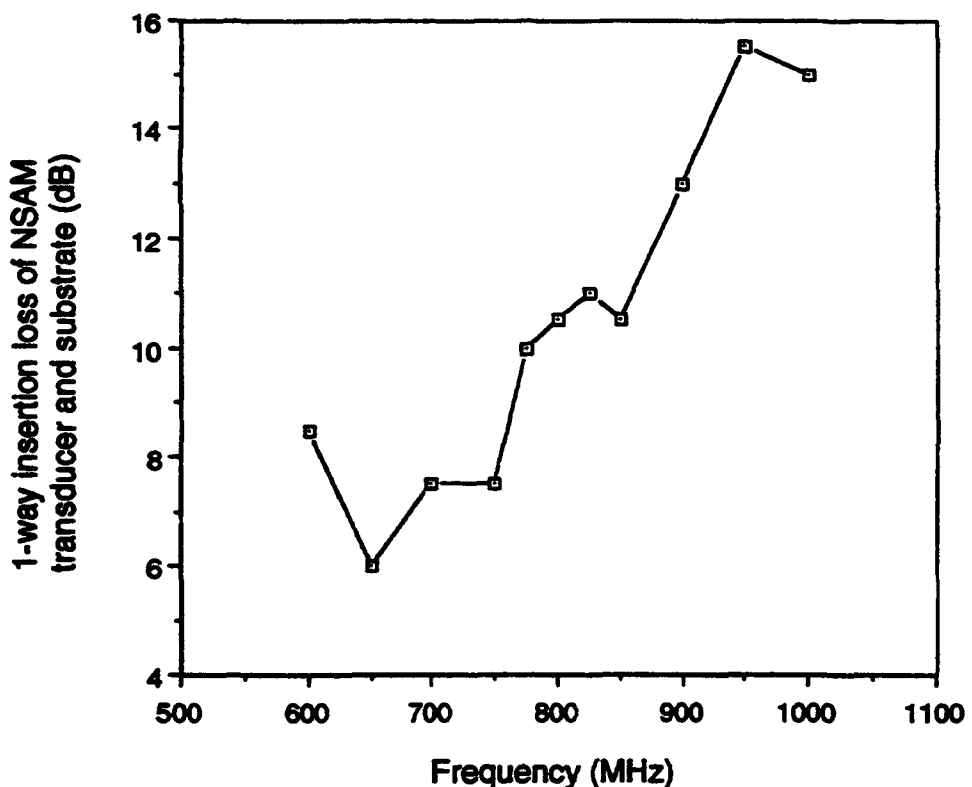
Figure 4.10 A tuned transducer operates in a fairly broad band and can
have insertion loss as low as 3 dB. The minimum insertion loss for this
transducer is 6 dB.

4.6 Hybrid Probe Assembly Process

The processes described above for fabricating the tips and the ultrasonic transducers

can be carried out on single or separate substrates. Initially, in order to study the feasibility

of the project, a hybrid process was used in which the transducer is fabricated on a Pyrex

7740 glass substrate and the tip is fabricated on a separate silicon substrate (Figure 4.11).

Although in principle, the entire tip wafer could be anodically bonded to the entire

transducer substrate, in this initial stage of experimentation, the tip and transducer masks

76

were not designed specifically for this project and therefore the tips and transducers were not aligned to each other across the entire wafer. For expediency, the substrates were each diced and individual tip dice were bonded to individual transducer dice.
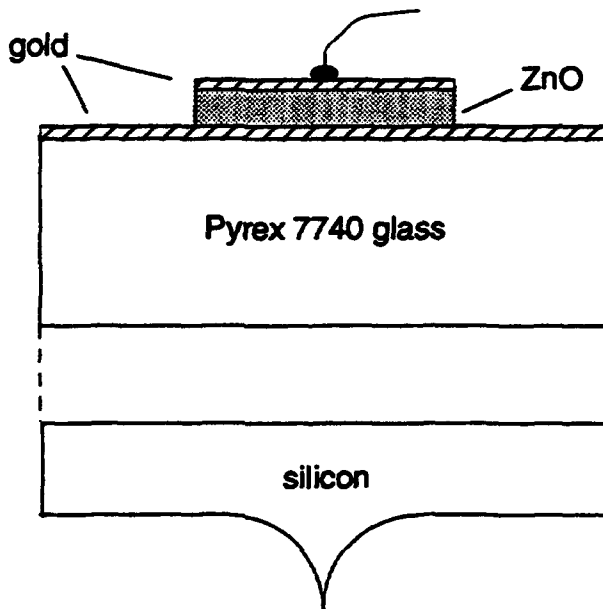
Figure 4.11 In the hybrid process, the tip is fabricated on a silicon wafer while the acoustic transducer is fabricated on a 7740 Pyrex glass substrate. To form the probe, the tip and transducer substrates are anodically bonded together.

The bonding of the tip and transducer substrates was accomplished using a low temperature anodic bonding process [18]. To begin the process, the die with the tip is placed in a special jig that holds the die with the tip facing downward into a cavity. The Pyrex die with the transducer is placed on top of the tip die and aligned under a direct view optical aligner which has coaxial optical objectives to view both sides of the sample. The alignment is accomplished by hand using tweezers to adjust the position of the dice. Approximately 25 µm accuracy in alignment is achievable using this technique. When the

alignment is completed, the entire jig assembly is transported to a hot plate. The silicon substrate is grounded and a large negative voltage is applied to the Pyrex through a point contact. Since the Pyrex is transparent, the bonding front can be observed moving across the entire 1 cm^2 die in a few minutes. To ensure proper bonding however, the voltage and temperature are maintained for 30 minutes. After bonding, the device is placed in the aligner again to confirm that the tip and transducer have in fact been bonded in alignment. Lastly, a 1 mil thick gold wire is bonded to the top electrode of the transducer to complete the hybrid fabrication process.

The principal advantage of the hybrid fabrication process is that the tip and the transducer are fabricated independently thereby reducing problems of process compatibility. For example, tip fabrication processes typically include the use of chemicals such as KOH or EDP, both of which would rapidly attack the ZnO in the transducers and therefore preclude the fabrication of transducers before tips. Fabricating tips before transducers is also difficult because it necessitates the protection of the sharp and fragile tips during all transducer fabrication steps. By fabricating the tips on silicon wafers in the absence of the transducers, the entire fabrication process is greatly simplified.

The acoustic reflection coefficient, Γ, of the silicon/Pyrex interface is given by [16]

$$\Gamma = \frac{Z_2 - Z_1}{Z_2 + Z_1}$$

(4.2)

where the acoustic impedances of Pyrex, Z_1, and silicon (100), Z_2, are 13.1×10^6 kg/m^2s and 19.7×10^6 kg/m^2s respectively [19]. The silicon/Pyrex interface therefore has an acoustic reflection coefficient of 0.201. The power transmission coefficient is expressed as [16]

$$\mathcal{T}_p = 1 - |\Gamma|^2$$

(4.3)

78

so for the silicon/Pyrex interface the power transmission coefficient is 0.960 or only -0.358 dB. Thus the silicon/Pyrex bond is relatively lossless.

4.7 Integrated Probe Assembly Process

After the hybrid process was used to demonstrate the viability of the NSAM, a complete mask set was designed to fabricate an integrated probe assembly. The most important difference between the hybrid process and the integrated process is that in the integrated process the tip and transducer are fabricated on the same substrate and the need for anodic bonding is eliminated.

To begin the integrated probe fabrication process, alignment marks are patterned on both sides of a 1 mm thick, double-side polished (100) silicon wafer which has previously been coated with thermal silicon oxide or LPCVD silicon nitride. The alignment is done using a Kasper 2001 contact aligner with an infrared transmission alignment capability. Tips are then fabricated and oxidation sharpened on one side of the wafer. Once the tips have been formed, all subsequent process steps are conducted using spacers to prevent the wafer from being placed face down on the tips. In some pieces of equipment, special stages are used which hold the wafer with the tips facing down over a depression suspended only at the wafer's perimeter. Keeping the tips protected at all times, the ultrasonic transducers are fabricated on the back side of the wafer using the fabrication process described above. The wafer is then cleaved into the individuals dice and gold leads are bonded.

4.8 Tip and Sample Mounting

To use the microfabricated probes in the NSAM, they must be mounted in a housing which provides rf shielding and can contain the rf matching network. Maximum rf shielding is desirable to prevent direct rf feed-through which results in high coherent background signal levels. The size and mass of the housing must be kept at a minimum so that the mass of the probe assembly will not load the piezoelectric tube scanner. Finally, the housing must accommodate the rf matching network circuitry which typically consists of a total of two or three chip capacitors and inductors. A photograph of a transducer housing is shown in Figure 4.12
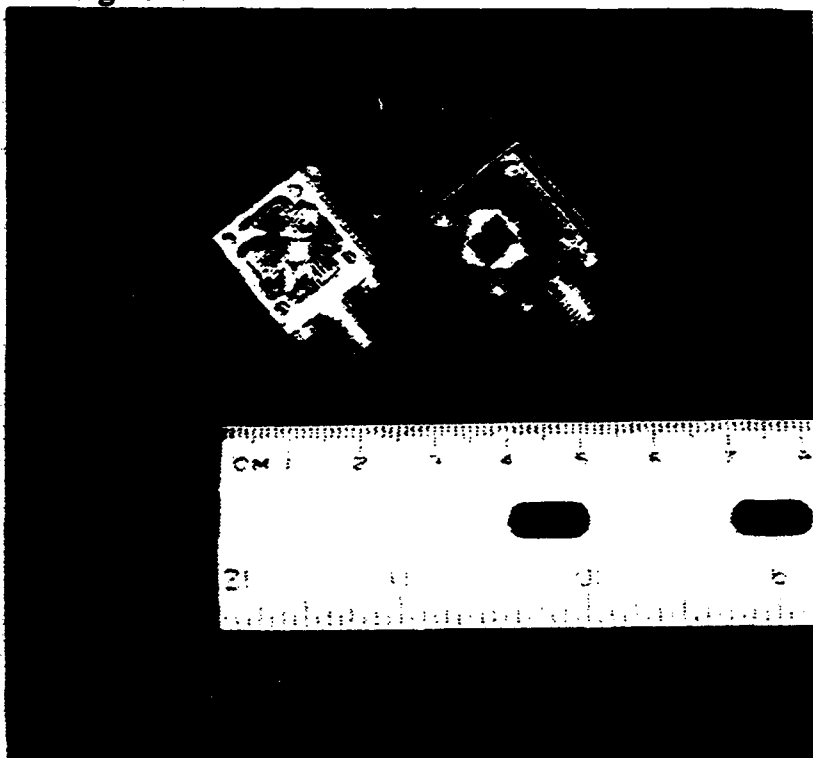

Figure 4.12 The housing for the transducers and matching networks must be small to prevent mass loading of the piezoelectric tube scanners and they

must be effective in shielding rf radiation. They are made from brass and measure 5/8" on a side.

4.9 NSAM Mechanical Instrumentation

The near-field acoustic microscope described in this work is shown in [Figure 4.13]. The mechanical instrumentation is based on the tripod design [20] and is largely identical to that of an STM. The three 1/4-80 screws form an equilateral triangle with height of 2 inches. These screws are used to adjust the tip height and tilt relative to the sample. The piezoelectric tube scanner is placed 0.3 inches from the base on the perpendicular bisector of the triangle formed by the screws. Therefore, when the height of the rear screw is adjusted, the tip rises with respect to the sample by an amount reduced by a factor of 0.3/1.7 or 0.18. This lever arm reduction enables the rear screw to have finer control of the height than the two screws at the front. The head of the microscope was constructed using the translation stage from a Park Scientific Instruments AFM [21].

The translation stage is necessary for positioning the tip precisely with respect to the receiving transducer on the back of the sample. In transmission mode this alignment must be accurate to within 25 µm. The disadvantage of the translation stage is that it may compromise the stiffness of the microscope and thereby increase drift or reduce the frequency of its lowest mechanical resonance. In fact, the same stage has been used in the Park Scientific Instruments' AFM and STM to obtain atomic resolution images successfully so it does not appear to be a limiting factor in this instrument.
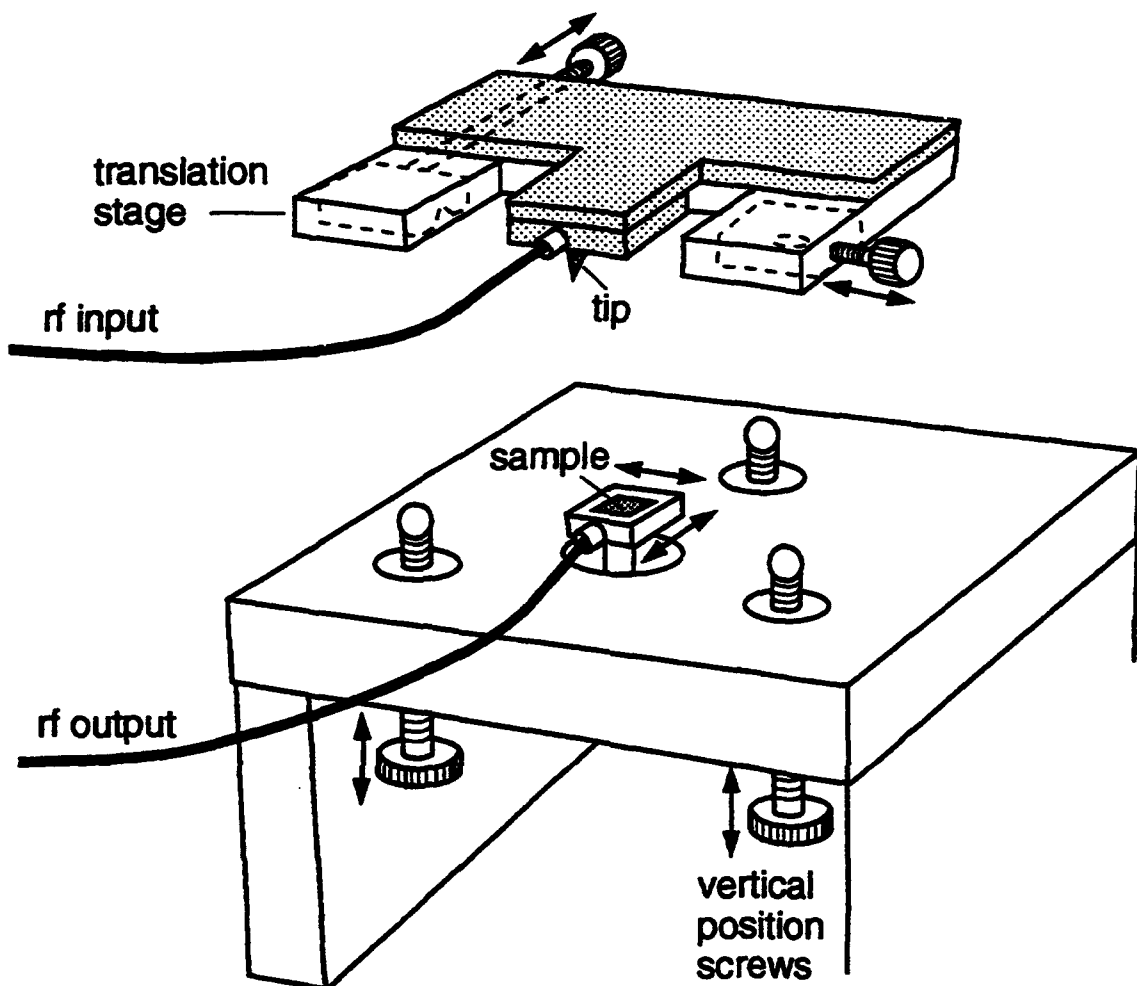
Figure 4.13 The mechanical instrumentation of the NSAM is almost identical to that of a STM with the exception of the translation stage that is necessary in NSAM to align the tip to the sample transducer.
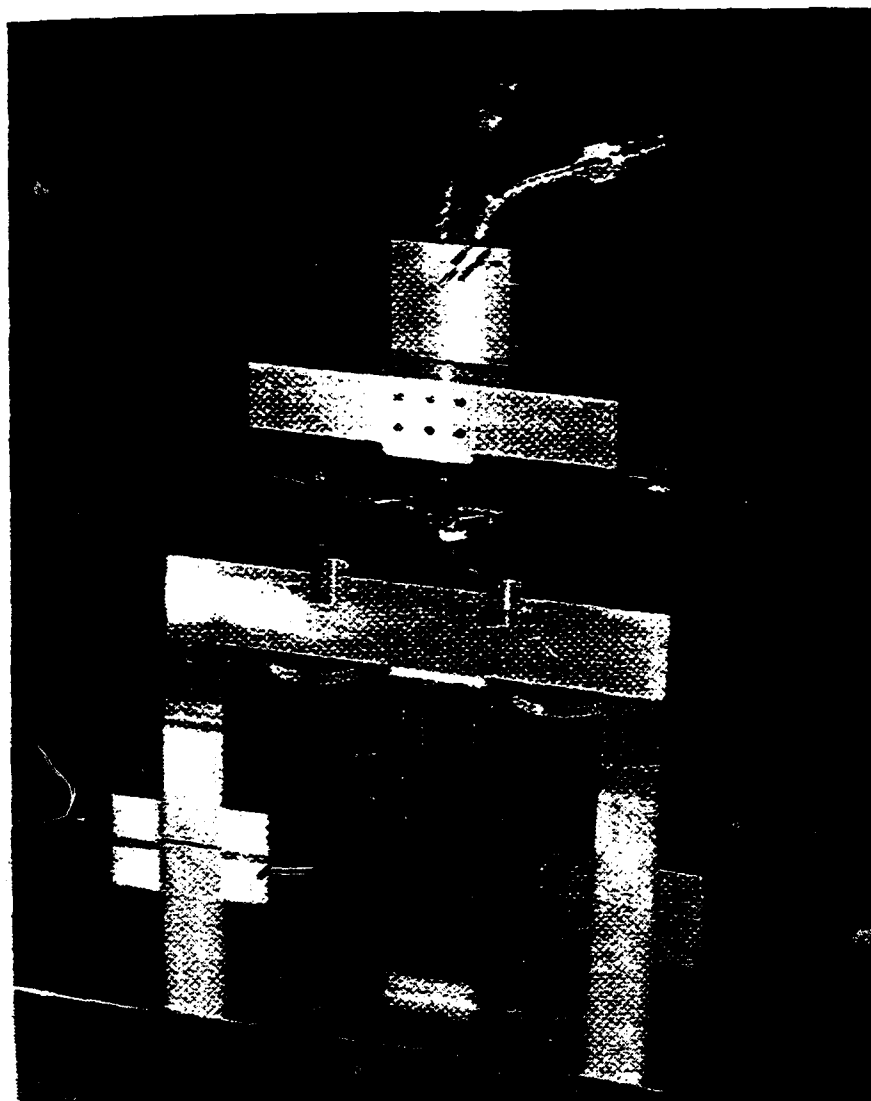
Figure 4.14 This photo shows the NSAM microscope. The width of the base is 4 inches.

4.10 rf Electronics

The electronic circuitry used for feedback and scan control were primarily constructed by Moris Dovek and Chris Lang for use with a STM [22, 23] (Figure 4.15).
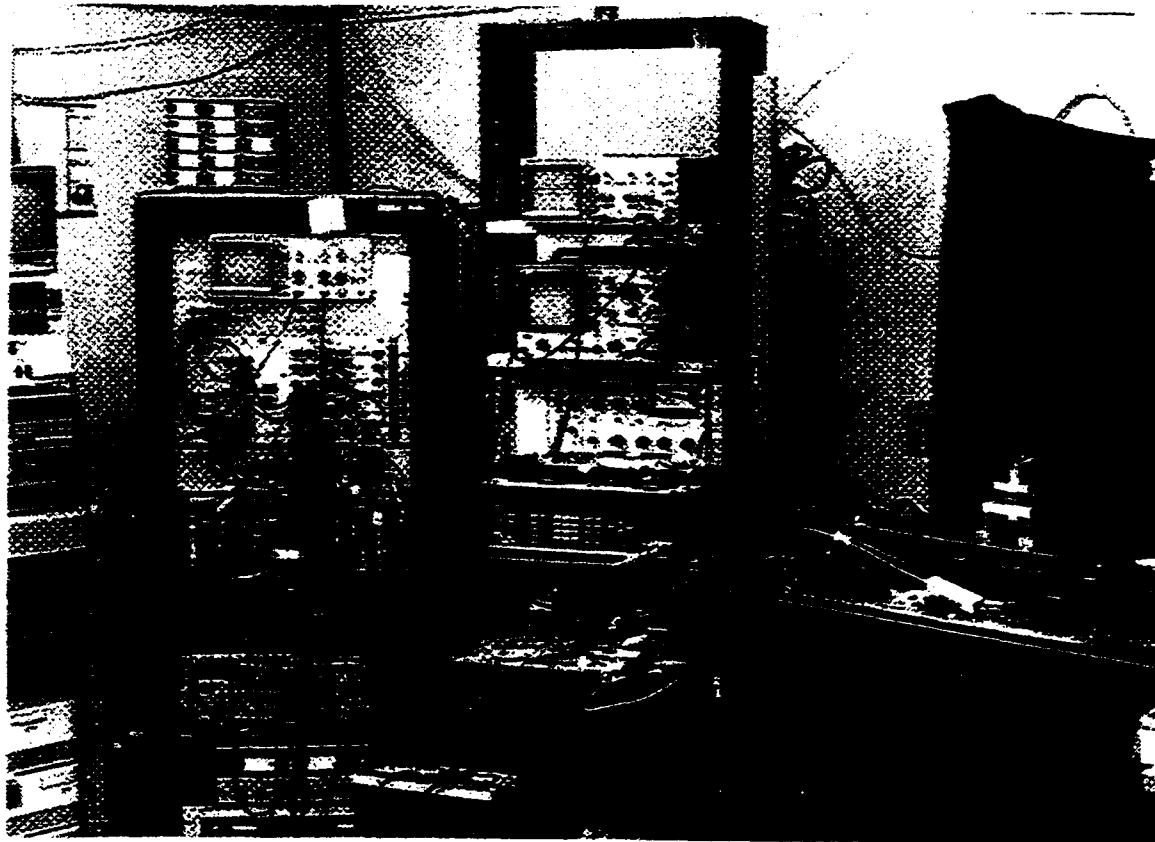
Figure 4.15 This is the necessary rack of electronics to operate the NSAM.

Principal differences between this NSAM and a traditional STM are the electronics necessary to process the rf signals as well as the microfabricated tip and transducer. The general rf electronics configuration is shown in (Figure 4.16).

The master pulser, a Systron Donner 101 Pulse Generator, controls the timing of the entire system. It triggers a HP 8112A 50 MHz Pulse Generator at 100 kHz and the HP pulse generator in turn gates a 100 nS, 1 GHz tone bursts from the Fluke 6062A frequency synthesizer. The tone burst is amplified by a power amplifier up to a peak power of 10 W before being directed through a circulator to the NSAM probe. The third port of the circulator is terminated with a 50 Ω load to prevent reflected signals from re-entering the power amplifier.

Matching networks connected to both the tip and sample transducer are used to tune the transducers to similar frequencies as well as to reduce the impedance mismatch between the 50 Ω coax lines and the acoustic transducers. The rf signal is converted into an acoustic wave by the ultrasonic transducer. The signal then propagates down the tip into the sample and is collected by the receiving transducer mounted on the back of the sample. The received signal is amplified by a Miteq AM-5A-0520 which has 50 dBs of gain and a 1.9 dBs noise figure.

Three FET switches controlled by the master pulser gate out the direct rf feed-through, which arrives almost instantaneously, from the acoustically transmitted signal which arrives after a time interval corresponding to the acoustic time of flight of the tone burst in the tip and sample substrates.

The high frequency signal is then mixed down to a 160 MHz intermediate frequency and amplified again. A crystal detector rectifies the signal and the rectified signal is fed to a Princeton Applied Research boxcar averager with input and output time constants of 100 μs. The output of the boxcar averager corresponds directly to the acoustic power transmitted from the tip into the sample and therefore, this signal is used in the feedback circuit to maintain a constant transmitted power level as the tip is scanned over the surface.

A topographic image of the surface is created by monitoring the feedback signal necessary to maintain a constant acoustic power. The total dynamic range of this system is 129 dBs.
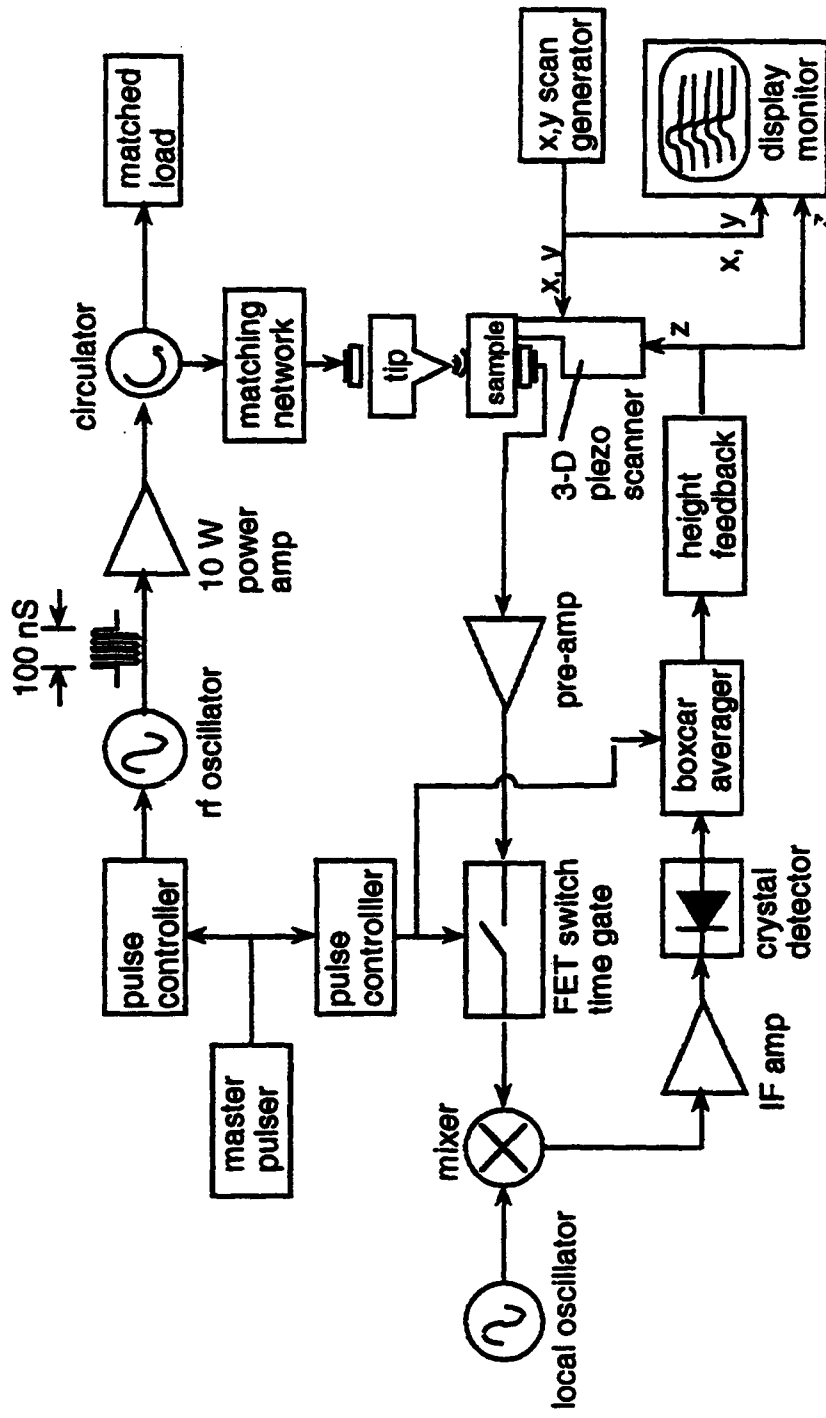
Figure 4.16 The NSAM uses an rf tone burst to generate an acoustic pulse. A heterodyne detection circuit detects the transmitted signal and feeds it to a feedback circuit that maintains the transmitted signal level constant.

References

1) R. A. Lemons and C. F. Quate, Appl. Phys. Lett. **24**, 163 (1974).

2) C. F. Quate, A. Atalar, and H. K. Wickramasinghe, Proc. IEEE **67**, 1092 (1979).

3) B. Hadimioglu and J. S. Foster, J. Appl. Phys. **56**, 1976 (1984).

4) R. C. Bray, C. F. Quate, J. Calhoun, and R. Koch, Thin Solid Films **74**, 295 (1980).

5) B. Hadimioglu and C. F. Quate, Appl. Phys. Lett. **43**, 1006 (1983).

6) J. A. Hildebrand, D. Rugar, R. N. Johnston, and C. F. Quate, Proc. Natl. Acad. Sci. USA **78**, 1656 (1981).

7) J. D. Fox, G. S. Kino, and B. T. Khuri-Yakub, Appl. Phys. Lett. **47**, 465 (1985).

8) E. A. Ash and G. Nicholls, Nature **237**, 510 (1972).

9) K. Takata, T. Hasegawa, S. Hosaka, S. Hosoki, and T. Kumoda, Appl. Phys. Lett. **55**, 1718 (1989).

10) K. Uozumi and K. Yamamuro, Jpn. J. Appl. Phys. **28**, 1297 (1989).

11) P. Güthner, U. Ch. Fischer and K. Dransfeld, Appl. Phys. **B 48**, 89 (1989).

12) J. K. Zieniuk and A. Latuszek, 1986 IEEE Ultrasonics Symposium Proceedings, 1037 (1986).

13) B. T. Khuri-Yakub, C. Cinbis, C. H. Chou and P. A. Reinholdtsen, 1989 IEEE Ultrasonics Symposium Proceedings, 805 (1989).

14) W. D. Pohl, U.S. patent no. 4,851,671.

15) B. T. Khuri-Yakub, G. S. Kino, and P. Gallo, J. Appl. Phys. **46**, 3266 (1975).

16) G. S. Kino, Acoustic Waves: Devices, Imaging, and Analog Signal Processing (Prentice-Hall, Englewood Cliffs, NJ, 1987).

17) J. Hardy, *High Frequency Circuit Design* (Reston, Reston, VA, 1979).

18)   B. Hadimioglu, S. A. Elrod, D. L. Steinmetz, M. Lim, J. C. Zesch, B. T. Khuri-Yakub, E. G. Rawson and C. F. Quate, 1992 IEEE Ultrasonics Symposium Proceedings, in press.

19)   A. R. Selfridge, IEEE Trans. on Son. and Ultrason. SU-32, 381 (1985).

20)   K. Besocke, Surf. Sci. 181, 145 (1987).

21)   Park Scientific Instruments, 1171 Borregas Ave., Sunnyvale, CA 94089.

22)   M. M. Dovek, Ph. D. dissertation, Stanford University (1989).

23)   C. A. Lang, Ph. D. dissertation, Stanford University (1990).

Chapter 5: Transmission Mode Near-Field Scanning Acoustic Microscope Operation

5.1 NSAM Experimental Procedure

The NSAM described in this dissertation can be operated in a transmission mode similar to other transmission NSAMs [1]. In this mode, acoustic waves are coupled from the tip into a sample and are then detected by a receiving transducer on the back of the sample (Figure 5.1). The spacing between the tip and sample is controlled by a feedback circuit that adjusts a piezoelectric positioner to maintain the transmitted acoustic power constant. An image of the surface is obtained by recording the error signal of the feedback circuit as the tip is scanned in a raster fashion over the sample.

Although the operation of the NSAM in transmission mode is reminiscent to that of the STM, there is one important difference: while the tip in STM has constant size and shape, the NSAM tip vibrates longitudinally as acoustic waves travel down its length. The amplitude of the tip displacement, or particle motion, is determined in parts by 1) the shape of the tip and 2) the amount of power reaching the location in the tip where its cross section is comparable in size to half the acoustic wavelength.

There are roughly two regions of interest in the acoustic path from the transducer to the apex of the tip, (Figure 5.2).

90

Figure 5.1 In transmission mode NSAM, acoustic waves are generated by the tip transducer, coupled to the sample through the tip and detected by a second transducer on the back of the sample.

From the tip transducer up to the point in the tip where the cross-section is approximately equal to $\lambda/2$, the loss is proportional to the ratio of the tip cross-section at $x = \lambda/2$ and the area of the transducer. Since the acoustic impedance mismatch of the silicon tip to air is 19.7×10^6 to 0 kg/m^2s, virtually nothing is transmitted from the silicon into the air. In this region, the power density is constant along the longitudinal axis of the tip.
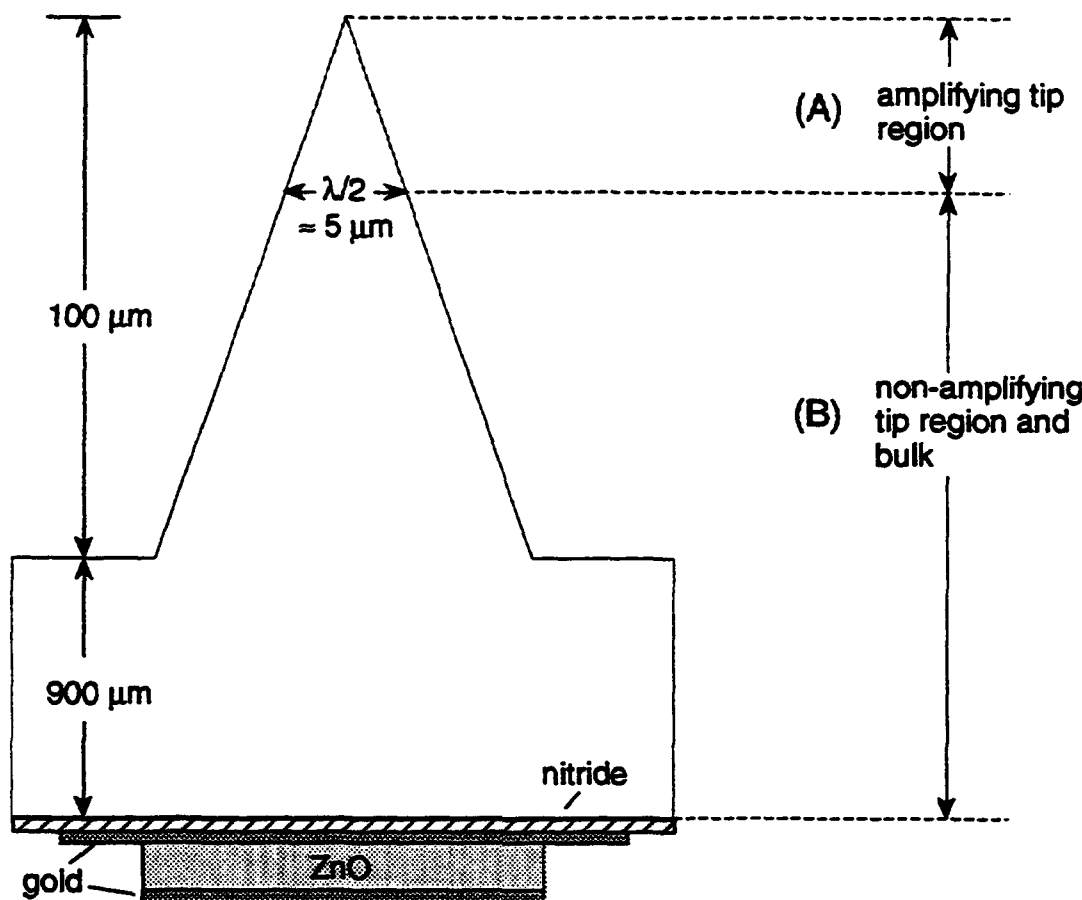
Figure 5.2 The NSAM tip and substrate have two regions of acoustic behavior. Region A has lateral dimension which are small compared to a wavelength. In this region, energy density is not constant and particle motion amplification results. In region B, the energy density is constant.

Acoustically, the most interesting region of the tip is near the apex where its lateral dimensions are comparable to half the acoustic wavelength. The particle displacement in this region is amplified through a phenomena identical to the one exploited in tapering rods for Mason horns and ultrasonic drills [2]. The particle motion in this region is amplified because the tapered shape of the tip acts to increase the power density of the acoustic wave

as it travels down to the apex of the tip. Since the power density is proportional to the square of the strain, as the power density increases, the strain increases resulting in amplified particle motion near the apex of the tip.

The region of the tip undergoing amplified displacement will be referred to as the "amplifying" portion of the tip and the portion of the tip in which the lateral dimensions are much larger than a wavelength will be called the "non-amplifying" portion of tip. For the purposes of this analysis, we assume the the two regions are distinct when in fact, the transition from one regime to the other is understood to be gradual and not clearly delineated. It is the amplified vibration of the tip that is responsible for the large strain that can be coupled from the tip into the sample.

5.2 Acoustic Power Propagation From Tip

The vibration amplitude of the tip can be calculated using a model for elastic motion of a solid cone with known dimensions and input power entering its base [2, 3]. The motion of the particles in the base of the tip can be determined from fundamental acoustic principles but in order to model the motion in the amplifying portion of the tip, it is necessary to determine the input power delivered not to the base of the tip but to a plane in the tip where the width of the cone equals half the acoustic wavelength, for example 11.7 μm at 750 MHz in silicon.

Determining the power reaching the amplifying portion of the tip would be simple if the tip structure were a perfect waveguide in which case the total energy reaching the amplifying portion of the tip would simply be equal to the energy impinging on the tip's base. The power reaching the base of the tip structure is not difficult to determine since the insertion loss of the NSAM transducer and silicon substrate can be measured.

93

Determining the actual acoustic loss in the non-amplifying portion of the tip is difficult but this value must be known before the particle displacement in the amplifying portion of the tip can be calculated.

To determine the loss in the non-amplifying portion of the tip, a hemispherical acoustic lens is focused on the amplifying portion of a NSAM tip and the power received from the NSAM transducer is measured. Knowing the input and output power of such a system, one can subtract all the known components of loss in the acoustic path leaving one unknown component, the loss in the linear portion of the tip structure.

The experimental configuration and the measurement apparatus are shown in Figures 5.3 and 5.4. A hemispherical lens is mounted above the NSAM tip on manual translation stages capable of moving the lens in three, orthogonal directions for coarse alignment. The hemispherical lens has an F# of 0.7 and 1.5 μm spot size. It is designed for operation at 1 GHz. The NSAM tip is mounted on a piezoelectric tube scanner which scans the NSAM tip in the x and y directions underneath the hemispherical lens to produce two-dimensional mappings of the radiated power from the tip. A resistive wire is wrapped around the hemispherical lens housing to heat the water to reduce its attenuation.

P_{in} and $P_{received}$ were measured directly in the transmission experiment. The transmission experiment was conducted at 750 MHz. For an input power, P_{in}, of 1 W. the received power, $P_{received}$, was 12.5 pW, or -109 dB down from the input rf power. The transmitted power versus frequency is shown in Figure 5.5.
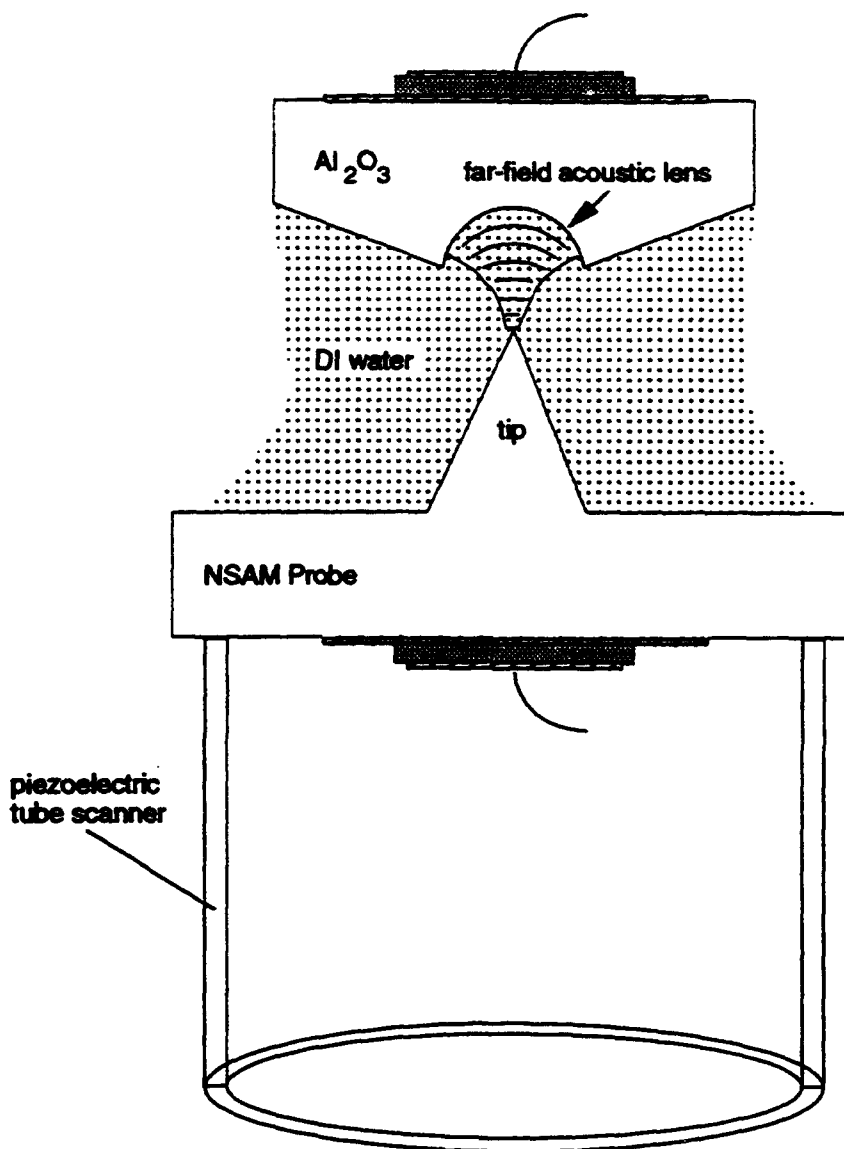
Figure 5.3 The intensity field of the NSAM tip was probed using a far-field acoustic microscope with a hemispherical lens. The NSAM tip was mounted on a piezoelectric tube scanner to allow fine positioning and 3-dimensional scanning.
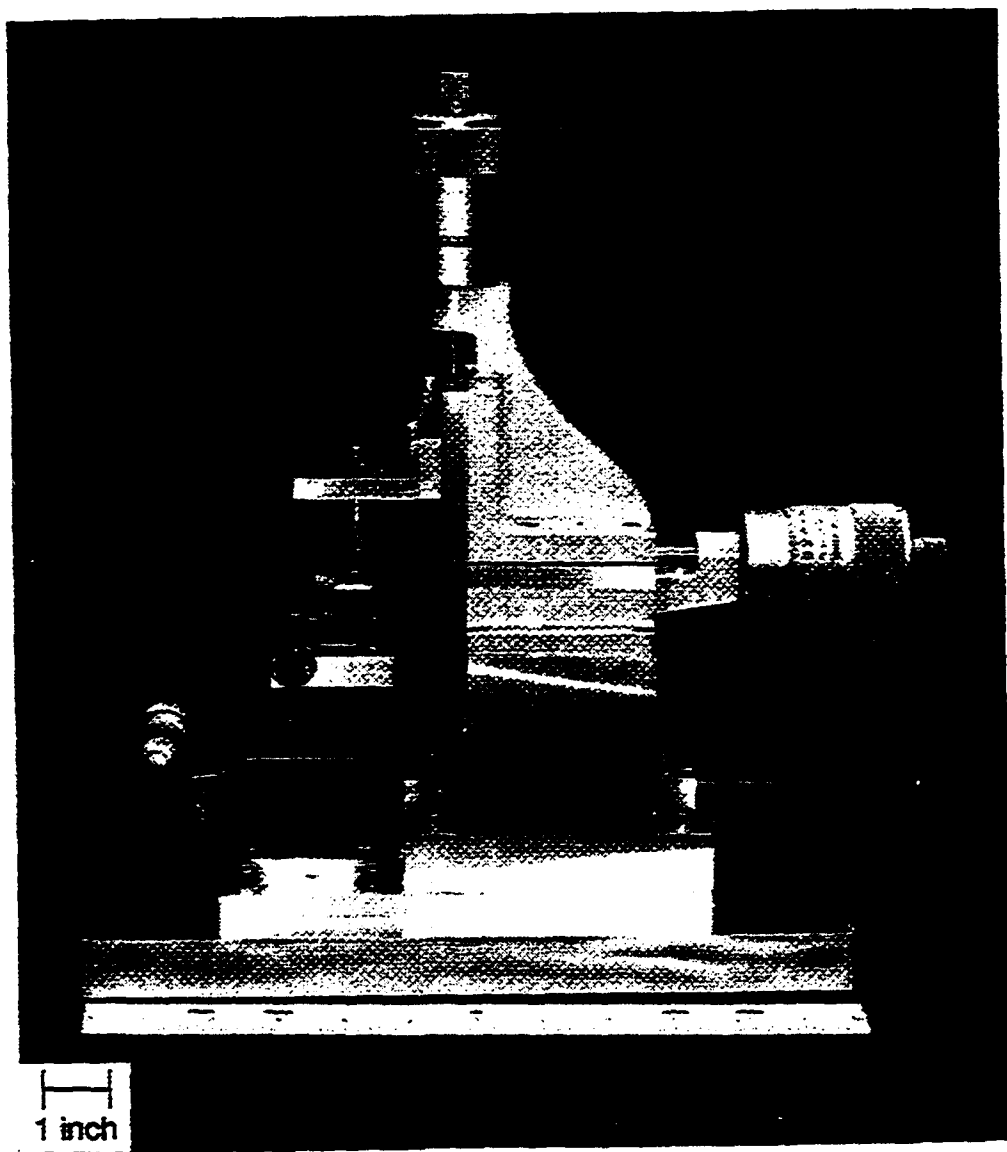
Figure 5.4 The far-field acoustic microscope apparatus is shown here.
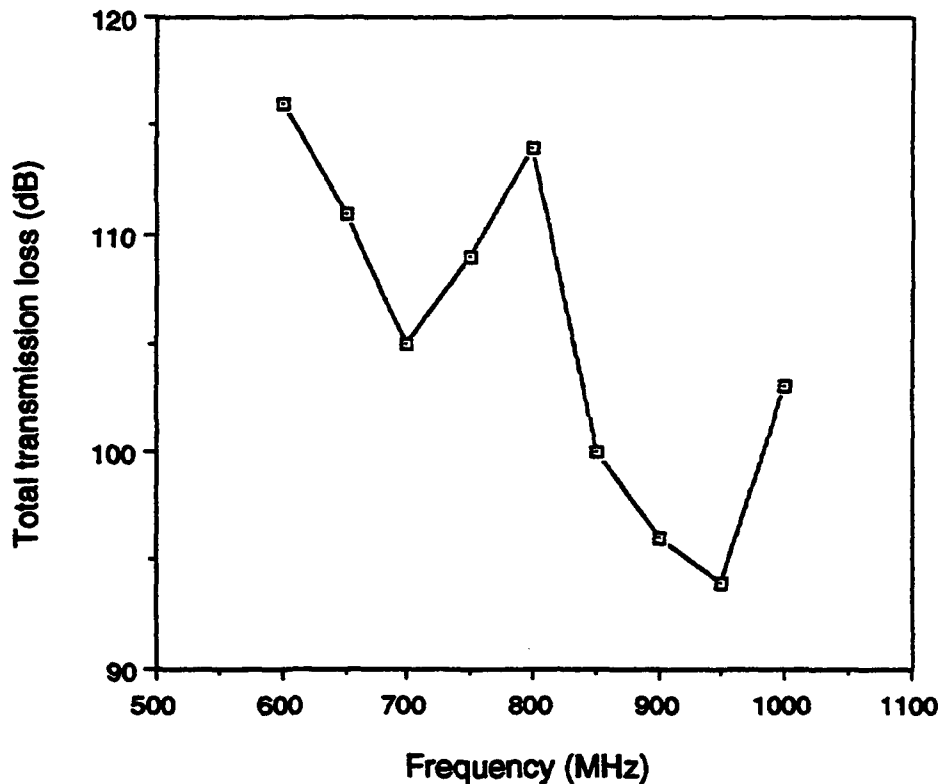
Figure 5.5 The transmission experiment was conducted at 750 MHz where the total loss between the hemispherical acoustic lens and the NSAM tip transducer is 109 dB.

The NSAM tip was scanned under the hemispherical lens by the piezoelectric scanner to obtain a 2-dimensional acoustic intensity image of the tip. An image of the tip taken with the tip apex in the focal plane is shown in Figure 5.6. The bright spot in the center of the image corresponds to the convolution of the diffraction-limited spot size of the lens and the size of the tip. The measured spot is larger than the tip radius since the acoustic signal is received from the entire portion of the tip in the focal volume of the lens

represented by lens' spot size and depth of field. A 1-dimensional scan of the same region taken with the apex of the tip in the focal plane of the lens shown in Figure 5.7. The -3 dB points are approximately 3 μm apart.
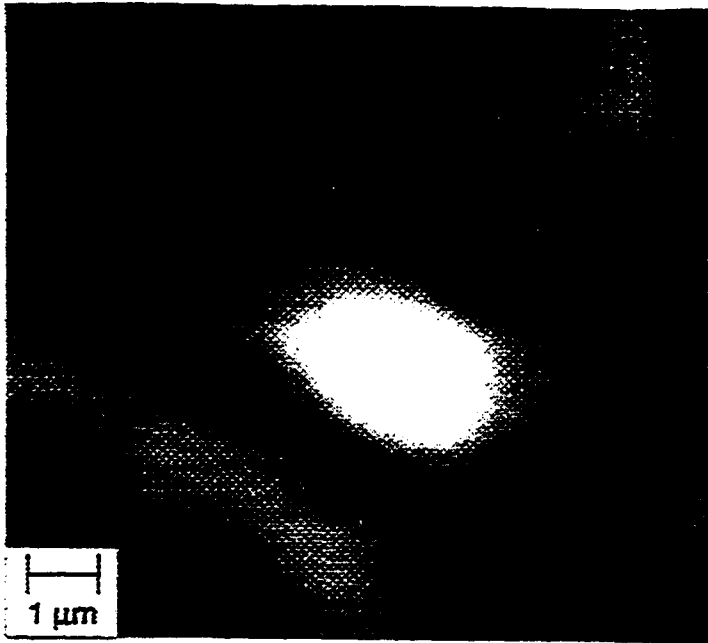
Figure 5.6 This 10 μm x 10 μm far-field acoustic microscope image of the acoustic intensity of an NSAM tip shows the presence of the sharp tip as a bright spot 3 μm wide.

Turning now to an accounting of the losses in the acoustic path for sound transmission from the tip to the lens, the first component of loss in the acoustic path to be considered is the insertion loss of the receiving lens assembly and the attenuation in the water. The sum of these loss mechanisms is determined by launching an acoustic pulse from the lens and measuring the 2-way loss of the signal when it is reflected off of a polished silicon wafer and collected again by the lens.

98
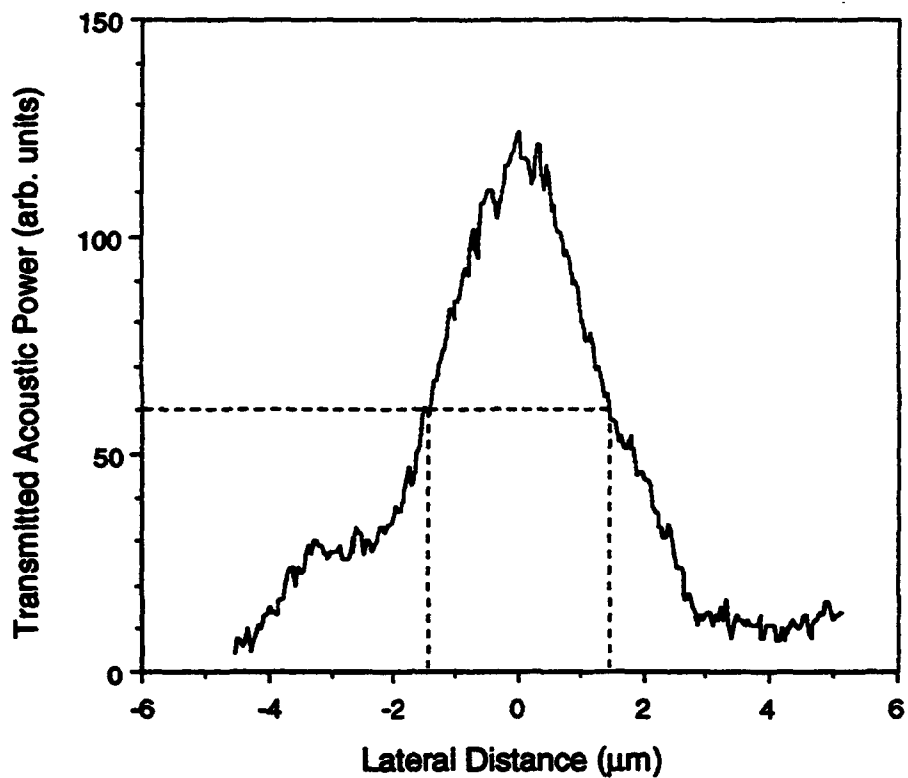
Figure 5.7 The NSAM tip can be scanned under the hemispherical acoustic
tip to map the acoustic intensity profile of the transmitted acoustic signal.
The -3 dB points width of the peak is 3 μm.

0.5 dB of the 2-way loss is attributable to the finite transmission of sound from the
water into the polished silicon reflector. The 1-way loss, calculated as half of the measured
2-way loss, is shown as a function of frequency in Figure 5.8. At 750 MHz, the loss is
-39.5 dB.
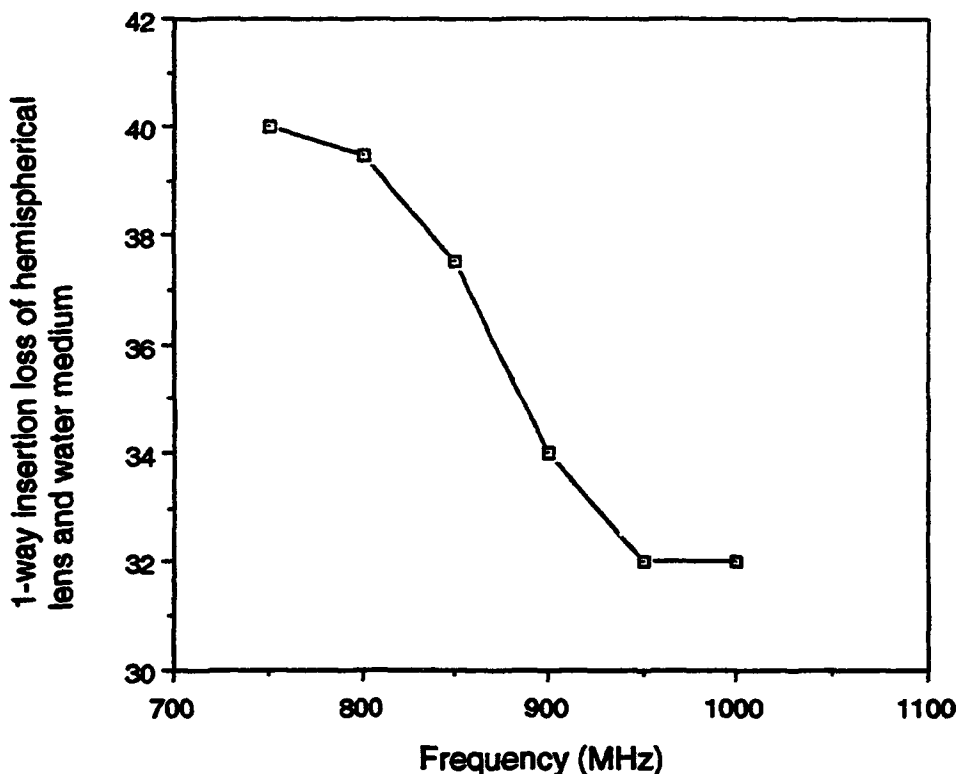
Figure 5.8 1-way transmission loss of the hemispherical lens as a function
of frequency shown here. At the frequency of the transmission experiment,
the loss is -39.5 dB.

The next component of loss is due to the inefficiency of coupling sound into or out
of a small body such as the apex of the tip. In order to determine the magnitude of this loss
mechanism, we examine the impedance mismatch between a small source radiating
spherical waves and the surrounding isotropic medium. This impedance mismatch
determines the transmission coefficient between the source and the medium. It is assumed
to be the same for sound traveling from the medium into the small body as well.

The radius of curvature of a NSAM tip is typically 1000 Å or less. Since the tip radius and gap spacing determine the NSAM's resolution, only the power transmitted from a region 1000 Å, or 0.009 of a wavelength, from the tip apex is of interest. The figure of interest in this experiment therefore is the coupling efficiency between a 1000 Å radius silicon source and a water medium. It is assumed that the sidewalls of the tip are very steep and any acoustic transmissions originating there radiate perpendicularly to the tip sidewall and are not collected by the hemispherical lens.

For a small acoustic source, the displacement velocity and the pressure amplitude are out of phase. This can be understood by noting that the pressure amplitude, T, is equal to the particle velocity times the acoustic impedance, vZ. The following equation describes the acoustic impedance encountered by a spherical wave radiating from a small source [4]

$$Z = \rho_0 c \left[\frac{(kr)^2}{1 + (kr)^2}\right] + j\, \rho_0\, c \left[\frac{(kr)}{1 + (kr)^2}\right] \tag{5.1}$$

where ρ_0 is the density of the medium, c is the phase velocity, k is the wave number, and r is the radial distance from the source. When kr is very large, far from the source, the second term in the equation goes to zero and the acoustic impedance approaches the impedance for a harmonic plane wave [4]

$$Z = \pm\rho_0 c \tag{5.2}$$

Near the source however, the second term dominates and the impedance becomes almost purely imaginary. To obtain even a small value of real pressure amplitude, the real particle displacement near the source must be very large. Therefore, the power radiation of a very small source is quite inefficient.

The equivalent impedance of the water medium seen by a spherical wave radiating from a 1000 Å sphere is 1.3×10^5 kg/m^{2}s according to equation 5.1. The transmission coefficient from silicon ($Z_{si} = 19.7 \times 10^6$ kg/m2s) into this equivalent impedance of water is 0.026, or -16 dBs. The coupling of sound from water into a small silicon sphere is also assumed to encounter the same impedance mismatch and therefore the same 16 dBs loss.

The next region in the acoustic path to be examined extends from the tip's apex to a plane where the lateral dimension of the tip is $\lambda/2$. This is the portion of the tip which experiences amplified motion. Since it is a relatively short region and the sidewalls are steeply sloped, we assume that no loss occurs in this region. The power density increases as the cross-sectional area of the tip decreases. These factors result in amplified particle motion in the fashion of a Mason Horn.

Skipping the non-amplifying portion of the tip for the present, the next loss component is the NSAM substrate and transducer itself. The magnitude of this loss component is evaluated by measuring the 2-way loss of a signal traveling from a transducer through the substrate and reflecting off of the polished silicon/air interface. The reflection from the silicon/air interface is almost 100% since the acoustic impedance of air is nearly 0. The 1-way insertion loss of the tuned NSAM transducer was shown in Figure 4.10. At 750 MHz, this component accounts for 7.5 dB of loss. Some additional power will be lost since the area of the tip's base is small and some power from the transducer will fall outside of this area. In the following discussion, this extra loss element will be lumped with the loss attributed to the non-amplifying portion of the tip.

Having accounted for all of the known loss mechanisms, the loss in the non-amplifying portion of the tip can now be determined. The total acoustic loss in the non-amplifying portion of the tip, L_{tip}, is given by the following equation

$$L_{tip} = P_{in} - P_{received} - L_{lens\ and\ liquid} - L_{point\ source}$$
$$- L_{tip\ substrate} \qquad (5.3)$$

where L_{tip} is the loss in the non-amplifying portion of the tip, P_{in} is the total power input,
$P_{received}$ is the received power, $L_{lens\ and\ liquid}$ is the loss of the hemispherical lens,
transducer and water, $L_{point\ source}$ is the loss due to inefficient radiation from a small
acoustic source and $L_{tip\ substrate}$ is the loss of the NSAM transducer and substrate.

P_{in}	1 W
$P_{received}$	12.5 pW
$L_{lens\ and\ liquid}$	-39.5 dB
$L_{point\ source}$	-16 dB
$L_{tip\ substrate}$	-7.5 dB
L_{tip}	-46 dB

Table 5.1 Total transmitted power, received power and values for each
component of loss are shown in this table. The operating frequency of the
experiment is 750 MHz.

Substituting the values from Table 5.1 into equation 5.3 yields the total loss in the
tip from the base up to a point in the tip where its cross-section is roughly half of a
wavelength. The loss in the non-amplifying portion of the tip, L_{tip}, is thus determined to
be -46 dBs.

-20 dBs of the -46 dBs of loss in the tip can be attributed to the difference in areas
between the transducer and the cross-section of the tip where its diameter equals half the
acoustic wavelength. The remaining -20 dBs may be due to error introduced in calculating

103

the radiation efficiency of the last 1000 Å of the tip, previously modeled as a radiating sphere.

In summary, when the NSAM tip is excited at its base by an acoustic wave, a total loss in signal of 53.5 dBs is incurred before wave reaches the amplifying portion of the tip. For a 1 W input rf power pulse, 4.5 μW reaches the amplifying portion of the tip.

5.3 Tip Motion Due to Acoustic Excitation

As described in the previous section, when the NSAM tip is excited by an acoustic wave at its base, the displacement of the particles varies according to their position in the tip (Figure 5.9).
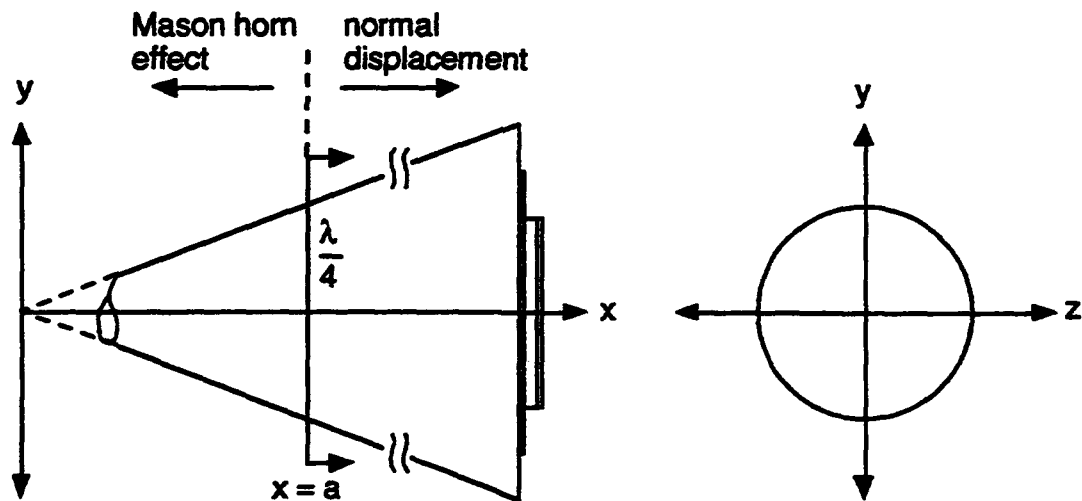

Figure 5.9 The particle motion in the tip is a function of the location of the particle in the tip. The figure above after Graff [3] indicates the axes which will be used in the analysis of the particle motion.

In the non-amplifying region near the base of the tip, the particle velocity, v, is proportional to the ratio of stress, T, to the acoustic impedance , Z [5] as shown

$$v = \frac{T}{Z} \qquad (5.4)$$

The acoustic impedance in the non-amplifying region is a material constant and therefore, the particle velocity is simply proportional to stress.

In the portion of the tip where the lateral dimension is comparable to half the acoustic wavelength, the impedance is no longer constant and begins to have an imaginary component. In this region, the particle motion is described by the following equation [3]

$$U(x,t) = \left(\frac{-F_0}{E\ A_0\ \beta}\right)\left(\frac{a}{e^{i\beta a}\left(1+\frac{i}{\beta a}\right)}\right)\left(\frac{-ie^{i\beta x}}{x}\right)e^{-i\omega t} \qquad (5.5)$$

F_0 is the force of the driving function at a plane in the cone where the lateral dimension is half of a wavelength, E is Young's modulus of the cone material, A_0 is the cross-sectional area of the cone at a point $x = a$. The propagation constant, β, is equal to ω/v_a. As x becomes very small near the apex of the tip, the displacement amplitude increases in inverse proportion to x.

The force at the point in the cone $x = a$, where the diameter is equal to half of a wavelength, can be calculated from the relation between power and force [5]

$$F = (P\ A\ Z)^{1/2} \qquad (5.6)$$

where P is power, A is the cross-sectional area and Z is the acoustic impedance. The power reaching the amplifying portion of the tip was determined in the previous section as 4.5 μW. The input conditions for the model of the NSAM tip's motion are shown in Table 5.2.

A computer program was written to evaluate equation 5.5 for particle motion as a function of distance. The particle displacement amplitude is plotted against distance along the tip's longitudinal axis in Figure 5.10. As expected, the graph demonstrates that the particle motion amplitude increases near the apex of the tip.

F_0	48 μN
$E_{silicon}$	1.9×10^{11} N/m2
Area	27 μm^2
ω	2π (750 MHz)
v_a (silicon, long.)	8.8 km/s
β	535×10^3 m^{-1}

Table 5.2 The values shown here are used in the model describing the amplified particle motion of the tip.

In the case of our NSAM, the distance of most interest is about 1000 Å since this is the approximate radius of curvature for the NSAM tips. At distances less than 1000 Å, the true tip shape deviates significantly from the conical geometry assumed in the model. At a distance of 1000 Å, the tip displacement amplitude is 17 Å, corresponding to a strain of 1.5 x 10^{-4} for an 11.7 μm wavelength. Although the strain limit of silicon is not well-defined, it is believed to be on the order of 10^{-4} [6] and therefore comparable to the strain due to the calculated particle displacement of the tip undergoing amplified motion.
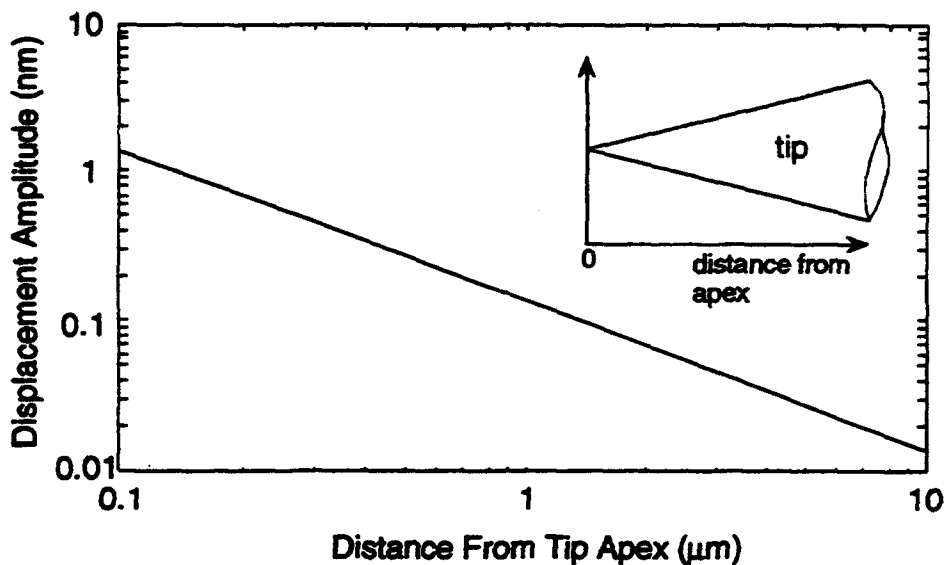
Figure 5.10 A calculation of equation 5.5 yields this curve demonstrating how the particle motion is amplified near the apex of the tip where the lateral dimensions of the tip are comparable to the acoustic wavelength.

5.4 Acoustic Transmission Mechanisms

There are several ways in which the strain from the tip can be coupled into the sample. In one non-contacting mode [1], the tip is brought 10 to 100 Å of the sample and the acoustic wave is thought to be coupled by van der Waals forces. These forces are always attractive and drop off as d^{-2} in the case of a sphere separated from a plane by the distance, d [7].

In non-contacting mode AFMs, which also utilize van der Waals forces, the typical force applied between the tip and sample is on the order of 10^{-11} N [8]. In our NSAM, the detection circuitry is not phase sensitive and therefore does not distinguish between attractive and repulsive forces.

107

If the tip contacts the surface, strain can be coupled through an intermittent contact in which the tip touches the sample over only part of its displacement cycle. In this mode since the applied force is a clipped sinusoid, higher frequency terms are expected to be excited.

If the force between the tip and sample is sufficiently large, a Hertzian contact is formed in which elastic deformations bring the tip and planar sample into contact over a circular area with radius a_c. It has been shown that transmission through such a Hertzian contact for a spherical body with radius of 20 cm contacting a planar sample can have transmission loss as small as -1.19 dB at 7 GHz [9].

An analysis of Hertzian contacts for isotropic materials is provided by Landau and Lifshitz [10]. Although the tip material in our system, silicon, is a highly anisotropic material, the first order solutions afforded by these formulations can give insight into the system at hand.

In a Hertzian contact, the radius of the contact area is specified by the following equation [9, 10]

$$a_c = (F \, B \, R)^{1/3} \tag{5.7}$$

where F is the force between the two bodies, B is an elastic constant which is a function of Poisson's ratio and Young's modulus, and R is the radius of the tip. The elastic constant B in this case is given by

$$B = \frac{3}{4}\left(\frac{1-\sigma_a^2}{E_a} + \frac{1-\sigma_b^2}{E_b}\right) \tag{5.8}$$

where σ_a and σ_b are the Poisson's ratios of the tip and sample material respectively. E_a and E_b are the Young's moduli for the tip and sample materials respectively. If the tip and sample are of the same material, B can be expressed as

$$B = \frac{3}{2}\left(\frac{1-\sigma_a^2}{E_a}\right)$$

(5.9)

The Young's modulus and Poisson's ratio for silicon are 1.9×10^{11} N/m^2 [11] and 0.22 [12] respectively. For a silicon tip contacting a silicon sample, the elastic constant, B, is 7.51×10^{-12} m^2/N. The typical NSAM tip's radius of curvature is 500 to 1000 Å. The radius of contact for a 1000 Å radius silicon tip making a Hertzian contact with a silicon sample with a force of 10^{-8} N is 20 Å. The Hertzian contact radius as a function of applied force and tip radius is shown in Figure 5.11.

The fact that the contact radius is on the order of just a few nanometers is important since if it were large, the contact area could limit the lateral resolution of the NSAM. In fact, the observed lateral resolution of the microscope appears to be approximately 1000 Å indicating that the contact area of the Hertzian contact is not a limiting factor in the microscope's lateral resolution.

The magnitude of the elastic deformation, h, is given by [10]

$$h = F^{2/3}\left(\frac{B^2}{R}\right)^{\frac{1}{3}}$$

(5.10)

A 1000 Å radius tip contacting a surface with 10^{-9} N of force deforms 0.09 Å. This deformation represents a strain on the order of 10^{-5} which is less than the expected elastic limit of silicon, on the order of 10^{-4} [6].

109
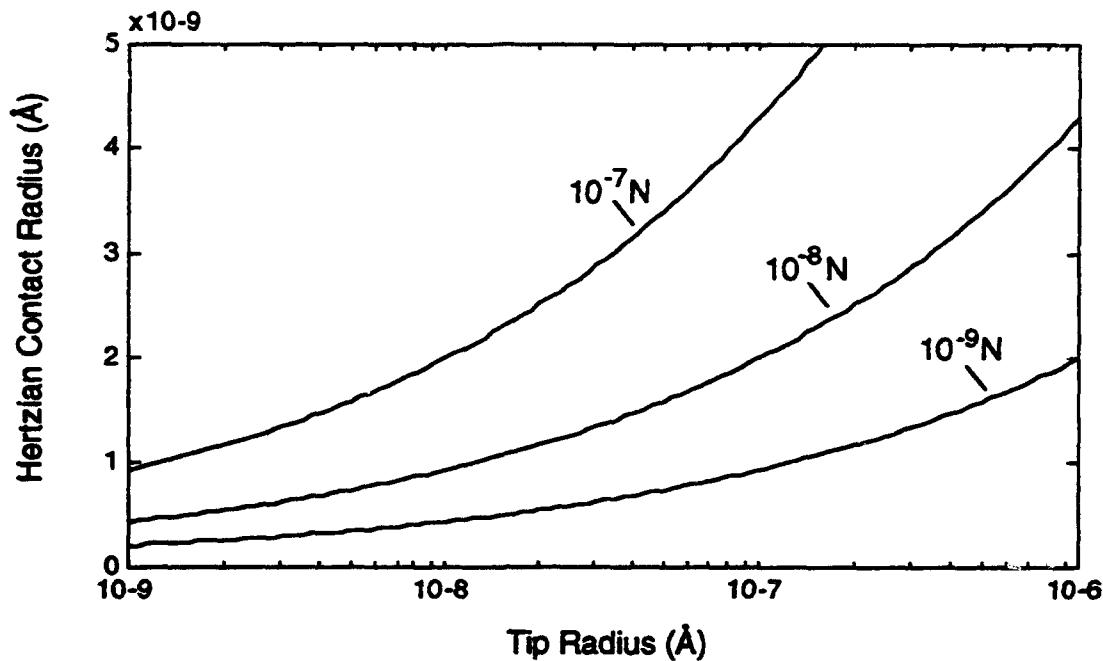
Figure 5.11 The Hertzian contact radius versus tip radius curves shown here are calculated from equation 5.7. Hertzian contact radius is a weak function of tip radius and applied force.

5.5 Distance Dependence of Signal

In near-field scanning probe microscopy, the resolution is determined by the sharpness of the tip and the working distance between the tip and the sample. The tip sharpness and the working distance necessary to obtain a certain level of resolution is in turn strongly dependent on the distance dependence of the interaction between the tip and the sample.

It is a common misconception that the STM achieves atomic resolution because the tips used in STM terminate at one atom. In fact, the tips used in STM commonly have microscopic radii of curvature in excess of 1000 Å. The STM's exquisite lateral resolution

110

derives from the fact that the tunneling current decreases exponentially with increasing

spacing between the tip and sample such that if a single atom on the tip is even one atomic

diameter closer to the sample than its neighbors, it conducts most of the tunneling current

[13]. It is the confinement of the tunneling current to one or two atoms on the tip that

allows STM to obtain atomic resolution images even with tips that are blunt on the

microscopic scale.

For scanning probe microscopes in general, the less sensitive the interaction

between the tip and the sample, the sharper the tip must be in order to confine the

interaction to a small lateral area. As shown in Figure 5.12, if the vertical sensitivity is

given by V_b, the interaction between the tip and the sample is limited to lowest local

asperity and the lateral resolution is given by R_b. If however, the signal is less vertically

sensitive, as indicated by V_a, other local asperities can interact with the sample degrading

the lateral resolution from R_b to R_a.

The dependence of lateral resolution on vertical resolution hints that there are two

paths that can be pursued in order to increase lateral resolution, one is to produce

increasingly sharper tips which have no undesired asperities and the other path is to try to

increase the distance sensitivity of the interaction between tip and the sample. If the vertical

sensitivity is high enough, such as in the case of STM, the microscopic tip sharpness is not

critical.

Vertical sensitivity is determined by measuring the interaction signal as a function of

distance between the tip and sample. The transmitted acoustic signal as a function of the

distance is measured by bringing a tip close to a sample and monitoring the transmitted

acoustic signal as the spacing between the tip and sample is modulated by the application of

a sinusoidal voltage to the z piezo of the tube scanner.

111
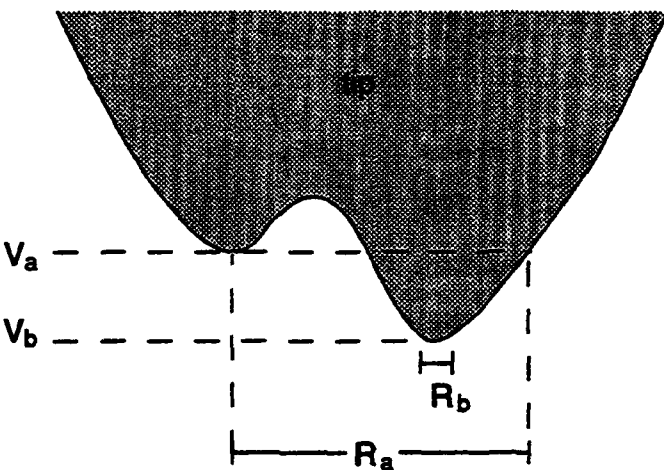
Figure 5.12 In near-field scanning probe microscopes, the lateral and
vertical resolutions are not independent. If the vertical resolution is poor,
V_a, then the near-field signal will be received from an area that could include
multiple asperities. If the vertical resolution is good, V_b, then all of the
interaction occurs at one asperity and lateral resolution improves.

The transmitted acoustic signal is identified both in the frequency and the time
domains. The signal can be identified in the frequency domain since the frequency of the
local oscillator can be selected to detect signals only at the transmitting frequencies of the
ultrasonic transducers. The signal can be localized in the time domain by knowing the
acoustic velocities and thicknesses of both the tip and sample substrates. From these
values, it is possible to calculate the transit time of the acoustic pulse from tip transducer to
the receiving transducer.

When monitoring the received acoustic power signal on an oscilloscope, there is a
large, received pulse at time $t = 0$ corresponding to the rf signal which feeds through the air
between the power amplifiers and the detection circuits. To distinguish between the
directly coupled rf signal and the transmitted acoustic signal, a time gate is placed at $t = t_1$,

where t_1 corresponds to the expected delay of the acoustic signal passing through the tip and sample materials, so that only the signal which has undergone the appropriate delay associated with acoustic propagation is detected.

A typical signal vs. distance plot is shown in Figure 5.13. The received acoustic power is shown on the vertical axis and the distance between the tip and sample is shown on the horizontal axis. The acoustic frequency is 654 MHz. The vertical axis is not very linear but one division represents approximately 1 pW of power. The horizontal axis is 60 Å per division as calculated from the sensitivity of the piezo tube and applied voltage. For the vertical sensitivity and signal-to-noise ratio exhibited in Figure 5.13, the vertical resolution of the instrument is approximately 15 Å.
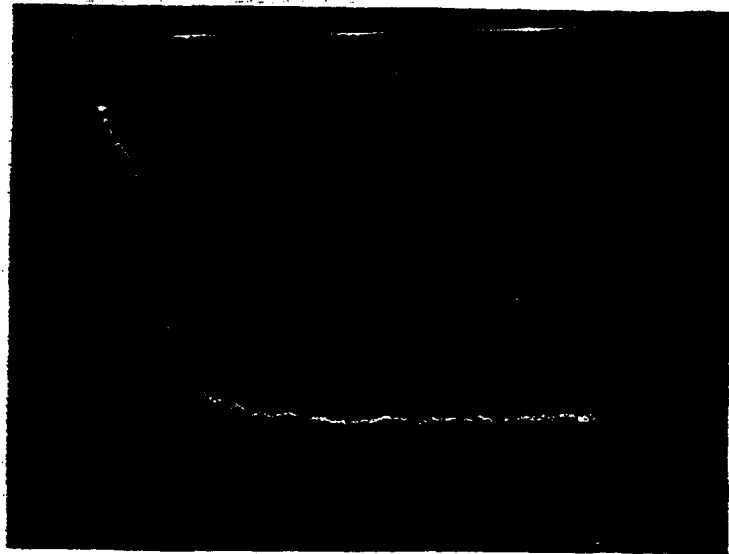

Figure 5.13 A typical signal vs. distance graph is shown in this oscilloscope photo. The lateral and vertical axes are 60 Å/division and approximately 1 pW/division respectively.

One difference between the acoustic signal versus distance curve of NSAM and the force versus distance curves commonly measured in AFM is that the NSAM curve does not have a snap-in or snap-back point. The snap-in point appears in AFM force versus distance curves as the tip approaches the sample and comes into contact with a thin liquid contamination layer which exerts a large attractive force on the cantilever causing it to "snap in" to the sample. When withdrawing the tip from the sample, the tip must be pulled further away from the sample before the meniscus force of the contamination layer can be overcome and the cantilever is released causing the tip to "snap back" [14].

The NSAM is more like the STM than the AFM with respect to the fact that in the NSAM has no flexible component. Since the NSAM tip is rigid like the STM tip, it can not be pulled into the sample by a surface contamination layer thus explaining the absence of a snap-in point. That is not to say however, that the surface contamination layer plays no effect in signal versus distance curve of the NSAM. Even though the surface contamination layer can not pull the tip into the sample, when it wicks up onto the tip (Figure 5.14), it can act as a medium for conducting the acoustic signal from the tip to the sample.

The effect of acoustic propagation through such a contamination layer is to degrade the lateral resolution of the instrument since the contamination layer represents a larger cross-sectional contact area than would be expected from a Hertzian contact alone. Additionally, the vertical resolution is also degraded since the signal does not decay as quickly with increasing distance as long as the contamination remains in the gap and serves to conduct the acoustic waves from the tip into the sample.
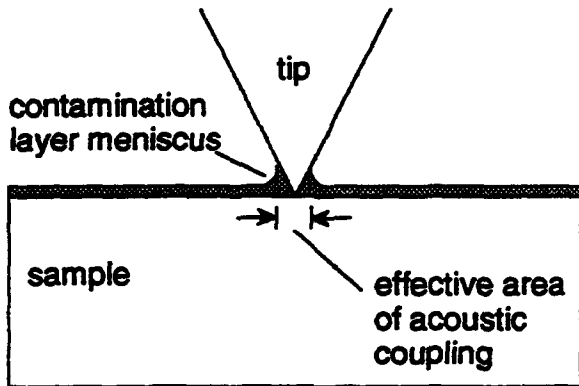
Figure 5.14 A contamination layer exists on almost all samples exposed to atmosphere. This layer can behave as a liquid film and its meniscus force exerts an attractive force on the tip. Acoustic energy can couple between the tip and sample through the contamination layer compromising lateral resolution.

It should be noted that the NSAM's transmitted signal versus distance curve is somewhat less informative than either the STM's current versus distance or the AFM's force versus distance curves. In the case of the NSAM's curve, it is not possible from this information alone to determine the point where the tip comes into contact with the sample. In STM, the signal saturates and the bias voltage goes to zero when the surface is contacted. No such convenient zero point exists in the NSAM's signal versus distance curve.

Another drawback to the NSAM's curve is that it is not calibrated in a meaningful way. In AFM, the force can be calculated by measuring the displacement of the cantilever and knowing the force constant of the cantilever used. In the STM, the transmitted current is measured directly. In the NSAM, the measured quantity is transmitted acoustic power and it can not be easily correlated to force. In short, in NSAM, it is possible to plot the

variation of the acoustic power with distance but it is not possible in a first order analysis to
determine the contact point or applied force.

Figure 5.15 is a graph comprised of data points taken from the curve in Figure
5.13. The data points are scatter plotted and fitted with an exponentially decaying function
whose decay length of 62 Å. In comparison, the decay length of the tunneling current
signal in STM is approximately 1 Å and the STM can be sensitive to vertical displacements
as small of 0.01 Å [13].

$$y = 5.2\ e^{-0.016x}$$
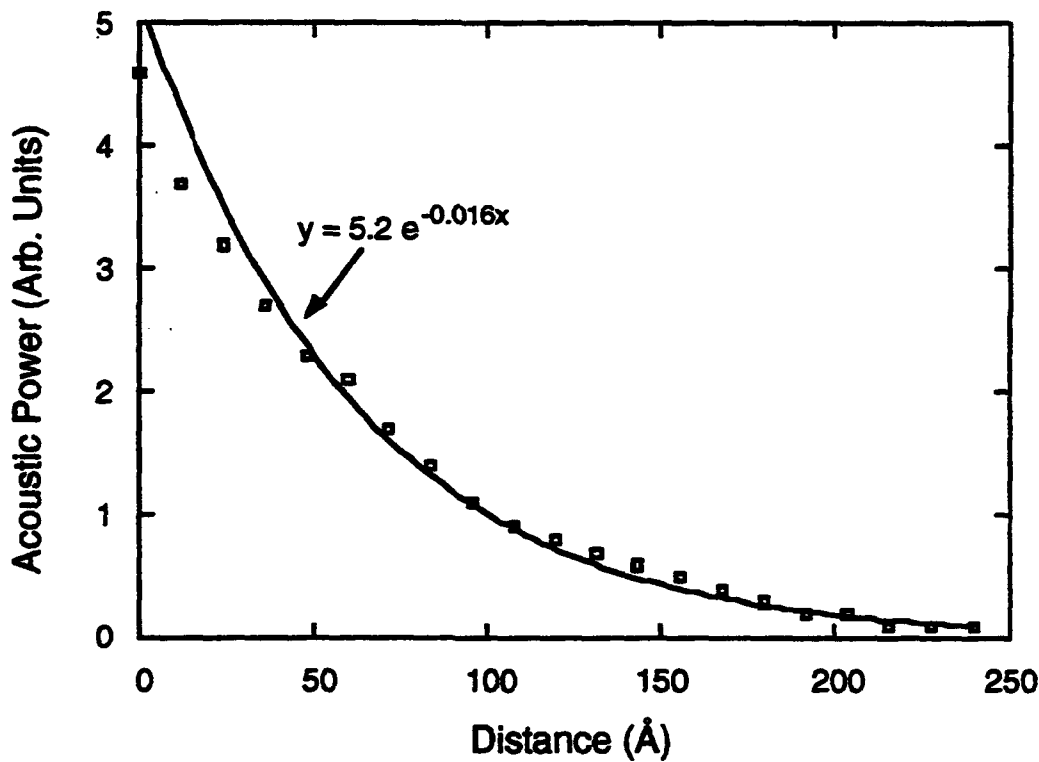
Figure 5.15 Data points from Figure 5.13 are scatter plotted
and curve fit to a decaying exponential curve.

5.6 Tip Damage

Damage to NSAM tips falls principally into three categories. The first category, damage caused by "tip crashes", is familiar to anyone who has had experience working with STM. Since neither the STM nor the NSAM have a flexible component such as the force sensing cantilever in AFM, if the feedback circuit loses control of the tip for even an instant, the tip can be pressed into hard contact with the sample in severe cases the tip can be crushed into the surface. STM researchers often find, after obtaining atomic resolution images, that the sharpened tungsten wire tip is "fish hooked". Catastrophic tip damage, being common to many forms of scanning probe microscopes is not of particular interest here. The two other forms of tip damage are more specific to NSAM with microfabricated tips and will be considered individually in the following subsections.

5.6.1 Acoustically Induced Tip Damage

The amplifying effect of acoustic waves traveling in a sharp tip was discussed in Section 5.3 and calculated to be 17 Å for an input rf power of 1 W. Such a displacement represents approximately 1.5×10^{-4} strain for a 750 MHz acoustic wave in silicon having an 11.7 μm wavelength. Since the elastic limit of silicon is on the order of 10^{-4} a 17 Å particle displacement may cause permanent, inelastic damage. If the power is increased from 1 W to 10 W by the use of a higher power amplifier, the particle displacement at the end of the tip becomes 45 Å which is approximately a strain of 3.8×10^{-4} which may exceed the strain limit of silicon. An additional increase in power may arise from a particularly efficient matching network. A 10 dB difference in insertion loss can exist between two transducers with similar matching networks.

117

Figure 5.16 (a) shows a tip before being acoustically excited. Figure 5.16 (b) shows the same tip after it was acoustically excited with 10 W input rf power. Although the tip was not approached to any sample, significant damage is evident. The pattern of damage is inconsistent with other instances of tip damage resulting from simple contact with a sample. Furthermore, the damage on the tip begins where its cross section is roughly 5 μm, or half the acoustic wavelength. This is the point at which the Mason horn model predicts that the amplification of the particle motion begins to occur. This is an example of tip damage due to acoustic excitation alone.

5.6.2 Tip Damage Due to Non-Ideal Hertzian Contact

In addition to damage caused by overly powerful acoustic waves, a second cause of tip damage is non-ideal Hertzian contacts. Hertzian contacts by nature are assumed to be formed by elastic deformation of two bodies. In practice however inelastic deformations can occur. Figure 5.17 (a) shows a tip before use. The tip was then used in transmitted signal versus distance measurements and as part of the measurement process, the tip was approached to a sample 20 times. The resulting damage to the sample can be seen in the SEM micrograph of the tip shown in Figure 5.17 (b). Unfortunately, it is difficult to make a direct comparison from these picture since the perspective of the tip is different in each picture. Nonetheless, one can see that the very fine spear-like asperities at the apex of the tip in the first SEM have certainly been destroyed by the time of the second SEM.
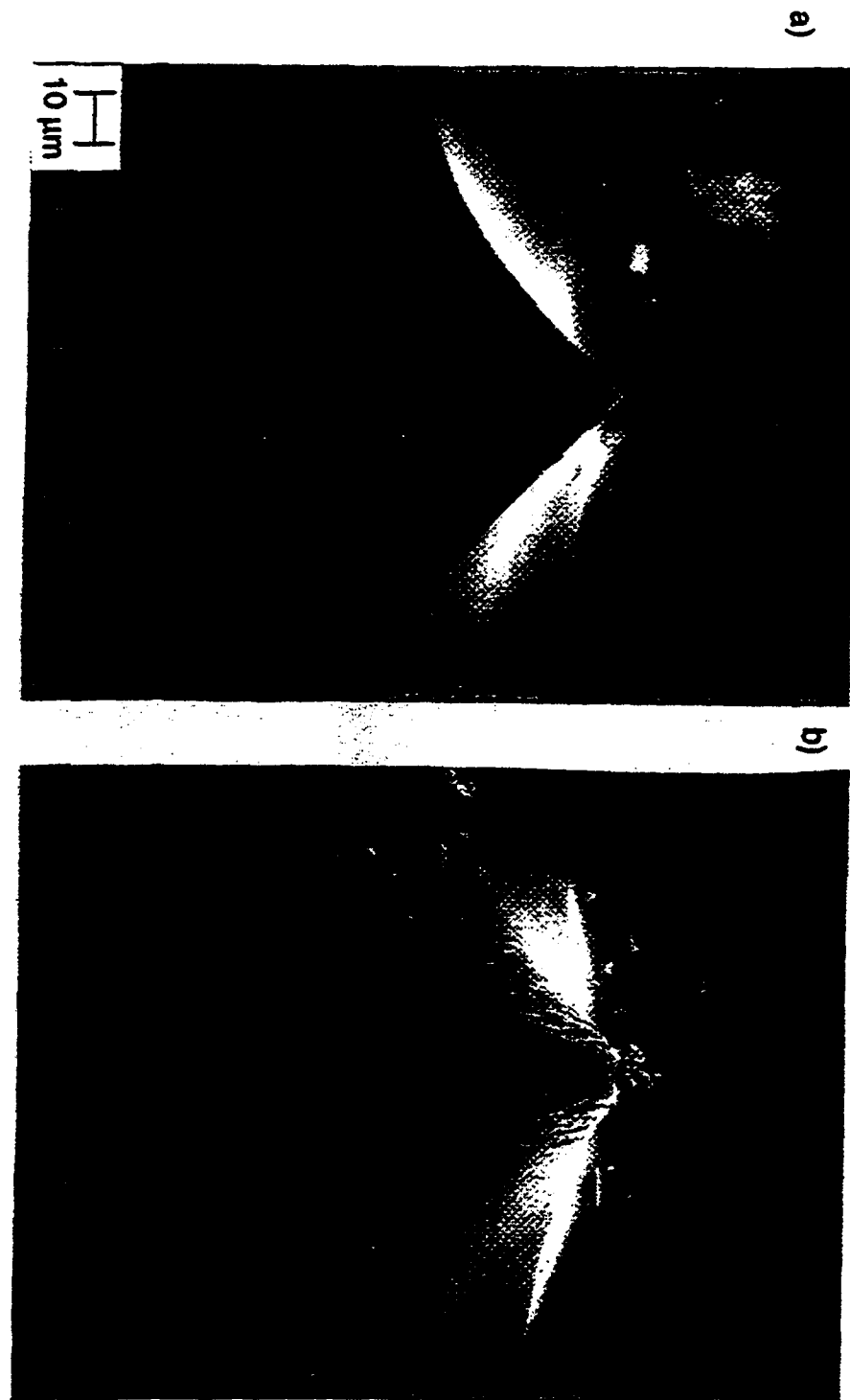
Figure 5.16 a) This tip before acoustic excitation shows no damage. b) After excitation with 10 W of rf power, the tip was heavily damaged even though it was not brought into contact to any sample.

The plateau-like structure at the tip apex after use may be a contamination particle that became attached to the tip during use. Although these SEM photos give some indication of the magnitude of tip damage caused by non-ideal Hertzian contacts, the damage due to this mechanism during imaging may be less than that shown here because while making the transmitted signal versus distance measurements, the tip transmits at least ten times more power than is used during normal, transmission mode imaging.
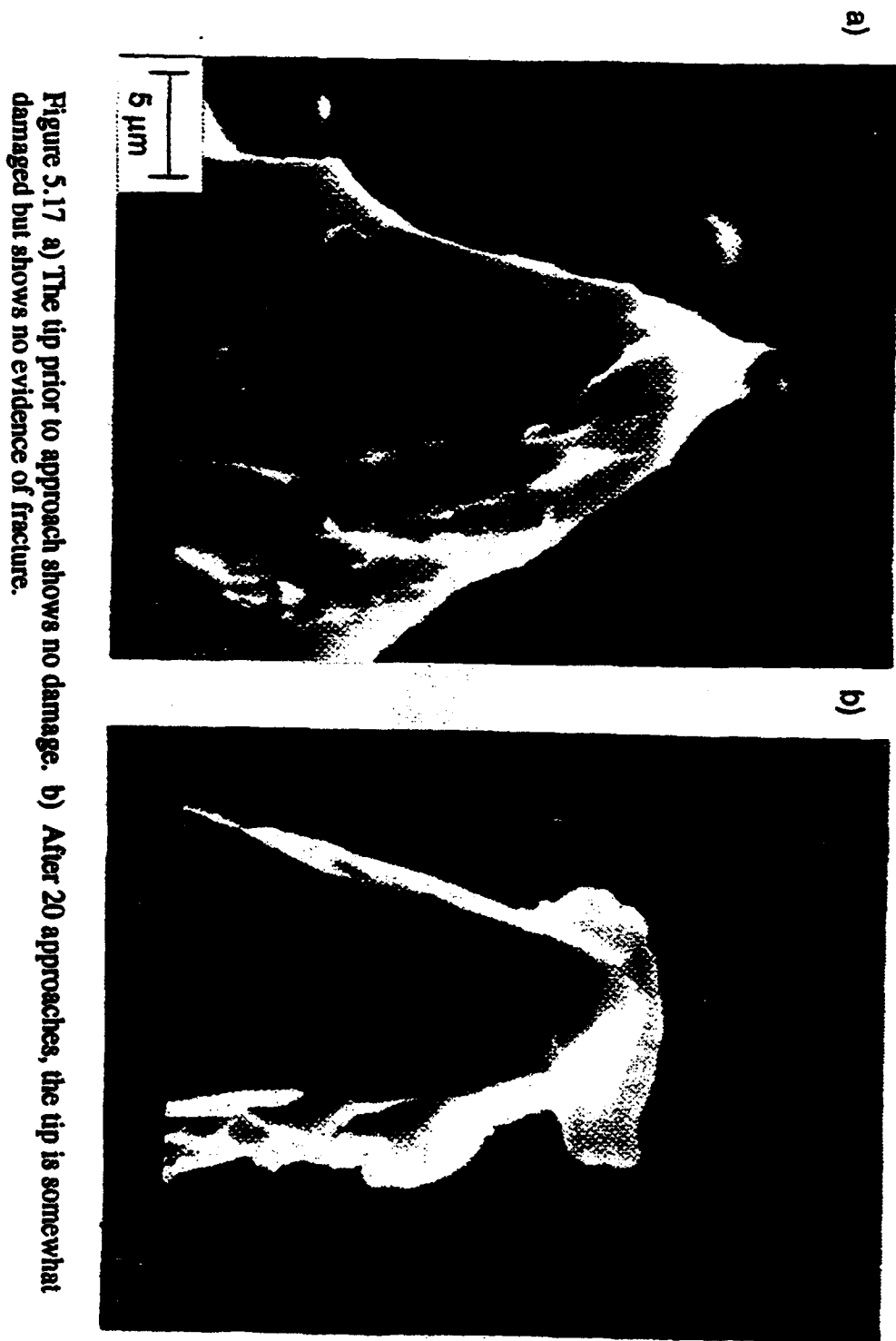
Figure 5.17 a) The tip prior to approach shows no damage. b) After 20 approaches, the tip is somewhat damaged but shows no evidence of fracture.

References

1) K. Takata, T. Hasegawa, S. Hosaka, S. Hosoki, and T. Kumoda, Appl. Phys. Lett. **55**, 1718 (1989).

2) W. P. Mason and R. F. Wick, J. Acoust. Soc. Am., **23**, 209 (1951).

3) K. F. Graff, *Elastic Wave Motion in Solids* (Dover, New York, 1975).

4) L. E. Kinsler, A. R. Frey, A. B. Coppens, and J. V. Sanders, *Fundamentals of Acoustics Third Edition* (Wiley, New York, NY, 1982).

5) G. S. Kino, Acoustic Waves: Devices, Imaging, and Analog Signal Processing (Prentice-Hall, Englewood Cliffs, NJ, 1987).

6) B. A. Auld, *Acoustic Waves and Fields in Solids*, Vol. 1 (Wiley, New York, NY, 1973).

7) J.N. Israelachvili, *Intermolecular and Surface Forces* (Academic Press, Orlando, FL, 1985).

8) Y. Martin, C. C. Williams, and H. K. Wickramasinghe, J. Appl. Phys. **61**, 4723 (1987).

9) B. L. Heffner, G. S. Kino and B. T. Khuri-Yakub, Appl. Phys. Lett. **47** (1), 17 (1985).

10) L. D. Landau and E. M. Lifshitz, *Theory of Elasticity* (Addison-Wesley, Reading, MA, 1959).

11) K. E. Peterson, Proc. IEEE **70**, 420 (1982).

12) G. Simmons and H. Wang, *Single Crystal Elastic Constants and Calculated Aggregate Properties: A Handbook* (M.I.T. Press, Cambridge, MA, 1971).

13) G. Binnig, H. Rohrer, C. Gerber and E. Weibel, Phys. Rev. Lett. **50**, 120 (1983).

14) A. L. Weisenhorn, P. K. Hansma, T. R. Albrecht, and C. F. Quate, Appl. Phys. Lett. **54**, 2651 (1989).

Chapter 6: Transmission Mode NSAM Imaging

6.1 Two-Dimensional Transmission Mode Imaging

The NSAM described in this work can be operated in transmission mode in which acoustic waves are coupled from the tip into the sample. An image is formed by scanning the tip over the sample in a raster fashion while a feedback circuit is used to maintain the transmitted signal constant. This chapter describes briefly the experimental procedure of transmission mode imaging and presents several images.

6.2 Experimental Procedure

Before transmission mode imaging can be performed the transducers are first characterized in the frequency domain. Both the tip and the sample transducers are then tuned so that they have an insertion loss minimum at approximately the same frequency. The acoustic path length of the tip and sample substrate is determined after tuning. Path length is determined by connecting the transducers to an rf source and monitoring the time it takes an acoustic pulse to travel to the front surface of the substrate and echo back to the transducer. Typically, the tip substrate is a 1 mm (100) thick silicon wafer. Since the acoustic velocity in silicon is approximately 8400 m/s [1], the pulse takes 115 ns to travel through the tip substrate. The time of flight in the sample is a similar value so the transmitted acoustic signal in most cases can be expected to arrive approximately 200 to 250 ns after the application of the rf pulse to the transducer.

123

During transmission mode imaging, high speed FET switches are used as time gates so that only signals arriving in a 50 ns window centered around the expected arrival time are detected and all other signals are ignored. Stray rf signals reflecting from different parts of the substrate and from mismatched terminations can often appear at unexpected points in the time domain and can be confused for the true transmitted acoustic signal. Predetermining the actual acoustic path length prevents such misidentifications.

Once the expected acoustic delay is known, the tip is aligned directly over the receiving transducer. The alignment is done by approaching the tip to the sample using the mechanical screws to lower the tip to within approximately 25 μm of the sample. Using a hypodermic needle, deionized (DI) water is injected into the gap to allow direct acoustic transmission from the tip transducer to the sample transducer. Due to the sizes of the transducers and the possibility of multiple acoustic echos, some acoustic signal can almost always be detected even if the transducers are poorly aligned. When DI water is present in the gap, flat regions of the silicon wafer surrounding the tip conduct most of the acoustic power. Therefore, the acoustic signal intensity is very sensitive to the relative tilt of the sample with respect to the tip since the acoustic plane waves can experience phase-cancellation if the wafer substrates are not parallel. Tilt is not a significant concern when doing the actual transmission mode imaging however since the acoustic waves are introduced to the sample at a very small spot and they propagate spherically into the sample independent of the exact angle of the tip relative to the sample.

To perform the fine alignment, the x and y positions of the microscope head are adjusted, using the translation stage on the microscope head, until the signal is maximized. The precision of the translation stage is approximately 25 μm. Due to multiple lobes in the intensity field of the transducers, multiple peaks typically appear, making it difficult to

decide which peak represents the central lobe. In general, the central lobe can be identified because it arrives earliest in time after the application of the rf pulse and its intensity drops off most quickly with changes in lateral position. The time domain signal of two well-aligned transducers coupled through DI water is shown in Figure 6.1.

Figure 6.1 This oscilloscope photo shows the feed-through rf pulse (left) and the acoustically coupled pulse (right). The feed-through rf signal is coupled from the rf source to the rf detector through the air and therefore arrives almost instantaneously. The acoustically coupled pulse arrives after a delay time determined by the path length and the acoustic velocity in water. The horizontal axis is 50 ns/division.

When the alignment is properly completed, the DI water is blown out of the gap with a filtered air gun and the sample is allowed to dry for a few minutes before proceeding with the experiment.

6.3   Transmission Imaging

Imaging in the transmission mode is accomplished in a manner similar to the constant current mode for STM or constant force mode for AFM. The tip is scanned over the sample while a feedback circuit controls the z piezo of the scanner tube constantly adjusting the spacing between the tip and the sample to keep the transmitted signal constant. The image of the surface is created by recording the output of the feedback circuit for each x and y position. Figure 6.2 shows a SEM image of a 6.5 micron period grating fabricated by plasma etching trenches into a silicon wafer.
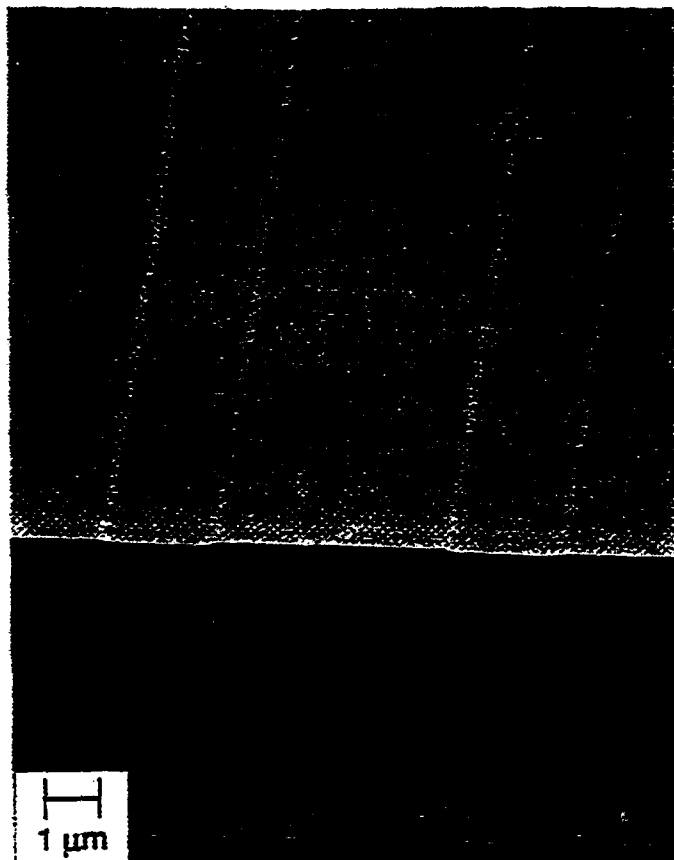

Figure 6.2 This SEM photo shows a 6.5 micron period silicon grating with step height of 940 Å.

126

Figure 6.3 A close-up SEM photo of grating profile shows that the depth of the trenches is about 940 Å. The grating edges are not sharp.

The depth of the trenches as measured from the SEM in figure 6.3 is 940 Å.

135 MHz Acoustic Image
960 A step height
Constant height mode

1 μm
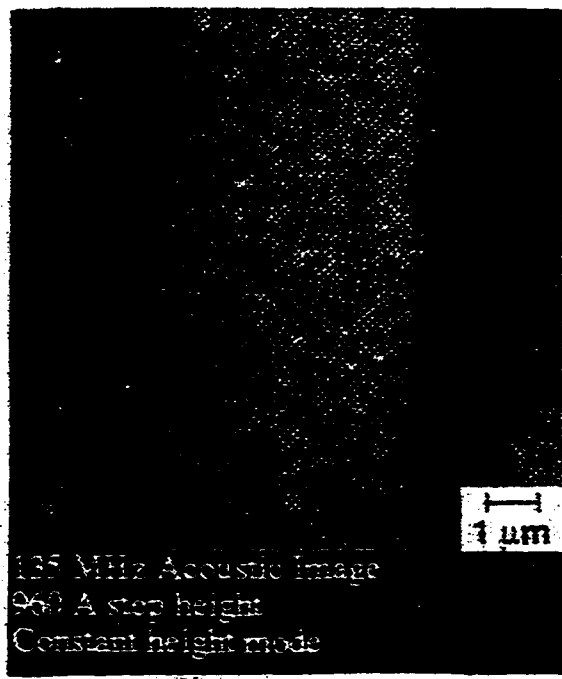
Figure 6.4 This transmission NSAM image of the 6.5 micron period silicon grating was taken using a tetrahedral tip and an acoustic frequency of 135 MHz. A hybrid NSAM assembly was used to take this image.

The NSAM image of the same grating is shown in figure 6.4. The depth of the trenches as measured from the NSAM images is 960 Å. It took approximately 3 minutes to scan this 512 x 512 pixel image.

128
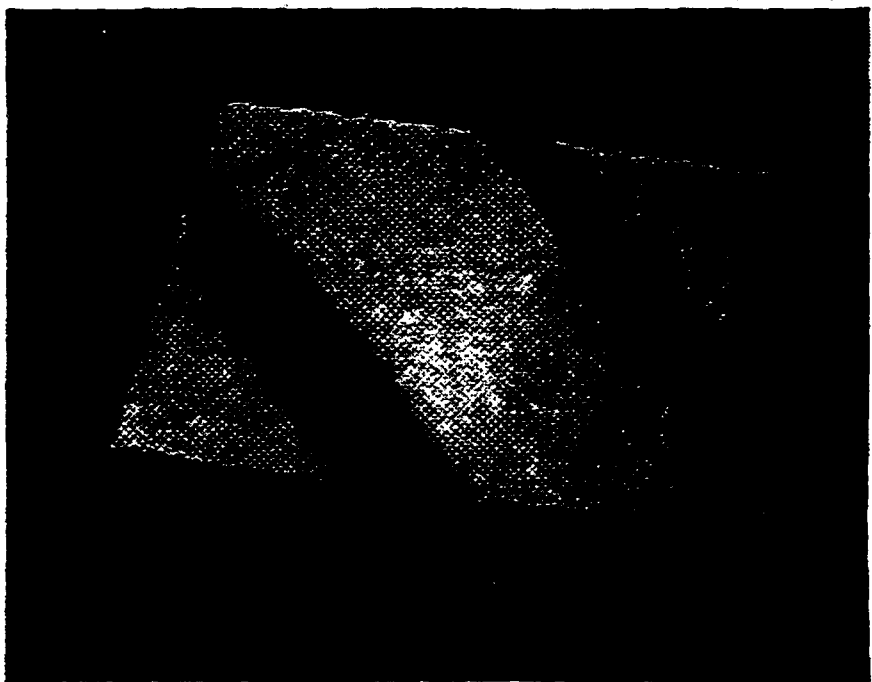
Figure 6.5 The scan direction was rotated to yield this 3-dimensional
transmission NSAM image of a 6.5 μm period silicon grating with 940 Å
step height. The image was taken using a tetrahedral tip and an acoustic
frequency of 135 MHz.

The scan angle was rotated to produce the three-dimensionally rendered image of
the same grating shown in Figure 6.5 These images were taken using 135 MHz acoustic

129

waves in the constant height mode. A tetrahedral tip with anodically bonded transducer
was used to obtain this image.

25 μm

Figure 6.6 During imaging, the transmitted acoustic signal became unstable
and the image quality was permanently degraded. Upon inspection in the
SEM, the tip was found to be fractured apparently along crystallographic
planes.

During imaging the feedback loop momentarily became unstable and the resolution
degraded significantly. Inspection of the tip in a SEM revealed that the tip had probably
come into hard contact with the sample resulting in the fracturing of the tip (Figure 6.6).
On several occasions, the fracturing of the tetrahedral tips seemingly along crystallographic
planes was observed.

130

The 6.5 micron grating was also imaged using a conical tip with an integrated transducer fabricated on the same silicon substrate. For the image shown in figure 6.7 the acoustic frequency was 815 MHz. The signal-to-noise ratio of this image is noticeably higher than that for the images taken at 135 MHz.

The SEM cross-section of the grating shown in Figure 6.3 shows that the transition width from 10 to 90% height is 1250 Å. The 10 to 90 % transition in the NSAM image is 1300 Å as shown in Figure 6.8.
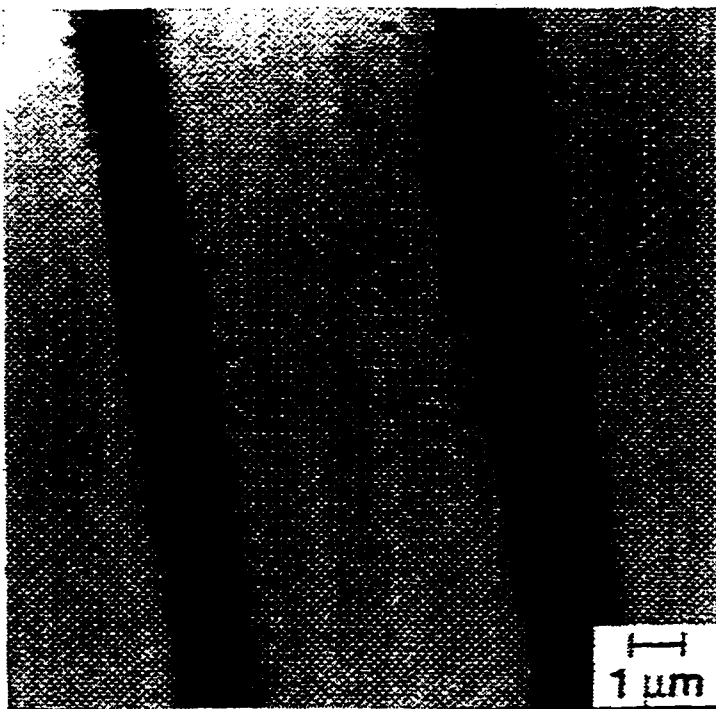
Figure 6.7 A conical tip integrally fabricated with a 200 μm transducer was used to obtain this image of the 6.5 μm silicon grating. The acoustic frequency was 815 MHz.

The 6.5 micron grating was also imaged using a conical tip with an integrated transducer fabricated on the same silicon substrate. For the image shown in figure 6.7 the

acoustic frequency was 815 MHz. The signal-to-noise ratio of this image is noticeably higher than that for the images taken at 135 MHz.

The SEM cross-section of the grating shown in Figure 6.3 shows that the transition width from 10 to 90% height is 1250 Å. The 10 to 90 % transition in the NSAM image is 1300 Å as shown in Figure 6.8.
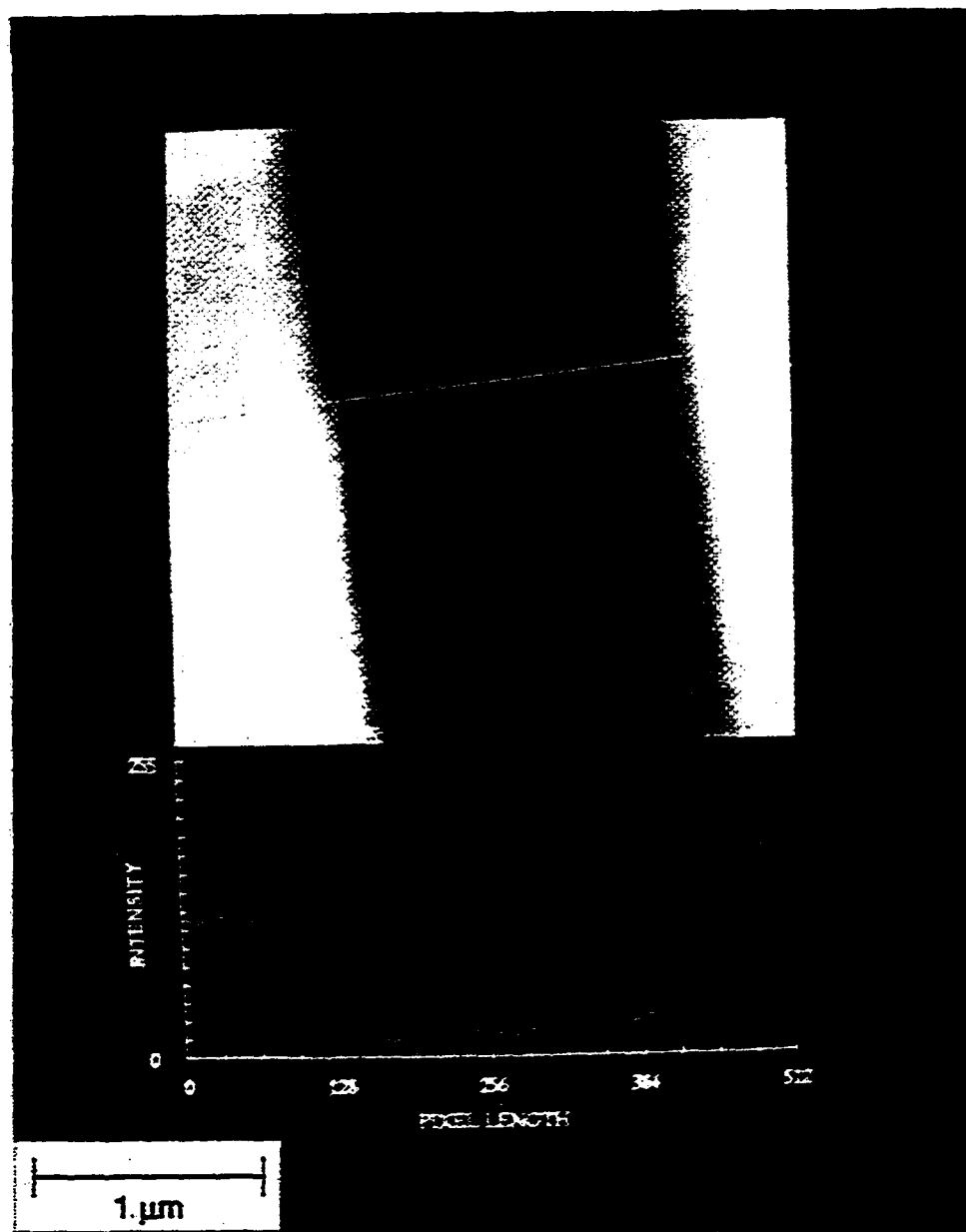
Figure 6.8 An NSAM image of a reduced scan area is used to obtain a 1-dimensional trace. The 10 to 90 % transition of the step is measured from the trace to be 1300 Å whereas the grating transition as measured from the SEM profile in Figure 6.3 was 1250 Å.

133

References

1)   A. R. Selfridge, IEEE Trans. on Son. and Ultrason. **SU-32**, 381 (1985).

Chapter 7: Electrostrictive Mode Near-Field Acoustic Operation and Imaging

7.1   Electrostrictive Mode

In previous chapters the transmission mode operation of NSAM has been discussed. While transmission mode NSAM imaging provides good lateral resolution and can be used to image insulators as well as conductors, this mode of operation has several experimental disadvantages.

The foremost disadvantage of the transmission mode is that it necessarily utilizes two transducers, one on the tip substrate and the other on the sample. The need for a transducer on the sample means that any potential sample must first have an ultrasonic transducer fabricated on its back side. This requirement limits the range of samples that can be examined in the NSAM. A second consequence of using two transducers is that alignment of the tip with respect to the sample is important. Even if both transducers are working properly and are tuned to the same frequency, any misalignment results in attenuation of the transmitted acoustic signal.

Another possible disadvantage of transmission mode imaging is that the tip may be in contact with the sample during operation in this mode. While Takata has suggested the operation of the NSAM in a non-contacting transmission mode using van der Waals attractive forces to couple acoustic power from tip to sample [1], such a technique has yet

to be demonstrated. Contact imaging is common in the field of AFM but even there, a growing number of researchers are moving toward non-contact mode imaging to avoid problems associated with friction and sample damage [2].

Electrostrictive imaging mode is a non-contact mode of operation that utilizes electric fields between the tip a sample to generate acoustic waves [3]. An rf electric field applied between the tip and the sample exerts time-varying attractive forces between tip and sample. These attractive forces generate acoustic waves which propagate up the tip where they are detected by the tip transducer (Figure 7.1). Only one transducer is necessary in electrostrictive mode operation, hence the problem of aligning transducers is eliminated.
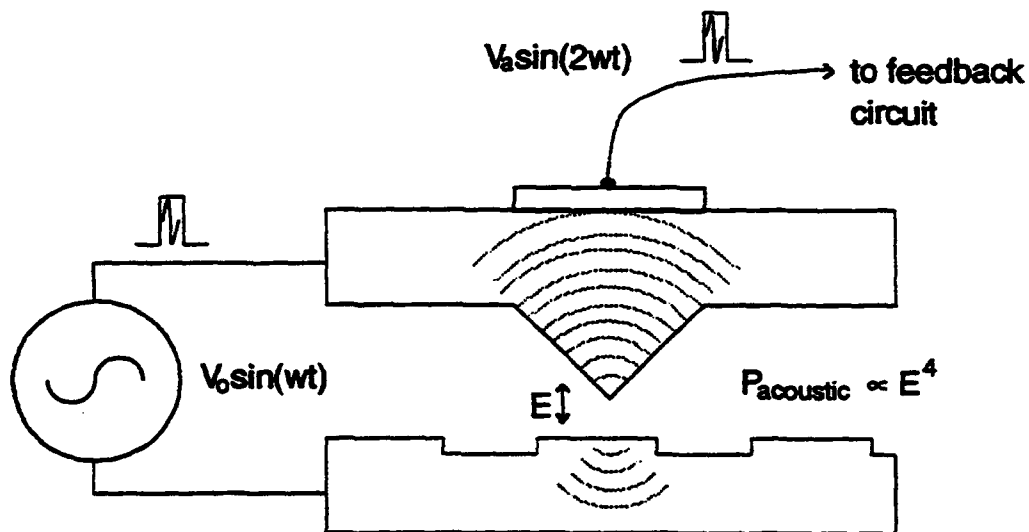

Figure 7.1 Applying an rf electric field between a conductive tip and sample electrostrictively generates acoustic waves which can then be detected by the tip transducer.

The electrostrictive mode is not without its own disadvantages. First, since the electrostrictive mode is non-contacting, the resolution may be lower than in the transmission mode because the spacing between the tip and sample is increased. Secondly, since the electrostrictive mode relies on electric fields, the sample and tip must be somewhat conductive to localize the electric field.

The following sections describe our first attempts at electrostrictive mode imaging. A simple model for acoustic generation will be presented and some tip damage mechanisms will be discussed.

7.2 Electrostrictive Generation of Acoustic Waves

If a tip and sample are conductive, acoustic waves can be generated by applying a time-varying electric field between the tip and sample acting as counter electrodes. The presence of the electric field creates an attractive force between the tip and the sample that is identical to the force which exist between plates of a parallel plate capacitor. The acoustic power that is generated from a given electric field strength is found by expressing the acoustic power as a function of force and force as a function of the electric field.

If the medium is assumed to be lossless, the acoustic power generated by a given force can be calculated from the equation

$$\frac{P_{ac}}{A} = V_a \, T \, S$$

(7.1)

where P_{ac} is the acoustic power, A is the area of each capacitor plate, V_a is the acoustic velocity, T is stress and S is strain. In order to express the acoustic power as a function of

137

force, the two following relations are necessary [4]. The first is simply Hooke's Law relating strain to stress by an elastic constant, c.

$$S = \frac{T}{c}$$

(7.2)

The second necessary relation is the expression of the acoustic velocity in terms of the elastic constant and the density, ρ_0. This relation results directly from the solution to the wave equation for acoustic waves.

$$V_a = \left(\frac{c}{\rho_0}\right)^{1/2}$$

(7.3)

Using equations 7.1, 7.2 and 7.3, the acoustic power can be written as a function of force on the plates of a capacitor. The force on the plates of a parallel capacitor can be expressed as

$$F = -\frac{q^2}{2\varepsilon A}$$

(7.4)

where F is the force on the capacitor plates, q is the charge on either plate and ε is the dielectric constant of the material in the gap. In the case of a parallel plate capacitor the capacitance, C, can be written as $C = q/V$ and $C = \varepsilon A/d$, where d is the distance between the plates. Thus, equation 7.4 can be rewritten as

$$F = -\frac{1}{2}\varepsilon A E^2$$

(7.5)

where E is the electric field between the electrodes.

Finally, the relation between the acoustic power and the electric field can be expressed by substituting equations 7.2, 7.3 and 7.5 into equation 7.1 to yield

138

$$P_{ac} = \left(\frac{1}{V_a \rho_0}\right) \frac{A \, \varepsilon^2 \, E^4}{4}$$

(7.6)

Equation 7.6 shows that the acoustic power increases with area, as expected, and is proportional to the fourth power of the electric field. Since the electric field goes as d^{-1} for a fixed voltage, this equation indicates that the acoustic power falls off as the d^{-4}.

Although the d^{-4} dependence of the acoustic power on distance is not as strong as the exponential signal dependence obtained in STM and experimentally observed transmission mode NSAM, by comparison, van der Waals force, which is the measured quantity in attractive mode AFM, only decreases as d^{-2}.

An important consequence of the E^2 behavior of force is that frequency mixing can occur through this non-linear interaction. For example, a time varying electric field, $E = E_0 \sin(\omega t)$, applied to the electrodes produces a force

$$F = \frac{1}{4} \varepsilon \, A \, E_0^2 [1 - \sin(2\omega t - \varphi)]$$

(7.7)

where φ equals $-\pi/2$. Since the force generated by the electric field goes as E^2, the total force consists of a sum and difference term. The sum term yields a signal at frequency 2ω while the difference term produces a DC component.

The mixing effect of the electric force interaction can be beneficial in several respects. Since an input electric field signal at frequency ω produces an acoustic signal at 2ω, the detection electronics can provide a better signal-to-noise ratio by filtering out the unwanted rf feed-through signal at ω. Knowing the acoustic signal's expected frequency and acoustic time delay allows proper identification of the received signal from among other sources of stray rf noise.

Other researchers are investigating the use of this mixing effect with the AFM to sample high frequency signals. If a sample has a high frequency signal, ω_1, on board this signal can be detected electrically by applying a second rf field, ω_2, between the tip and sample and sweeping the frequency of the applied field. The applied field and the sample's rf signal mix and electrostrictively generate acoustic waves at $\omega_1-\omega_2$ and $\omega_1+\omega_2$. A peak response will be detected by the acoustic transducer when ($\omega_1-\omega_2$) or ($\omega_1+\omega_2$) equals the tip transducer's operating frequency [5, 6].

7.3 Acoustic Power Versus Distance

There has been some conjecture that electrostrictive forces do not decay with distance rapidly enough to be useful as a feedback signal in near-field imaging [3]. While such claims certainly have much empirical support, without further investigation they are not completely justifiable since factors such as the signal-to-noise ratio and the sharpness of the tip also help determine whether or not a particular interaction mechanism is suitable for use in near-field microscopy.

To determine whether or not a particular interaction mechanism can be used to produce a feedback signal for near-field imaging we measured the signal vs. distance curve for the system. A description of the measurement procedure for the transmission mode signal versus distance curve was presented in Chapter 5. In a similar fashion the electrostrictively generated acoustic power as a function of distance is measured by approaching the tip to the sample until a signal is barely detectable. The curve is plotted by monitoring the acoustic power signal while the spacing between the tip and the sample is electronically modulated by extending and contracting the piezoelectric tube scanner.

A measured signal versus distance curve is shown in Figure 7.2 The rf excitation

frequency was 355 MHz and the acoustic signal was detected at 710 MHz. The input rf

power was 10 W. Similar to the transmission mode acoustic signal, the electrostrictively

generated acoustic signal also does not display a snap-in behavior. When the vertical axis

is corrected to be linear in power, the acoustic power can be replotted as in Figure 7.3.
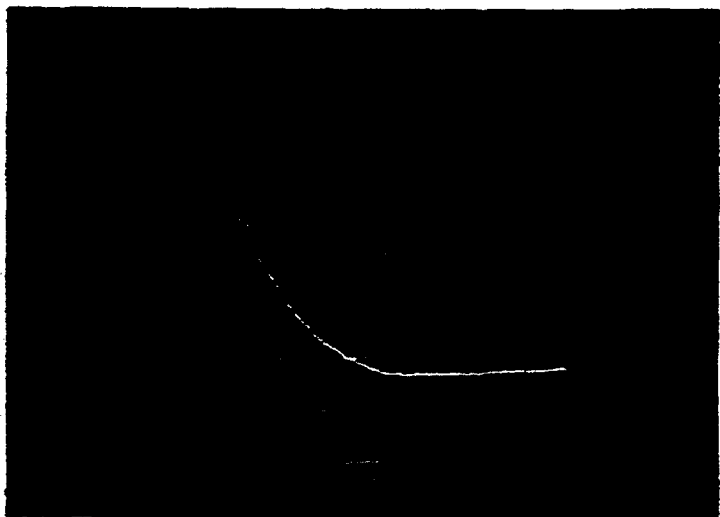

Figure 7.2 This oscilloscope photo displays the electrostrictively
generated acoustic signal power vs. distance between the tip and sample.
The horizontal axis is 1000 Å/division. The non-linear vertical axis
represents power from 0.03 to 6 nW as measured at the detection circuit
output.

It was seen in equation 7.6 that the acoustic power is expected to be proportional

to E^4. To confirm that this behavior occurs, the acoustic power is plotted as a function of

1/distance. 1/distance is chosen as the horizontal axis since the electric field is

proportional to 1/distance when the input rf voltage is held constant. Data points were

taken from Figure 7.2 and scatter plotted (Figure 7.4).
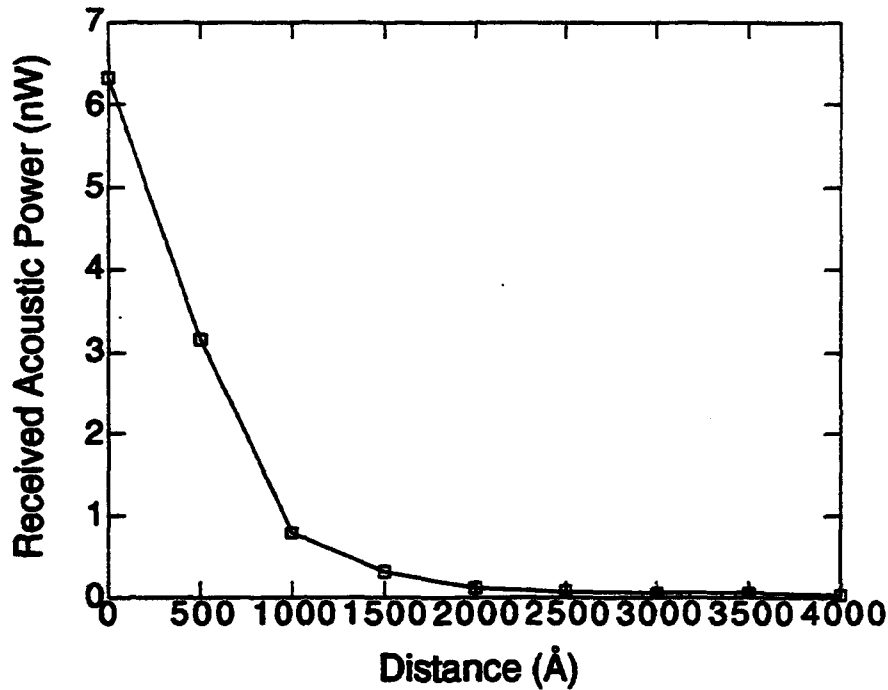
Figure 7.3 Data points are taken from the oscilloscope photo in Figure 7.2 and plotted against the vertical axis which is corrected to be linear in power. Electrostrictively generated acoustic signal power is plotted against increasing distance between the tip and sample.

The E^4 dependence for large distances supports the contention that the monitored signal is in fact the acoustic signal that is generated by the electrostrictive generation mechanism. At small spacings, where the data deviates from the expected E^4 dependence, some portions of the tip may actually be coming into contact with the sample or contamination layer thereby changing the effective impedance of the gap.

In addition, if the electrical contact is large enough to support significant current flow, local resistive heating may initiate thermoacoustic generation of acoustic waves. Resistive heating is proportional to the square of the voltage and therefore, any acoustic signal generated by this mechanism would also display exhibit frequency doubling.
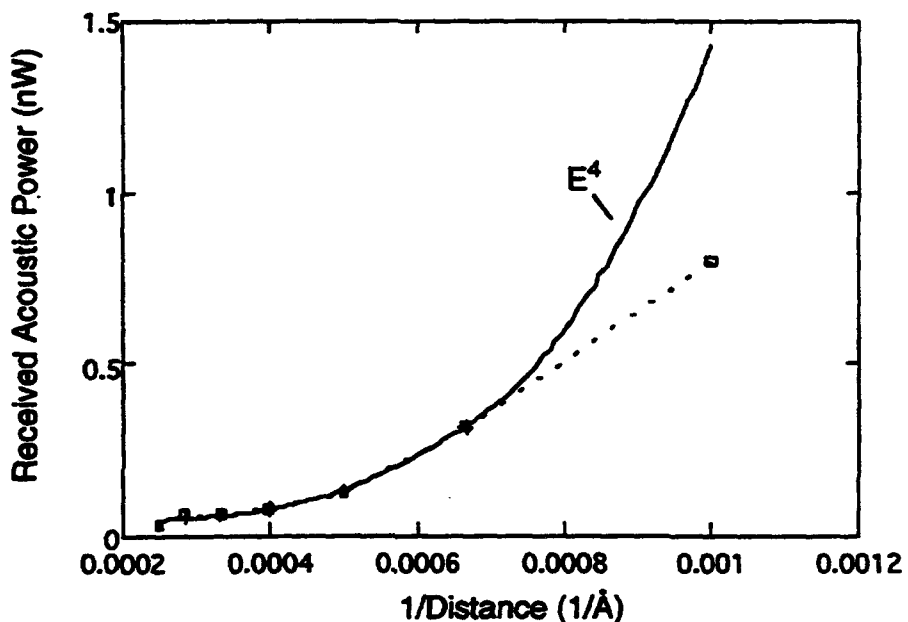

Figure 7.4 The relation of acoustic power to distance exhibits E^4 behavior at large spacings and is well fit by a curve, $Y = 0.042 + 1.4\,x^4$. The data is plotted as a dashed line and the fitting curve is shown as a solid line.

7.4 Relation of Acoustic Power to Force.

In addition to the advantages of single transducer operation and non-contact imaging, the electrostrictive mode of operation has one other clear advantage over the transmission mode imaging. In the electrostrictive case, the coupling mechanism between the sample and tip is relatively clear compared to the transmission mode case

where it is still uncertain as to which coupling mechanism dominates the interaction between the tip and sample.

In the electrostrictive case, the acoustic power generated by the electric field can be modeled and calculated knowing the magnitude of the applied rf electric field as shown in equation 7.5. The force for a given rf voltage, V, is

$$F = -\frac{\varepsilon A V^2}{2 d^2} \tag{7.8}$$

For 10 W input rf power the corresponding rms voltage is 22.2 V on 50 Ω coaxial lines. In the electrostrictive mode, the rf field is applied to the open circuit represented by the gap between the tip and sample so the actual voltage including reflection will be 44.4 V. The dielectric in the gap is assumed to be air or vacuum. The area is taken to be a flat circular area of 1000 Å radius. This is a reasonable assumption for the first order since the force is a weak function of distance and the entire cross-section of the 1000 Å tip radius is assumed to interact with the sample

When equation 7.8 is calculated it can be plotted against distance as is shown in Figure 7.5. In the electrostrictive case, the minimum detectable force is found to be on the order of 10^{-9} N. Electrostrictive imaging is typically conducted at a spacing of 1000 Å so the force associated with imaging is actually in the mid-10^{-8}'s.
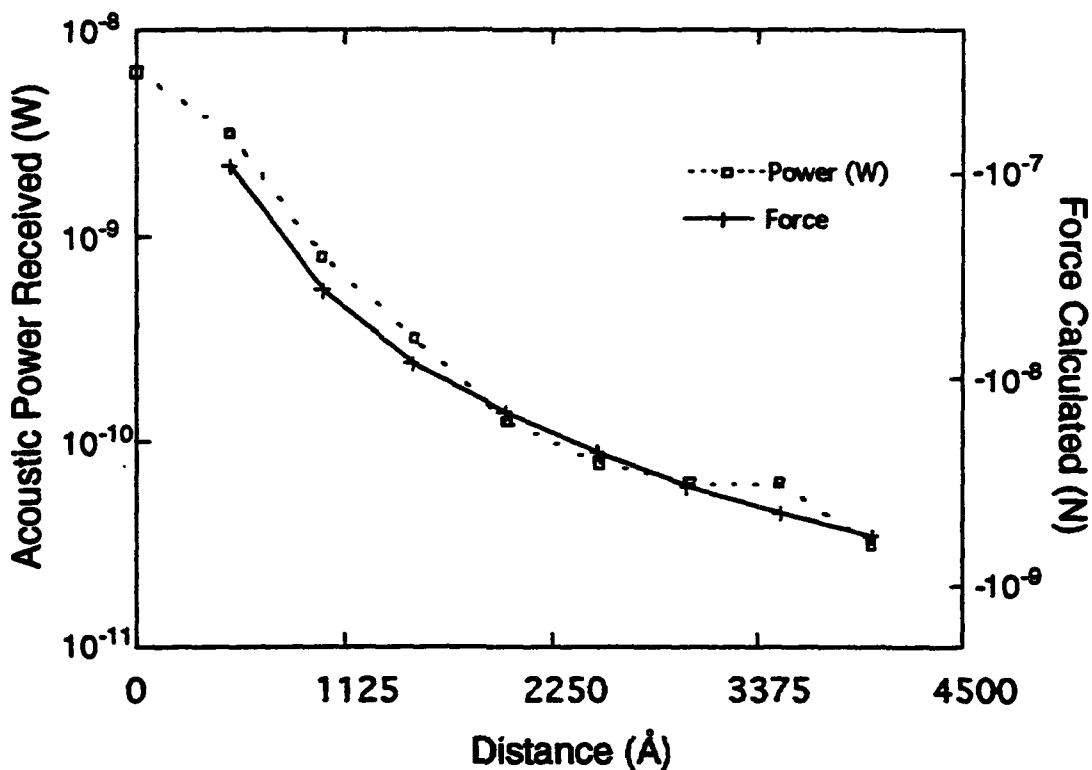
Figure 7.5 In the electrostrictive mode of operation, the force between the tip and the sample can be calculated from the acoustic power received. Typical force used during imaging is in the 10^{-8} N range.

The parallel plate capacitor model for calculating applied force during electrostrictive mode imaging is very crude. A more detailed model should include the actual capacitance between a plane and a sphere or a plane and a cone [7]. At a spacing of 1000 Å from a conductive plane, a 1000 Å radius sphere has a capacitance of 1.5 x $(4\pi\varepsilon r)$, where r is the radius of the sphere [8]. Calculated in this manner, with an applied voltage of 44.4 V, the force on the sphere is -10^{-6} N compared to -3×10^{-8} N calculated assuming the parallel plate model. One factor which would tend to reduce the calculated forces is the assumption for applied voltage. In the present model the voltage between

145

the tip and the sample is simply calculated from $V = (PR)^{-1/2}$ where P is 10 W and R is 50 Ω. In reality, parasitic capacitances between the line and ground may reduce the actual voltage which appears between the tip and sample. Even a small reduction in voltage could be significant since the force goes as the square of voltage.

Another simplifying assumption which could be enhanced is the assumption that the dielectric medium in the gap is air or vacuum. At large distances, it is a good assumption to let $\varepsilon = \varepsilon_0$ but as the gap becomes smaller, the capacitance is increasingly dominated by the dielectric coefficient of the 10 to 100 Å thick contamination layer which is assumed to have a dielectric coefficient similar to hydrocarbons. The capacitance and force increase linearly with increasing ε and therefore the force is expected to rise faster than d^{-2}, predicted by the air dielectric assumption, as the spacing decreases below 1000 Å.

Due to these and other factors which are at present unknown, the model presented above can only be useful in giving a heuristic sense of the force behavior in the electrostrictive mode. More rigorous analysis may be possible when an NSAM is demonstrated in vacuum where contamination layers are eliminated.

7.5   Electrostrictive Mode Imaging

In order to use the electrostrictive imaging mode a few simple modifications must be made to the NSAM. The most important modification is the introduction of a rf coaxial line very close to the tip and sample. The magnitude of the acoustic signal that can be generated relies directly on how efficiently the rf electric field can be introduced into the gap. The rf electric field must be brought as close to the gap as possible through a coaxial line terminating in the open circuit gap. A special fixture to hold the tip was

designed with one coaxial line to deliver the rf power to the gap and a second line to transmit the detected acoustic signal from the tip transducer to the detection electronics (Figure 7.6).
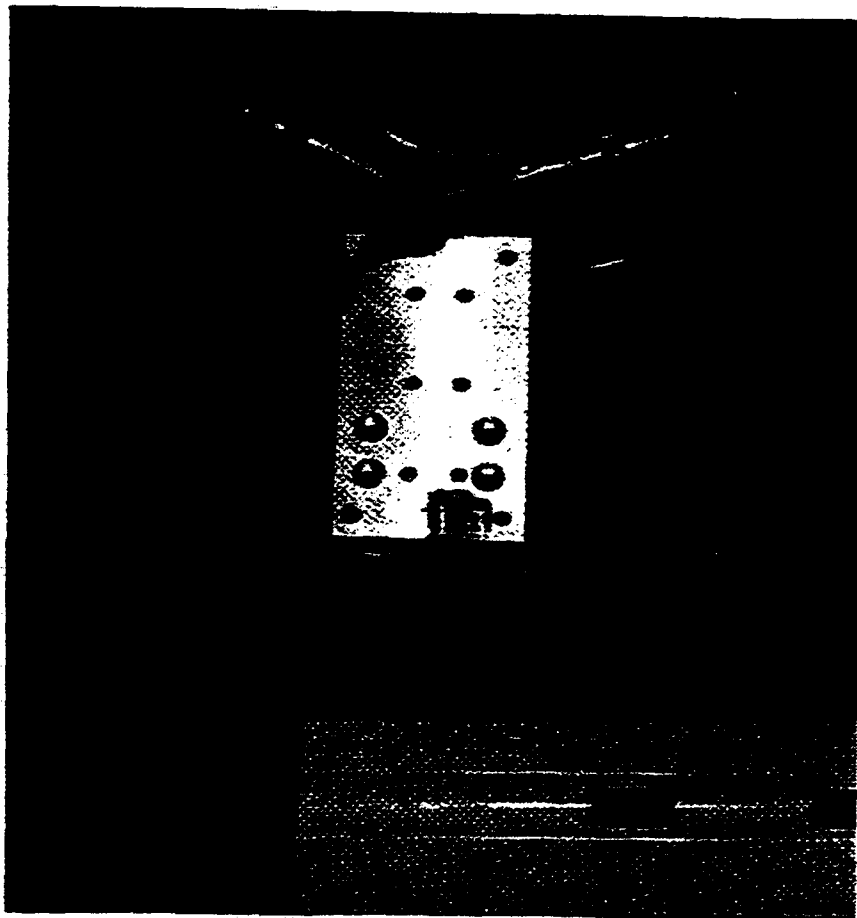

Figure 7.6 The tip holding fixture has one coaxial line to bring in the rf field to be applied to the gap and second coaxial line to receive the detected acoustic signal from the tip transducer.

The tip is mounted on the specialized tip holder and a gold wire is soldered between the tip and the center conductor of the rf delivery coaxial line. The tip is then

brought within a hundred microns of the sample using the positioning screws. A 1 mil gold wire is then attached from the sample to the outer conductor of the coaxial line so that the sample is effectively grounded. The length of each gold wire is made as short as possible and is typically 1 cm. Then, without the need for any alignment, the tip is lowered to its final position over the sample and the rf electric field is excited. The final approach is made electronically by extending the piezoelectric tube scanner while monitoring the acoustic signal.

When the tip is sufficiently close to the sample, an acoustic signal is detected. Since the electric force interaction is non-linear, an exciting electric field at frequency ω produces an acoustic signal at frequency 2ω. Filters are used to attenuate the feed-through signal at the fundamental frequency to improve the signal-to-noise ratio at 2ω. As in the transmission mode case, a time gate is placed on the received signal so that only the incoming signal which has undergone the expected delay associated with acoustic propagation in the tip is captured to create the image. The ability to identify the signal in frequency and time, allows higher confidence that the image is composed of the electrostrictively generated acoustic signal only.

The sample and tip must be conductive in order for the electrostrictive mode to function. The grating shown in Figure 7.7 consists of 4000 Å thick gold lines on an evaporated aluminum film on a silicon substrate. The lines are 2 μm wide and the grating period is 7.5 μm. The quality of the edges is low due to poor lift-off of the gold film during fabrication.
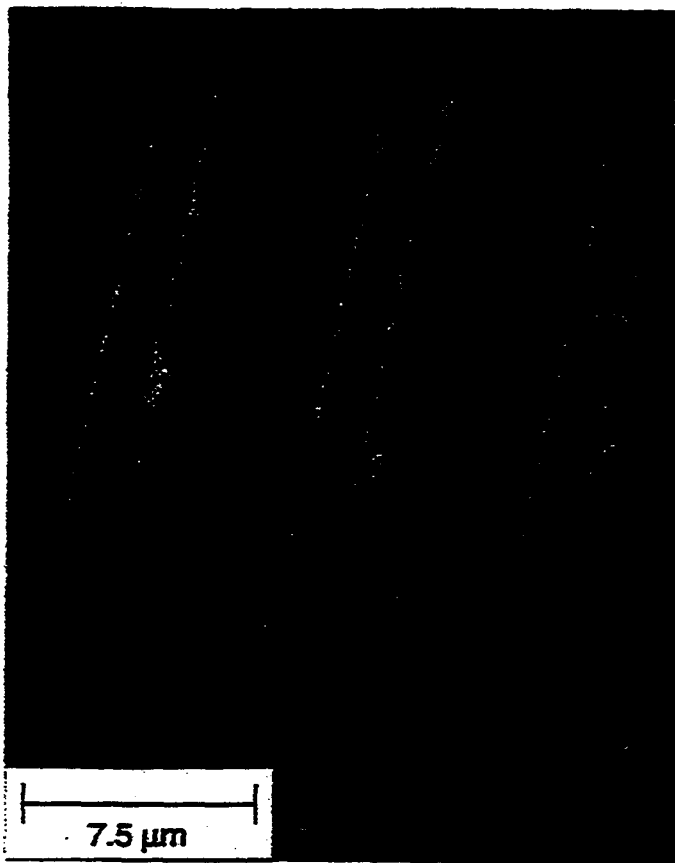
Figure 7.7 The gold grating consists of 4000 Å thick gold lines deposited on an aluminum covered silicon wafer. The period is 7.5 μm and the line widths is 2 μm.

The image of the sample taken in electrostrictive mode is shown in Figure 7.8. The apparent non-linearity in the grating period is due to the non-linearity of the large scale piezo scanner used. The bright object at the right is the smallest individual feature that was resolved and therefore the lateral resolution of the microscope in this instance is approximately 5 μm. The received acoustic power level during imaging was set at 0.5 nW which corresponds to a force of 50 nN. The spacing between the tip and the sample was approximately 1000 Å. The image took approximately 3 minutes to create.

149
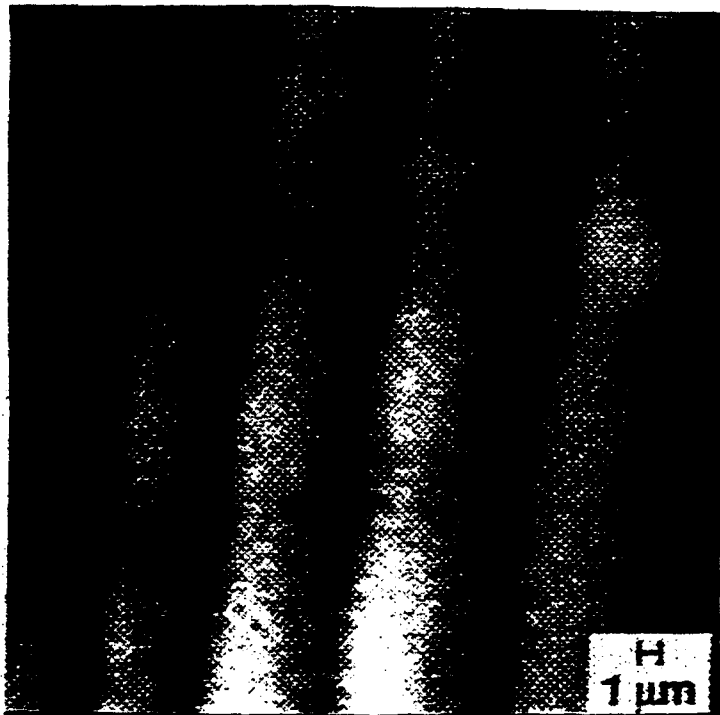
Figure 7.8 An electrostrictive mode image of 7.5 μm period gold grating. is shown here.

The thin gold lines which should be 2 μm appear much wider in the image. Several factors may be contributing to this effect. The first is simply the sharpness of the tip. Although most tips have approximately 500 to 1000 Å radius when they are fabricated, the presence of the metal coating or damage to the tip could cause the tip to be duller than expected.

More fundamental problems result from the fact that the equipotential lines over the sample surface may not be faithful to the surface topography at the height of the tip over the sample. For example, electric field lines are concentrated around sharp edges and points and therefore, such features should be accentuated in the images.

150

In Figure 7.8, the quality of the tip and not the electric field effects is probably responsible for the poor resolution. These are the first images obtained in electrostrictive mode, and therefore there is much room for improvement. An order of magnitude of improvement in the resolution should be attainable simply by improving the quality of the tips and optimizing the rf electronics for use in electrostrictive mode imaging.

7.6 Tips For Electrostrictive Imaging

In electrostrictive mode imaging, the tip and sample must be conductive in order to confine the electric field to the gap between the tip and the sample. The best way to make conductive microfabricated tips might be to heavily dope the surface of the silicon tip during fabrication. At the time the tips were fabricated for this generation of the NSAM, the need for conductive tips was not anticipated and therefore the silicon tips were fabricated using lightly doped silicon. In order for the tips to be useful in the electrostrictive mode, a way had to be found to make the tips conductive.

7.6.1 Damage to metallized tips

The easiest method for making the tips conductive without doping the silicon is to coat them with a metal. The metal coating must be thick enough to be conductive while not being so thick as to detract greatly from the sharpness of the tip. Gold was chosen as the metal for the coating since it is highly conductive and therefore can be used in thinner films while maintaining good conductivity. Figure 7.9 and 7.10 show the same tip before and after the deposition of 2000 Å of gold. The radius of curvature has increased from 300 Å before the gold coating to 1500 Å after the sputter deposition of gold.

151

Figure 7.9 A silicon tip with no metal layer has a radius of curvature of approximately 300 Å.

The tips coated with sputtered gold did produce some acoustic signals but their operation was very unstable. Often the image quality was quite poor from the start or degraded rapidly over a few minutes. Inspection of the tips after imaging revealed substantial damage to the gold film.
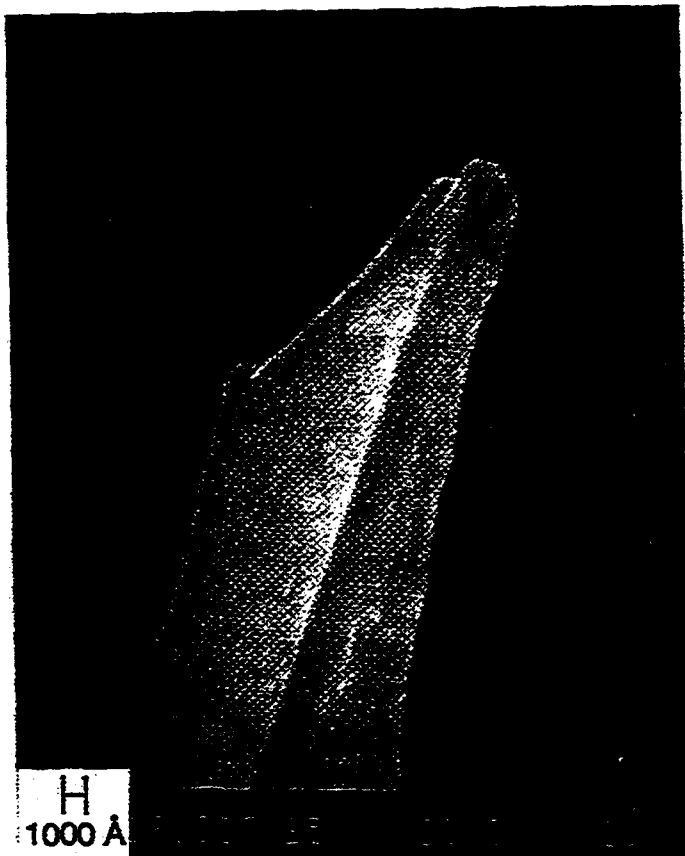
Figure 7.10 After the sputter deposition of 1500 Å of gold, the radius of curvature of the tip has increased from 300 Å to over 1500 Å.

The damage to the metal coating is most likely due to two mechanisms. The first mechanism is resistive heating upon contact with the sample. If the tip comes into contact with the sample a large current can flow and cause the gold layer to melt. If the contact is not sufficiently conductive to short out the field completely, the electric field can exert high forces on the molten metal. The tip in Figure 7.11 was being used to image a gold grating when the signal suddenly saturated. When the tip was examined in the SEM, a metal line from the sample was found fused to the tip after apparently having

153

been pulled off the surface. A closer inspection of the areas of damage reveals that the gold film was not simply rubbed off from contact but was in fact melted in the presence of a high field (Figure 7.12). When molten metal drops are extracted by high fields, very sharp cones can be left behind. This behavior suggests the possibility of fabricating sharp metal tips.
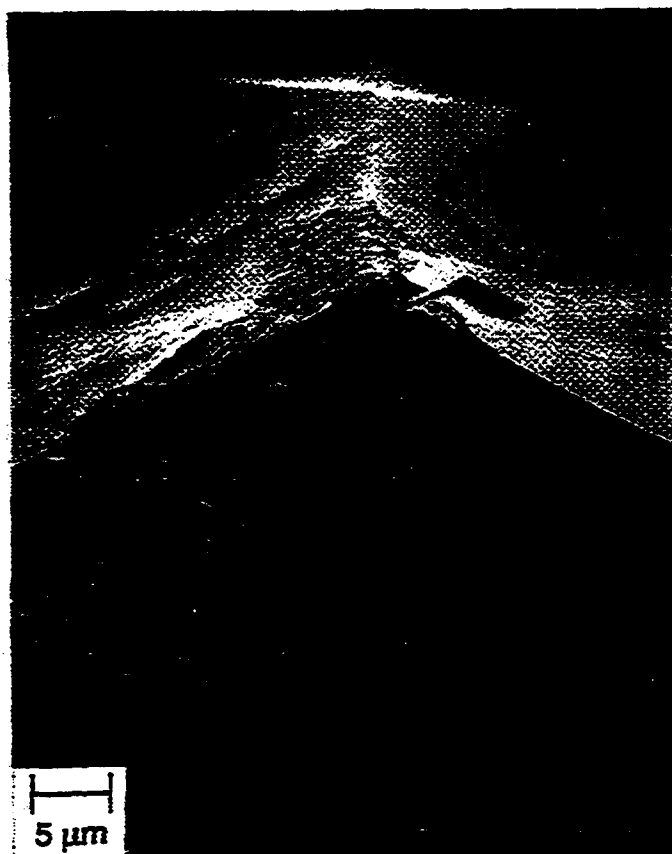

Figure 7.11 This tip was damaged by coming into contact with one of the metal lines of a grating.
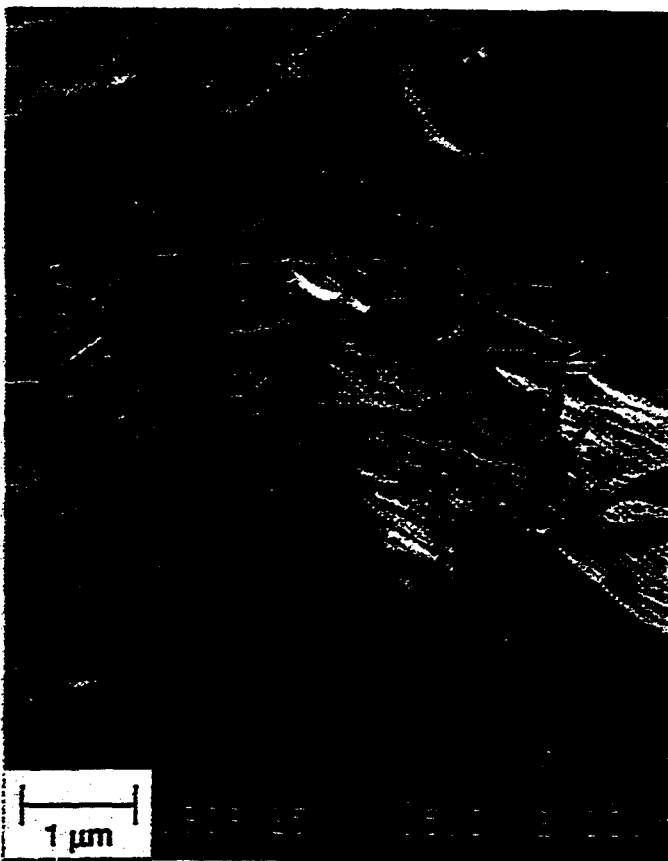
Figure 7.12 The damage to this tip was caused by the field emission of molten gold from the silicon tip.

In addition to melting of the gold film, a second damage mechanism is the loss of adhesion between the gold film and the tip. At the time of metal deposition, the tip's surface is covered by a layer of native oxide and a contamination layer due to exposure to atmosphere. The adhesion of gold to silicon dioxide is notoriously poor and the presence of the contamination layer compounds the problem. When a tip covered with gold is used in th electrostrictive mode the high electric fields in the gap between the tip and

155

sample can exert considerable forces on the gold film leading to the destruction of the film in some cases.
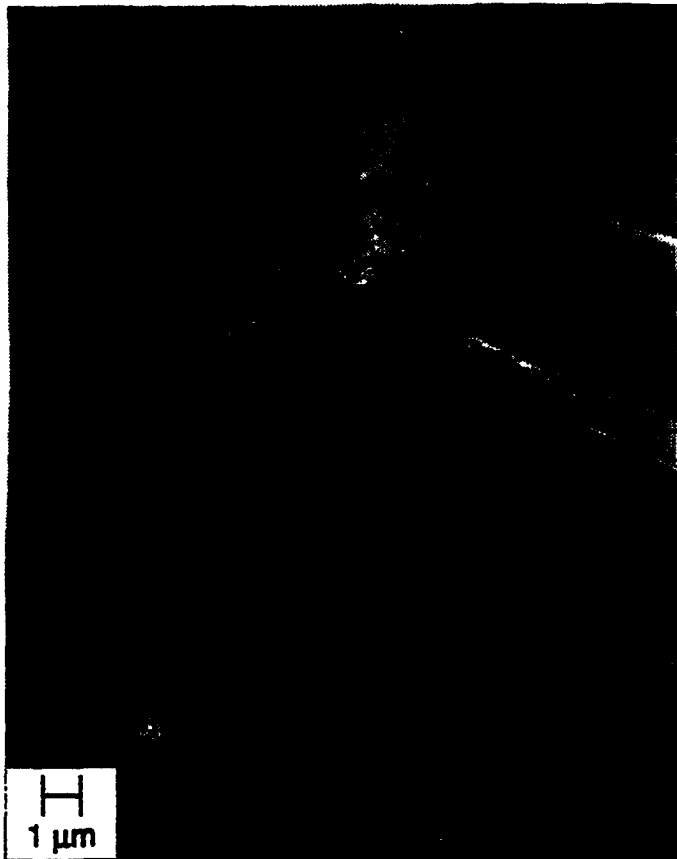
Figure 7.13 The gold layer of this tip is damaged over an area of approximately 10 μm while the silicon tip itself is only slightly damaged over a 2 μm region. Electrical factors caused the damage to the gold film while mechanical contact is probably responsible for the damage to the silicon.

One tip which was damaged in this manner is shown in Figure 7.13. This image shows the gold film damaged over a 10 μm region whereas the underlying silicon is only damaged over a 2 μm region. This photo indicates that at least in some cases the

instabilities in the electrostrictive signal are caused by failure of the metal coating and not mechanical damage to the silicon tip itself. In other words, the instabilities in the signal stem from electrical rather than mechanical factors.

The adhesion of the gold to the tip was improved by first sputter cleaning the tip for 20 seconds with argon at a power of 100 W on a 6" target. Then 20 to 40 Å of chrome are sputtered on the tips to act as an adhesion promoting layer. The tips are transferred through air to an evaporation chamber where they are coated with 2000 to 4000 Å of evaporated gold. Tips made using this process never exhibited an adhesion failure as shown in Figure 7.13.

7.6.2 Tip damage due to acoustics alone.

The damage to the tips discussed thus far has centered on the damage to the metal film caused by mechanical contact as well as effects due to the high electric fields present in the gap between the tip and sample. In addition to these effects, damage resulting simply from the motion of the tip induced by the presence of acoustic waves has also been observed. As described in Chapter 5, when the acoustic wave travels down the tip, the particle displacement within the tip is amplified toward the apex of the tip where the lateral dimension of the tip becomes comparable to half the acoustic wavelength. If the particle motion is sufficiently large, the adhesion of the metal film to the tip can be compromised. This form of acoustically induced damage to the tip can occur even when no electric field or sample is present.

To demonstrate the effect of acoustically induced tip damage, a tip was coated with sputtered chrome and evaporated gold as described previously (Figure 7.14 (a)). It is not entirely clear from the SEM photo that the metal film is continuous to the very apex

of the tip but this ambiguity is probably caused by poor contrast between silicon and gold in the SEM. This tip was acoustically excited for 1 second at 1 GHz with 1 W of rf power delivered to the transducer. During excitation, the tip was held in air with no sample present. There is no significant change to the appearance of the tip as a result of the acoustic excitation (Figure 7.14 (b)).

Figure 7.14 (c) shows the same tip after a 1 second excitation with 10 W of rf power. There is noticeable damage to the metal coating concentrated at locations with small radii of curvature. Since the amplification of particle motion is proportional to the reduction of cross-sectional area of tip, it is expected that asperities, edges and other sharp regions would experience the greatest degree of amplified particle motion.

To determine whether further damage would result with increased duration of the acoustic excitation, the tip was excited again for 10 minutes at 1 W. Figure 7.14 (d) shows that even after extended periods, the excitation at 1 W is insufficient to cause further tip damage. Extensive damage to the metal film does result however, if the tip is excited for 10 additional minutes at an rf power of 10 W (Figure 7.14 (e)). A close up view of the damage (Figure 7.15) clearly shows that the metal film is being torn off of the undamaged silicon tip.
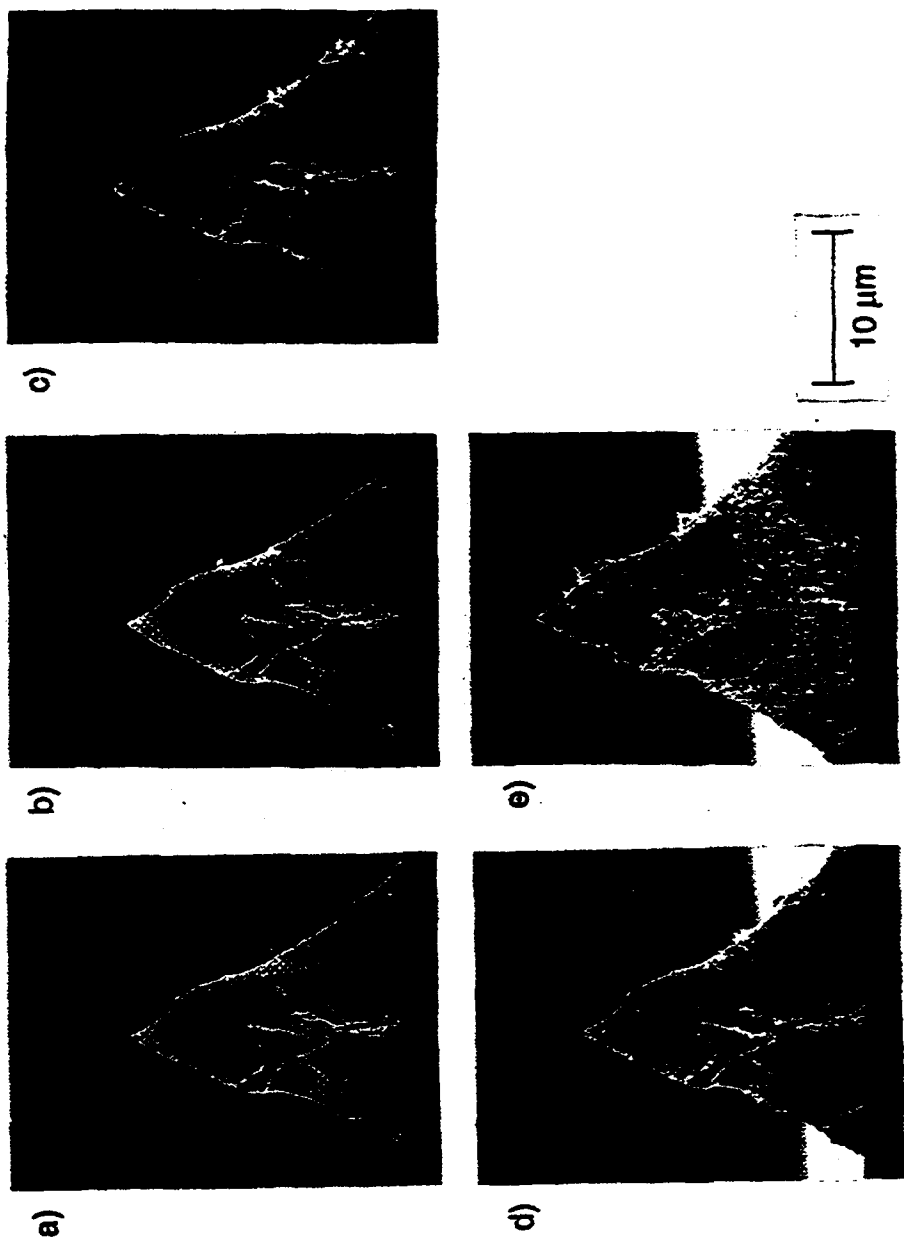
Figure 7.14 a) This tip was covered with 40 Å of sputtered chrome and 2000 Å of evaporated gold. b) After 1 second acoustic excitation with 1 W no significant damage is evident. c) After an additional second of acoustic excitation with 10 W the metal begins to fail in areas of high curvature. d) The same tip is excited again with 1 W for 10 minutes with no additional signs of damage. e) 10 minutes of acoustic excitation at 10 W causes extensive damage to the metal film.
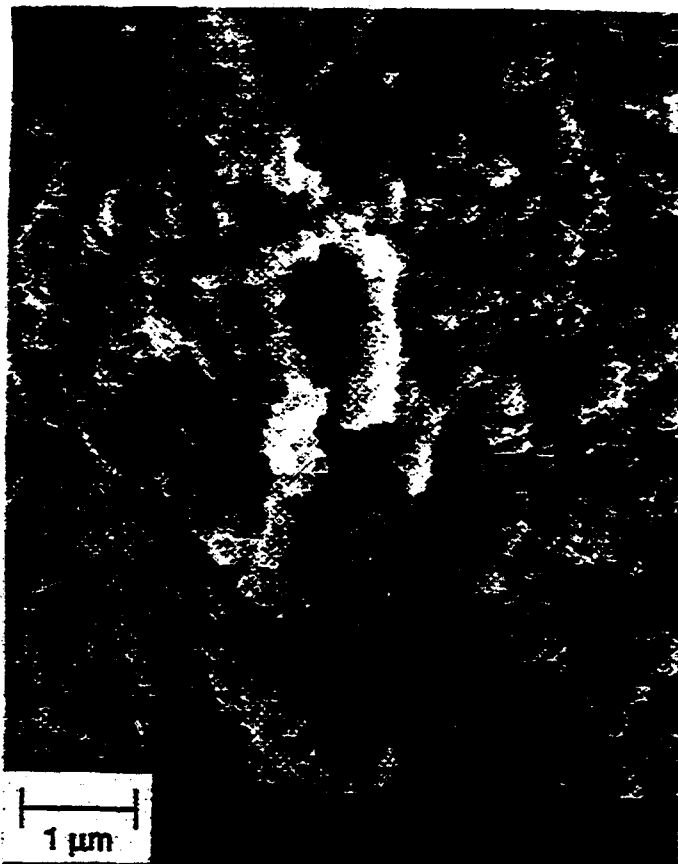
Figure 7.15 Closer inspection of the damaged metal film confirms that the metal layer is being broken up and adhesion to the substrate is compromised.

Figure 7.16 shows that the damage to the gold film is limited to the end of the tip. The fact that the damage is limited to the end of the tip is likely due to the fact that the particle motion is amplified near the apex of the tip by the Mason horn effect [9]. The amplification of particle motion in a sharply tapering tip is large enough to destroy the metal layer near the apex of the tip even though the loss in the majority of the tip, determined to be -42.5 dB (Chapter 5), indicates that it is a very poor wave guide. The

losses however, are small in the last segment of the tip comparable to an acoustic wavelength and therefore there is still significant particle motion amplification from that point to the tip's apex.
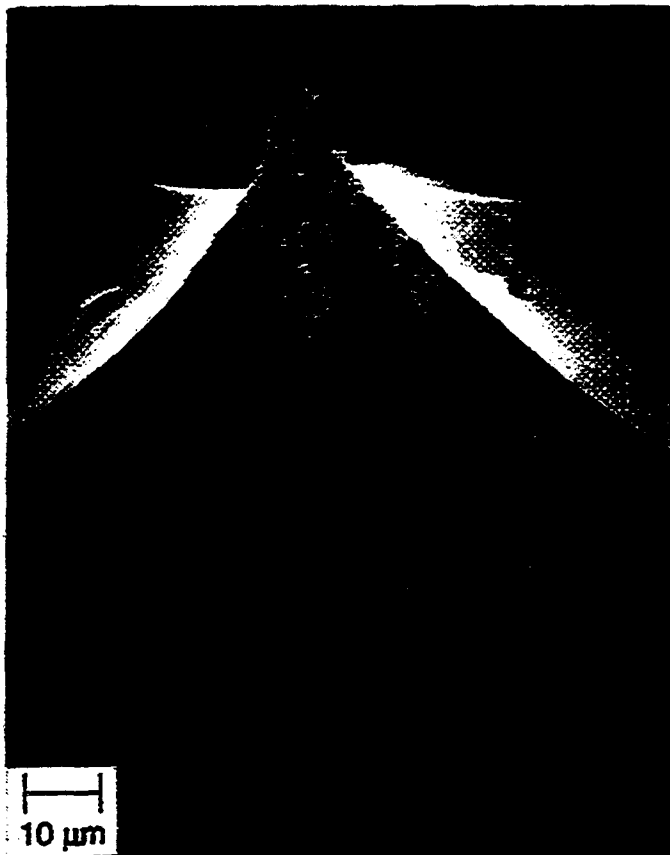

Figure 7.16 The damage to the metal film caused by acoustics alone is confined to the region of the tip roughly proportional to the acoustic wavelength.

161

7.7 Future directions for electrostrictive mode imaging

The electrostrictive mode of imaging may prove to be very fruitful. The resolution achieved to date is quite low but since it was the first attempt, an order of magnitude improvement is a reasonable goal.

Heavily doped silicon tips will decrease the instabilities currently associated with failure of the metal films. In addition, a great increase in resolution and reliability may be achievable if the NSAM with microfabricated probe is radically reconfigured to operate as a resonant mode instrument, similar to Güthner's microscope [10]. In the resonant mode, continuous wave operation may be possible and thereby lead to increased signal-to-noise ratios.

If the electrostrictive mode can be used reliably, it may become possible to detect high frequency signals on the sample by mixing a carrier rf signal with the signal carried on the sample. Other applications of the electrostrictive mode might include its use in the characterization of sample conductivity or thin film permittivity. The key to the success of any of these possibilities will be to improve the microscope's reliability through the introduction of new conductive tips and/or new detection techniques.

References

1) K. Takata, T. Hasegawa, S. Hosaka, S. Hosoki, and T. Kumoda, Appl. Phys. Lett. **55**, 1718 (1989).

2) Y. Martin, C. C. Williams, and H. K. Wickramasinghe, J. Appl. Phys. **61**, 4723 (1987).

3) K. Takata, T. Okawa, and M. Horiuchi, Jpn. J. Appl. Phys. **30**, 428 (1991).

4) G. S. Kino, Acoustic Waves: Devices, Imaging, and Analog Signal Processing (Prentice-Hall, Englewood Cliffs, NJ, 1987).

5) A. S. Hou, F. Ho, and D. M. Bloom, Electron. Lett. **28**, 2302 (1992).

6) G. E. Bridges and D. J. Thomson, Ultramicroscopy **42-44**, 321 (1992).

7) W. Denk and D. W. Pohl, Appl. Phy. Lett. **59**, 2171 (1991).

8) P. Lorrain and D. R. Corson, *Electromagnetic Fields and Waves* (Freeman, San Francisco, CA, 1970).

9) V. M. Ristic, *Principles of Acoustic Devices* (Wiley, New York, NY, 1983).

10) P. Güthner, U. Ch. Fischer and K. Dransfeld, Appl. Phys. B **48**, 89 (1989).